Radar Sub-surface Sensing for Mapping the Extent of Hydraulic Fractures and for Monitoring Lake Ice and Design of Some Novel Antennas

by

Jiangfeng Wu

A dissertation submitted in partial fulfillment
of the requirements for the degree of
Doctor of Philosophy
(Electrical Engineering)
in the University of Michigan
2016

Doctoral Committee:

Professor Kamal Sarabandi, Chair
Assistant Professor Brian R. Ellis
Associate Professor Anthony Grbic
Professor Leung Tsang

To God
To my parents Jun Mu and Fan Wu with love and gratitude.

ACKNOWLEDGEMENTS

First and foremost, I would like to thank and dedicate all my success to God.

This dissertation completed with invaluable help from my advisor, Prof. Kamal Sarabandi, whose help has been crucial to the successful completion of my doctoral degree. It is him who led me into research and also guided me through every step during my Ph.D. study. I couldn't have started my research life without him. I'm grateful for his advice and discussions. I am also deeply grateful to my other committee members, Prof. Anthony Grbic, Prof. Brian Ellis, Prof. Leung Tsang, who have also contributed insightful comments and valuable suggestions in my thesis to make it a more complete and better work. In addition to my committee members, I am extremely appreciative of Prof. Yogesh Gianchandani and Dr. Don Atwood for their input and constructive comments in my research projects.

I would like to thank the department of EECS for offering all those well-designed courses in a variety of areas. I thank Prof. Kamal Sarabandi, Prof. Anthony Grbic, Prof. Eric Michielssen, Prof. Mahta Moghaddam, Prof. Fawwaz Ulaby, Prof. Amir Mortazawi, Prof. Mona Jarrahi, Prof. Almantas Galvanauskas and Dr. Mortaza Nick, Dr. Seyit Ahmet Sis, Dr. Fikadu Dagefu, Dr. Mehrnoosh Vahidpoor, Dr. Hamid Nejatie for their tremendous works and enormous patience on teaching courses.

I am especially grateful to have Dr. Adib Nashashibi to help me solving many difficulties in laboratory works. I would like to thank Dr. Adel Elsherbini for tutoring me in the beginning of

my Ph.D. study. I'm also grateful to have many great colleagues in the Radiation Laboratory and EECS who have been working with me. For great friendship and enjoyable discussions, I thank Dr. Pierce Leland, Dr. Scott Green, Dr. Jungsuek Oh, Dr. Young Jun Song, Dr. Sangjo Choi, Dr. Meysam Moallem, Dr. Carl Pfeiffer, Dr. Hatim Bukhari, Dr. Liu Yang, Dr. Han Guo, Dr. Tian Wei, Dr. Yiting Zhang, Dr. Gurkan Gok, Dr. Amit Patel, Dr. Victor Lee, Dr. Scott Rudolph, Dr. Mohammad Imani, Dr. Onur Bakir, Dr. Abdulkadir Yucel, Dr. Lius Gomez, Dr. Mark Haynes, Dr. Jing Zhou, Dr. Jun Tang, Michael Benson, Armin Jam, Brian Tierney, Xiuzhang Cai, Jihun Choi, Amr Ibrahim, Mani Kashanianfard, Nikoloas Chiotellis, Lai Wei, Amanda Couch, Jason Heebl, Adam Weiss, Xiaoyu Wang, Seungku Lee, Seyed Mohammad Amjadi, Behzad Yektakhah, Milad Zolfaghar, Noyan Akbar, Peng Tian, Ning Wang, Guanbo Chen, David Chen, Shang Hua Yang, Morteza Sheikhofla, Tianlin Wang, Huanting Huang, Shurun Tan, Tai Qiao, …

I am grateful to my friends in Ann Arbor for their support during my Ph.D. studies. Without their companionship, I would not have such a memorable life in Ann Arbor. We celebrated weekends and holidays, traveled together, and encouraged one another to get through graduate school. Playing badminton with friends in UM Badminton Club and Ann Arbor Badminton Club is one of best stress-releasing activities I have enjoyed in the past five years. I am especially thankful to the friends coming with me to those "dangerous" sports, such as rock climbing and skiing. In addition, I would like to thank Pastor Weizhong Chang and my friends at Olive Tree Campus Church for sharing their stories and introducing God to me.

Finally, my greatest gratitude goes to my parents, grandparents and cousins. They always encourage me to follow my dreams and support me to pursue my dreams the best they can. I

would also like to thank my girlfriend Claire Zhang, who have always been supporting me on my decisions and inspiring me to explore the beauty of life.

Jiangfeng

Fall 2015

Ann Arbor

TABLE OF CONTENTS

LIST OF TABLES

LIST OF FIGURES

ABSTRACT

Hydraulic fracturing, which is a fast-developing well-stimulation technique, has greatly expanded oil and natural gas production in the United States. As the use of hydraulic fracturing has grown, concerns about its environmental impacts have also increased. A sub-surface imaging radar that can detect the extent of hydraulic fractures is highly demanded, but existing radar designs cannot meet the requirement of penetration range on the order of kilometers due to the exorbitant propagation loss in the ground. In the thesis, a medium frequency (MF) band sub-surface radar sensing system is proposed to extend the detectable range to kilometers in rock layers. Algorithms for cross-hole and single-hole configurations are developed and tested based on simulations using point targets and realistic fractured rock models. A super-miniaturized borehole antenna and its feeding network are also designed for this radar system. The antenna makes use of a composite ferrite core and has dimensions of $\lambda_0/35 \times \lambda_0/1500 \times \lambda_0/1500$ that can fit within a borehole and shows a decent radiation efficiency of 10% even with a conducting cylinder passing through the center of the antenna.

Also application of imaging radars for sub-surface sensing frozen lakes at Arctic regions is investigated. The scattering mechanism of the lake ice is the key point to understand the radar data and to extract useful information. To explore this topic, a full-wave simulation model to analyze lake ice scattering phenomenology that includes columnar air bubbles is presented. The proposed model can handle complex interactions between high density air bubbles and rough ice surfaces. Based on this model, the scattering mechanism from the rough ice/water interface and

columnar air bubbles in the ice at C band is addressed and concludes that the roughness at the interface between ice and water is the dominate contributor to backscatter and once the lake is completely frozen the backscatter diminishes significantly.

Radar remote sensing systems often require high-performance antennas with special specifications. Besides the borehole antenna for MF band subsurface imaging system, several other antennas are also designed for potential radar systems. Surface-to-borehole setup is an alternative configuration for subsurface imaging system, which requires a miniaturized planar antenna placed on the surface. Such antenna is developed with using artificial electromagnetic materials for size reduction. Furthermore, circularly polarized (CP) waveform can be used for imaging system and omnidirectional CP antenna is needed. Thus, a low-profile planar azimuthal omnidirectional CP antenna with dimensions of $0.5\lambda_0 \times 0.2\lambda_0 \times 0.06\lambda_0$, gain of 1dB and bandwidth of 40 MHz is designed at 2.4 GHz by combining a novel slot antenna and a PIFA antenna.

CHAPTER I

Introduction

1.1 Motivation

"The oil reserves in the world only lasts for 30 years!" for many years, I still remember my primary school teacher told us to save energy by turning off lights when we leave the classroom. However, after two decades, the worries about the oil reserves seems to be less necessary than ever before – recent technological advances have made available a huge amount of oil and natural gas reserves, which were previously believed to be inaccessible or nonexistent. A new technology known as hydraulic fracturing (fracking) has been widely adopted by the petroleum industry to release the trapped gas and oil in shale rock. Briefly speaking, the hydraulic fracturing process involves injecting a mixture of pressurized water, proppants, and special chemicals into wells to create small fractures in subsurface rock layers as channels to transport the trapped oil and gas from the surrounding area into the pipeline and out of the earth. An overview picture is shown in Figure 1.1[1].

Modern rock fracture generation is a sophisticated engineered process intended to create fracture networks in a desired distribution pattern that is confined to the targeted area. During the process of hydraulic fracturing, observing the fracture distribution and overall dimensions is critical to determining the accurate parameters of reservoir stimulations, optimizing the production efficiency and leading to a successful well completion [2]-[4]. More importantly, with increasing number of hydraulic fracturing sites, concerns about its environmental and public

health impacts have significantly grown. One of the most concerning issues pertains to is the potential of aquifers contamination with hazardous chemicals that are injected into underground rocks. With proper fracture monitoring, the fracturing operations can be carefully managed and regulated to lower the risk of hazardous chemical to reach aquifers.

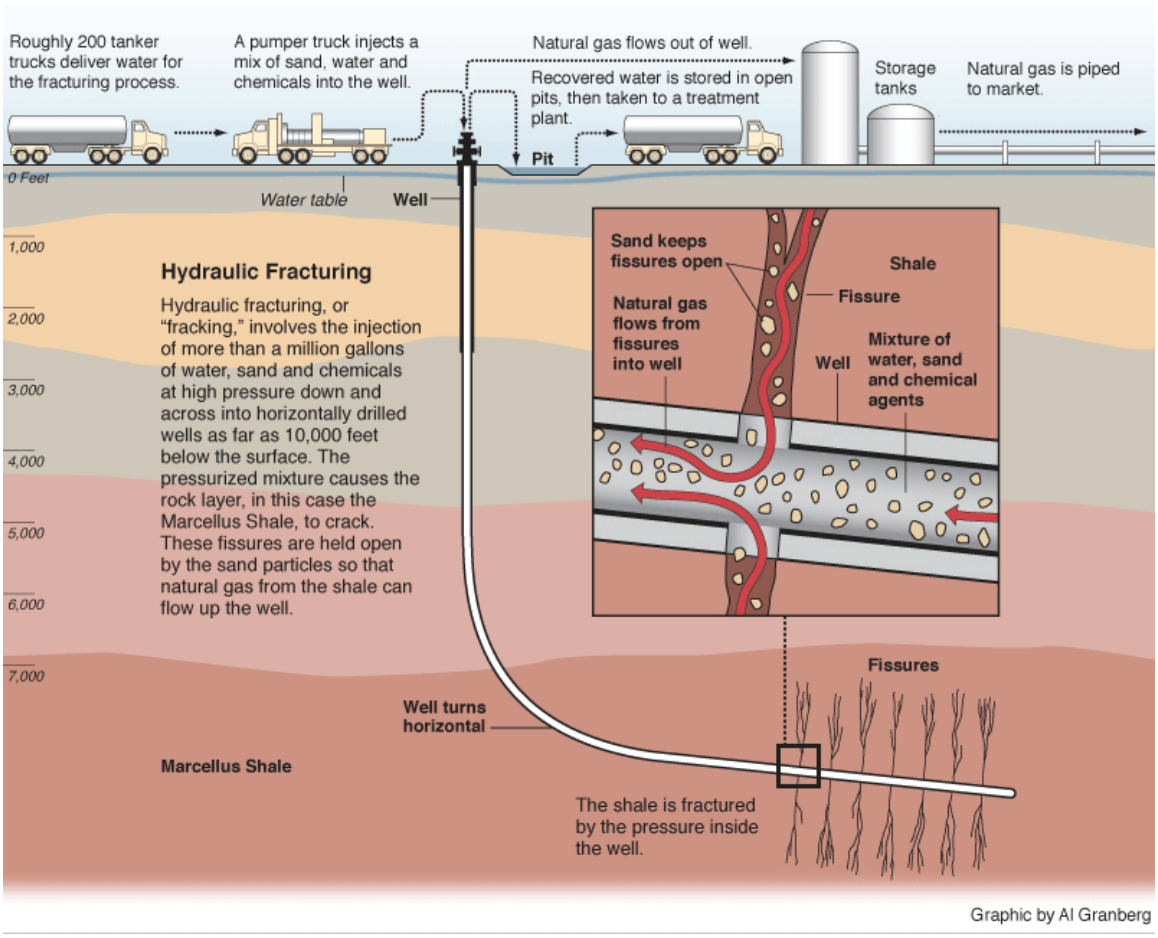

Figure 1.1. Hydraulic fracturing overview [1]

The most common and simplest method of monitoring is measuring the pressure during the injecting operation. Along with the knowledge of rock formation properties and fluid amount being injecting into the well, a few basic fracturing parameters can be roughly estimated [5].

Microseismic mapping, which is based on the observation of mini-earthquake events induced by fracturing process, is used to pinpoint fracturing and aids in well stimulation [3]. Since 1970's, microseismic measurements have been reported and are now widely applied in

fracturing sites [6][7]. Accuracy of microseismic mapping depends on the distribution and the sensitivity of sensors. Multiple offset wells and a large number of seismic sensors are often required to map the fractures and their extent [8]. For single-hole setup, the ability to detect the particle motion, measurements with high signal-to-noise ratio and full spectral bandwidth are required.[7] Microseismic detection is also a dynamic mapping method, which only shows new generated fractures while the natural existing fractures will be hidden from the detection.

Methods based on radioactivity of the underground materials and radioactive illumination are also used for the fracture monitoring. However, the use of radioactive sources is costly as regards to storage, transportation and recycling of the hazardous radioactive materials and increases the risk from health damage to site workers.

Nowadays, some electromagnetic (EM) subsurface mapping methods have been proposed to detect the fractures in the rock layer. However, most mapping methods are performed at the frequencies around 100-200 MHz at upper VHF band [9]-[14], requiring high power transmitters and highly sensitive receivers. Such systems have very limited penetration range into soil due to the exorbitant propagation loss in the ground. The existing fracture detection can only locate targets tens of meter from borehole. The EM based reservoir mapping method has not been developed yet. Generally, oil and gas-bearing reservoirs are located at the depth of 1000~3000 meter and the horizontal well can extend laterally as far as 2500 meter. Therefore, a penetration distance for electromagnetic waves at upper VHF band is the major bottleneck for mapping.

In order to extend the propagation distance from tens of meter to kilometers, we propose to use a lower frequency band such as MF band (300 KHz - 3 MHz) to reduce the signal attenuation. To make this clear, consider wave propagation at 2 MHz within a soil medium having 12% of humidity, the imaginary part of soil permittivity ε" is about 0.1, and this gives an

attenuation coefficient of 0.009 dB/m [15]. For this attenuation coefficient, the penetration distance can extend to as high as 2.5 kilometer with a round-trip propagation loss of lower than 50 dB. On the contrary, using the same dielectric parameters at 200 MHz, the penetration distance reduces to 25 meter for the same propagation loss.

However, an imaging radar system operating at MF band is a very challenging design and more importantly to configure such radar into an imaging system with desired resolution has not been reported in literatures. The large wavelength and the limited absolute bandwidth increase the difficulties on both imaging algorithm and antenna design. The following sections will discuss existing radar system that maps subsurface targets and conventional antenna designs for such radar system. These sections will also stress the specific problems as one lower the operating frequency to MF band.

1.2 Ground Penetrating Radar and Sub-surface Sensing

Using electromagnetic fields to map a subsurface region has a history of more than 50 years while many major technologies has been developed in recent two decades, along with the evolution of the computers [16]. Now the term ground penetrating radar (GPR) refers to many different techniques that uses radar pulses to image the subsurface in different applications, including archaeology discoveries[17], building inspection [18], and drilling [19][20], operating in different media varying from natural materials, such as rock, soil, ice, fresh water, to man-make composites, like concrete or asphalt. In general, GPR uses microwave to probe the target region to detect changes in material property contrasts within the medium, such as discontinuities in permittivity and conductivity. Reflection and transmission modes are both employed in different scenarios. A GRP transmitter (TX) emits energy into the medium, when the transmitted

wave encounters an object or a boundary between different media, scattered waves is generated and recorded by the GPR receivers (RX). The emitted energy can be a short-pulse or in the waveform of a swept frequency continuous wave. But both of them can be analyzed in time domain by applying Fourier Transform if necessary. Knowing the time delay of received signals from different receivers at different positions, the scatterer positions can be calculated. In lossy dielectric medium, EM waves will penetrate to some depth before being absorbed. The medium conductivity, the transmitted frequency and the radiated power all will limit the penetration distance. Basically, higher frequencies do not penetrate as far as lower frequencies but higher frequencies may provide better resolution. This results in a trade-off between the penetration distance and the resolution when choosing the operation frequency of a GPR. GPS systems also require lateral motions and proximity to the target for accurate geolocation.

1.2.1 Borehole GPR

GPR platforms (RX and TX) can be either placed on the ground or inside boreholes. These two kinds of GPRs are often referred as surface GRP and borehole GPR, respectively. Borehole GPR is physically limited by the geometry of a borehole. Consequentially, many special requirements and design challenges have to be met during the borehole antenna design process. Many different borehole GPRs have been reported; some are operating in a single borehole, similar to a monostatic radar system (Figure 1.2 (a)); some are establishing links between two boreholes, like a bistatic radar system, also known as cross-hole GPR (Figure 1.2(b)); and some are from a borehole to the surface, known as surface-to-borehole GPR [21].

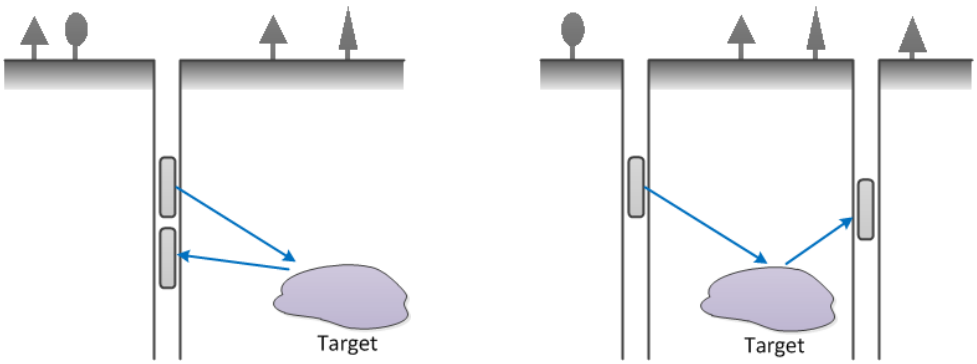

(a) (b)

Figure 1.2. Schematic representation of borehole GPR configurations. (a) single-hole measurement. (b) cross-hole measurement.

Normally, considering the cost of drilling a well, borehole GPR system tends to use as few boreholes as possible to cover the entire mapping region, and thus requires a larger penetrating distance than a normal surface GPR does. This is another reason why most of borehole GPRs operate at a low frequency band. The diameter of a borehole to place the GPR is often less than 10 cm, which is only a very small portion of a wavelength at the usual operation frequencies, and antenna diameter has to be even smaller to be housed in a waterproof case. Dipole antenna with a thin, long shape is often adopted as the transmitter or the receiver antenna for borehole GPR. Therefore, the radiation pattern is usually considered to be omnidirectional at azimuth plane with the maximum directivity at boresight direction. The omnidirectional antenna pattern limits the azimuth resolution.

1.3 Antenna Design

One of the main challenges in low frequency imaging systems comes from the difficulties associated with the antenna design.

1.3.1 Borehole antenna

Over the MF- and HF-band, frequencies of which span the 0.3 MHz through 30 MHz band, the antennas deployed for various communications and radar systems have been based

traditionally on the loop antennas or dipole antennas. Vertical radiators such as the dipole, monopole, top-loaded monopoles, T-antenna, Inverted-L antenna, and the Triatic and Trideco antennas, have been reported in the past [22]. Additional MF and HF antenna design structures have been proposed recently, such as the bi-folded monopole over infinite ground plane antenna structure [23], the V-shaped wire-structured fishbone antenna [24], the bi-conical antenna [25], the compounded log-periodic dipoles (LPDA) with monopole antenna structure [26], vertically radiated double rhombus antenna [27], and the parallel-plate antenna [28]. All of the aforementioned antennas are both physically and electrically large, making it extremely difficult to adapt for boreholes with maximum diameters less than 15cm. Furthermore, many of the proposed antennas require the presence of an infinite ground plane at their base for proper operation. These include monopole, the folded monopole, and the compounded LPDA antennas. Different size miniaturization schemes of different HF-antennas have been proposed recently. A small quarter-wavelength microstrip antenna with over 50% reduction in size has been proposed [29]. Also, a flat spiral rectangular loop antenna [30] was proposed as an HF antenna for RFID systems. Using air-core high quality factor inductive coil (Q>3000) and capacitive loading on a monopole antenna has achieved a large miniaturization factor [31], and the 2MHz version has reported to have a lateral dimension of $\lambda_0/150$ and a height of $\lambda_0/300$ [32]. Despite these size reductions, the resulting antennas are still physically large in two-dimensions, which is impractical for boreholes. A low profile multi-frequency HF antenna design was also proposed for coastal radar applications [33]. It consists of a meandering line antenna composed of helical elements and switchable folded arms. The antenna is 90 cm high with 60 cm diameter.

While the overall antenna length is acceptable, its diameter is much larger than the borehole diameter. Recently, the helical antenna operating in broadside mode was proposed for

communication applications at HF-band [34]. The helical antenna is inherently broadband and of cylindrical structure, hence suitable for operation in the borehole environment. It was demonstrated in [34] that a helical antenna of 10 cm diameter has an azimuthally uniform radiation pattern when operated in free space at 20 MHz. Another paper reports that a ferrite loading dipole array antenna at 20 MHz is able to conform to a sonde with diameter of 54 mm [35]. The scaling to 2 MHz without the use of proper antenna miniaturization schemes would result in substantially large diameter size that is incompatible with the borehole diameter.

1.3.2 Miniaturized Planar Antenna

As mentioned before, the ground-to-borehole GPR establishes a link between borehole and the surface. Planar antenna array is often deployed on the surface as TX or RX. As the operation frequency goes down, the increasing antenna size becomes a problem when considering the mobility of the system. The effort on shrinking the antenna size would be important to the radar sensor design.

In the past decade, many approaches for miniaturization of planar antennas have been proposed. For example, by placing a shoring wall at the end of a rectangular patch, the resonant frequency is equivalent to that of a patch having exactly twice the length and thus the size can be decreased by a factor of two, known as quarter-wavelength resonance [36]. The partially shorted patch, also referred as planar inverted F antenna (PIFA) presents a 60% reduction in frequency or size [37]. Another technique, similar to the inverted F method, is to insert a shoring pin at a proper position on a probe-fed circular microstrip patch [38]. However, designs based on these approaches yield antenna structures whose input impedance values and operating frequencies are very sensitive to the positions of the shorting post and the feed probe [39]. In addition such antennas produce exorbitant cross-polarized radiation [40]. Another approach for miniaturization

is based on modifying the geometry of the patch itself. Folded-patch antenna has a longer physical length along the non-radiating edge to form a standing wave [41]. Also slots or a notch on the patch have been used to cut off the surface current, so that it can re-distribute along a longer path [42]-[44]. Employing high-permittivity substrates is another useful method to reduce the size [39][45]. But the high dielectric constant materials will increase the antenna weight, cost, and in some cases lowers the antenna efficiency due to the higher dielectric loss-tangent of high dielectric materials.

Another approach could be applying novel artificial materials which offer new perspectives of reducing the size of planar antennas. By engineering the electromagnetic properties of the artificial material or surface, antenna designers can achieve much higher miniaturization than using conventional size reduction methods [46]-[51]. However, an important issue related to design of small antenna is the size of the artificial material substrate itself. In past, miniaturization factors reported in the literature only concern themselves with reporting the size of the antenna elements. This may be acceptable when miniaturized antennas are used as elements of a large array with a large ground plane. For single element applications, the antenna size should also include the size of the artificial material substrate which is usually much larger than the element itself.

1.3.3 Azimuthal Omnidirectional Horizontally/Circularly Polarized Antenna

Azimuthal Omnidirectional antenna gives radar system $360°$ azimuthal coverage, which is desired by surveillance radars and some imaging radars. Most systems with detection of signal direction of arrival require an omnidirectional radiation pattern [52]. For a polarimetric radar system, both horizontal and vertical polarizations are required to measure Stokes' matrix. Most of azimuthal omnidirectional antennas are polarized vertically, such as dipole antenna [53][54],

microstrip patch antenna [55] and slot antenna [56]. That is, their omnidirectional plane coincides with the H-plane. To achieve an omnidirectional horizontal polarization, loop antennas [57]-[59] and Alford-loop-type structure [60][61] are widely employed. Slot antenna only radiate on one side can also have a horizontal polarized azimuthal omnidirectional pattern [62].

Circular polarized waves are employed in many radar systems. In general, the reflection from a flat surface or sphere has opposite direction of circular polarization, which enables selecting reception of reflection or transmission. If TX and RX are designed with same sense of circular polarization, transmission or double-reflection signal will be received; otherwise, it will be the single-reflection signal from scatterer. This idea has been used in rain-clutter suppression [63] and in precipitation mapping [64][65]. For transmission through the ionosphere, because of the unknown amount of Faraday rotation, the orientation of linearly-polarized signal cannot be predicted [66]. An omnidirectional circularly polarized antenna can be implemented by combining several directional CP antennas mounted on a cylinder to cover the entire horizontal plane [67]-[69]. If two linearly polarized omnidirectional antennas are combined with phase delay structure design, the circularly-polarized omnidirectional pattern can be realized [57][62][70]. Most of these antennas have complex 3D structures occupying large volume. Planar antenna designs with omnidirectional CP pattern have also been reported, but the omni-directionality is poor and the axial ratio exceeds the 3dB limit at certain directions on the omnidirectional plane [71][72].

1.4 Thesis Contribution

The thesis proposed an MF band subsurface hydraulic fracture imaging radar system. The imaging algorithms and antenna designs are covered in the thesis, as well as a few topics related to potential implementations to the subsurface imaging radar. The content of the thesis can be

summarized in the flowchart shown in Figure 1.3. A brief introduction to each topic will be discussed in this section.

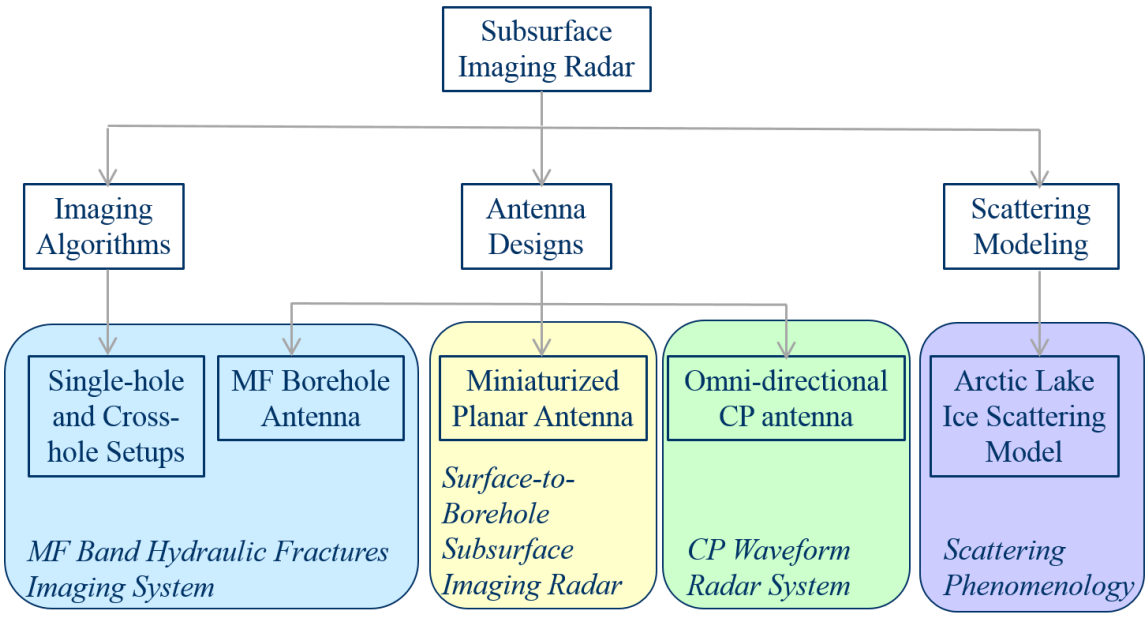

Figure 1.3. Thesis content overview.

1.4.1 Chapter II: Medium Frequency Band Synthetic Aperture Radar for Sub-Surface Imaging of Hydraulic Fracture

This thesis proposes a borehole synthetic aperture imaging radar system for hydraulic fracture detection application for the first time. The proposed system operating at medium frequency band around 2 MHz, which is selected to increase the penetrating distance. Subsequently, many challenges of low frequency radar system are discussed and solved. Borehole antenna design at 2 MHz is one of most important ones. Cross-hole and single-hole imaging algorithms are also challenging designs. Especially, the narrow bandwidth, due to the nature of electrically small antennas, that limits the range resolution and prevents one from using time-gating technique to isolate transmitter (TX) and receiver (RX) antennas. In the thesis, two setups are studied to solve these challenges.

The cross-hole setup uses a pair of borehole antennas in different wellbores. Consequently, a bistatic imaging radar can be configured to detect and monitor the hydraulic fractures. The concept of synthetic array is applied to the system, which by sweeping the location of TX or RX antennas and collecting phase coherent measurements array synthesis is performed. Post-processing the data allows for forming a virtual antenna array with a narrow beam to achieve fine resolution. Regarding TX/RX isolation, traditional ground penetrating radar can transmit a pulse and analyze its reflected signal. With a wide-band frequency spectrum, one can obtain a fine range resolution and eliminate direct-link signal by applying time gating to the received signal. In this setup where the antenna has limited by the bandwidth, a continuous wave (CW) or a narrowband signal does not permit time-gating to filter out the direct-link signal which is by many orders of magnitude larger than the intended scattered filed from desired targets. A beamforming technique named “adaptive null generation” is invented to control the array pattern in a manner in which a radiation null is always pointing to the RX antenna when steering the main beam of TX array.

Another imaging technique called single-hole setup is devised that makes use of a frequency-tunable feeding network to effectively increase the bandwidth of the radiated signal. In this scheme a stepped frequency waveform is used for the radar and the antenna is tuned accordingly to match the transmitter signal. Basically for a duration of time larger that round-trip delay the transmitter transmits a CW signal and wait until the receiver receives the echoes before transmitting the next frequency. Synthesizing the received signals at all frequencies mathematically, a short pulse can be generated to achieve range resolution and direct-link suppression. This technique only requires one hole to place both TX and RX antennas. Applying the concept of synthetic aperture radar (SAR), elevation resolution and range resolution can be

achieved by the pencil beam of the array and the stepped frequency bandwidth, respectively. Finally, by steering the focusing spot, a two-dimensional image with angular symmetry along the borehole can be generated.

1.4.2 Chapter III: Super-Miniaturized MF Antenna for Borehole Radar Application

One of the main challenges in low frequency imaging systems comes from the difficulties associated with the antenna design. Within a narrow borehole and with a limited length, designing an antenna with impedance match and high efficiency over a wide bandwidth seems practically impossible. Antennas with high radiation efficiency can easily be designed when the dimension of the antenna is comparable to or larger than the wavelength at its operating frequency. At the frequency band around 2 MHz, a typical half-wave dipole antenna is about 75m long in free-space. For mobile applications instead of using such tall antennas, a short dipole or a small loop antenna is often used, but due to the fact that the radiation resistance is very low and smaller than the ohmic losses of the antenna and its impedance matching network, the radiation efficiency is usually lower than 1%.

For the proposed system mentioned above, a super-miniaturized borehole antenna working at MF band with the dimensions 98 mm × 98 mm × 4100 mm is developed. For miniaturization a novel ferrite-loaded non-uniform helical folded-dipole antenna is presented. This antenna can be inserted in boreholes and is shown to be capable of providing radiation efficiency as high as 50%. The ferrite core serves a high permeability material providing a large miniaturization factor. The core is designed as a composite of a bundle of small ferrite cylinders in such a way as to minimize the loss.

One practical issue involves the effect of feeding cable passing through the antenna. High power transmitters cannot be sent down with the antenna in the borehole, thus the antenna must be fed by a transmission line connected to a source on the surface. As will be shown, passing a transmission line, such as coaxial line, through the center of the helical antenna significantly reduces the antenna impedance match and its radiation efficiency. Two layers of disjointed cluster of ferrite core is considered to mask the effect of a conducting cylinder placed inside the antenna to mitigate the adverse effects of the transmission line at the center of the antenna. In this case, the radiation efficiency can still reach 10%.

To enable antenna being used in stepped frequency continuous wave (SFCW) radar system, a feeding network is designed to match the antenna input impedance to a 50Ω port with the frequency tunability in the range of 1.6 MHz to 2.8 MHz with a minimum gain of -25 dB.

1.4.3 Chapter IV: Scattering Phenomenology of Arctic Lake Ice

Besides the sub-surface imaging application, radar remote sensing is often applied at Arctic region where many frozen lakes have interested researchers. In radar remote sensing, extracting physical information from imaging results requires the knowledge of scattering characteristic of targets. The analysis of EM waves scattering from different targets and terrains has been classical work of electromagnetism for the previous century. Inspired by some polarimetric synthetic aperture radar measurements, lots of interest has been raised in exploring the scattering mechanism for ice in shallow Arctic lakes, wherein strong radiometric responses are seen for floating ice, and low returns are evident where the ice has grounded.

In this thesis, a numerical model for analyzing Arctic lake ice scattering phenomenology is studied [73], which is based on full-wave finite element method (FEM) solver (Ansoft HFSS).

The model handles most of the scattering mechanisms in the lake ice, including the rough ice/water surface, the inclusion of the columnar gas bubbles and all the interaction between them. The periodic boundary condition is applied and is carefully analyzed to give the corresponding far-field scattering coefficient of the random surface from the finite area simulation. Subsequently, some numerical simulation results are presented, including the bistatic scattering coefficient, the effect of the clear ice layer thickness, and the effect of bubble length with flat/rough ice/water interface. The research concludes that the rough ice/water interface usually dominants the C-band backscattering on the lake ice while the double-bounce reflection is negligible for most scenarios of Arctic lake ice.

1.4.4 Chapter V: Planar miniaturized antenna

Besides the scattering phenomenology analysis, high-performance antenna design is also important to a radar remote sensing system. In previous Chapters, a borehole antenna is introduced for single-hole and cross-hole setup of MF band subsurface imaging system. In this thesis, other antennas are also developed for potential radar systems. In another sub-surface imaging radar setup, the borehole antenna may talk to the antenna arrays on the surface, which is also referred as surface-to-borehole EM method. Surface-to-borehole imaging system requires a planar antenna array to be placed on the ground. At a low operation frequency, antenna size would become a burden to a radar system, and thus a miniaturized planar antenna is highly demanded. Such antenna is introduced in Chapter V.

As mentioned previously, artificial materials are used to help miniaturizing planar antennas. In this thesis, an artificial-material-based planar antenna miniaturization technology is studied. We propose a patch antenna design using a two-layer mushroom-like reactive

impedance surface (RIS) to miniaturize the antenna. RIS, known as meta-substrate, has shown to present the ability to miniaturize printed antennas, when served as the substrate for the antenna. However, the area of conventional RIS substrates is usually much larger than that of the miniaturized antenna. To solve this problem, an RIS structure with smaller unit cell size is needed.

Firstly, the properties and design procedures for RIS substrates are studied. It is shown that the lateral dimensions and the height of the unit cells can be reduced to $\lambda_0/51 \times \lambda_0/51$ and $\lambda_0/167$, respectively, while the dielectric constant is kept below 3.5 for keeping the cost and weight low, by using a two-layer mushroom-like RIS structure. Based on a surface impedance model, the dispersion diagram of the surface wave and the propagation characteristic of microstrip lines over such RIS substrate are studied. Then, a UHF band patch antenna working at 356 MHz is developed. The overall size of the antenna is reduced to $\lambda_0/11.4 \times \lambda_0/11.4$. The sensitivity of alignment of patch antenna and the RIS substrate is also analyzed. Different sizes of the RIS substrate and the ground plane are tested in the simulation domain. Finally, several prototypes are fabricated and the measured results are shown to agree with the simulation results very well.

1.4.5 Chapter VI: Small Planar Omni-Directional Circularly Polarized (CP) Antenna

The antenna designs introduced above radiate and receive linearly polarized waves. In radar and communication applications, an azimuthal omnidirectional circularly polarized antenna is often desired but existing designs have complex 3D structures and are large in size. In this thesis, a planar CP antenna having omnidirectional pattern within a ring area is developed, which is suitable for many potential CP waveform radar applications with space-limited scenarios. The CP polarization is synthesized by combining two linearly polarized and omnidirectional antennas

and feeding them with signals having the same amplitude but 90 degree phase difference. The first antenna is a slot antenna on a finite and small ground plane which is made to have an omnidirectional pattern on its E-plane. To achieve that, the radiation null on the E-plane that exists on conventional slot antennas is removed by constructing a parallel plate waveguide delay line between the two sides of the antenna and forming an antiparallel field distribution on the aperture of each side. As a result, the far field radiation from both apertures adds up in phase and becomes uniform. The other antenna consists of two PIFA elements which radiate omni-directionally on their H-plane. The feeding network splits the input power equally to excite both antennas and introduces an extra 90 degree phase delay for one of the antennas. The feeding network is realized by microstrip lines and is optimized to have an axial ratio lower than 2 within a bandwidth of 2-3%. The simulation results demonstrate that the antenna has a figure-eight pattern in elevation with a beamwidth of about 100 degree. The gain of this small antenna is 2dB with small fluctuation as a function of angle in the horizontal plane.

1.4.6 Appendix: Dual Polarized Antenna for Base Station Application

A side project has also been carried out during the dissertation research period and is listed as the appendix to the thesis.

Wideband systems allow very high spatial resolution in radar applications making them excellent candidates for see-through-wall and ground penetrating radars [74]. They are also used in high data rate communications such as wireless USB [75]. Wideband antennas are key elements for such systems. Dual polarized antennas offer additional information which can be used in clutter reduction and target identification in radar systems [76]. The additional

polarization can also be used as a diversity measure to improve the received SNR and/or increase the data rate in communication applications [77].

A dual polarized wideband directional Coupled Sectorial Loop Antenna (CSLA) is developed with matching and radiation characteristics suitable for base stations application [78]. A dual-pol planar CSLA is designed and optimized and is fed by two vertically placed slotlines under the radiating element. The antenna is placed in front of a metallic ground plane with a beamwidth of 65 ° and a compact size ($0.38\lambda_m \times 0.38\lambda_m \times 0.25\lambda_m$). The antenna is designed to work over 1710 MHz to 2170 MHz which covers three common frequency bands of mobile radio application. The measured results showed return loss better than 14dB over the operating band and more than 30dB polarization isolation.

CHAPTER II

Medium Frequency Band Synthetic Aperture Radar for Sub-Surface Imaging of Hydraulic Fractures

In this Chapter, we will introduce the proposed subsurface fractures mapping method at MF band with two different system setups.

2.1 Introduction

Hydraulic fracturing (fracking) is a relatively recent technique for releasing trapped gas and oil in shale rock by creating small fractures in subsurface rock layers using a mixture of pressurized water, proppants, and especial chemicals. Modern fracturing fluid stimulations are sophisticated engineered processes designed to generate fracture networks in a desired distribution that is confined to a targeted formation. During the process, mapping the fracture dynamics is critical for determining the accurate parameters of reservoir and to optimizing the production efficiency [2]-[4]. Nowadays, some electromagnetic subsurface mapping methods have been proposed to detect the fractures in the rock layer. However, most mapping methods are performed at the frequencies around 200 MHz at upper VHF band [9]-[12], requiring high power transmitters and highly sensitive receivers. Due to the exorbitant wave propagation loss in the ground, such electromagnetic subsurface mappings are limited to short distances from the fracking area. This of course is not very practical as the imaging radar must be very close to the targeted area. In order to extend the penetration distance from tens of meter to kilometers which

is the extent of a typical shale gas wellbore, we propose to use a much lower frequency band such as MF band (300 KHz - 3 MHz) to reduce the signal attenuation.

One main challenge in utilization of low frequency imaging radar systems pertains to the difficulties associated with the antenna design. At these frequencies the size of conventional antennas becomes prohibitively large. The literature concerning antenna miniaturization is vast [79]-[82]. Within a very narrow borehole (diameter ~10cm) and with a limited antenna length, the antenna for such system will suffer from low radiation efficiency and narrow bandwidth. For the proposed system, a super-miniaturized borehole antenna working at MF band with the dimensions 98 mm $\times$ 98 mm $\times$ 4100 mm has been designed (Chapter III). The antenna shows a good efficiency of 10~50% but only provides a narrow bandwidth of about 1 kHz. To alleviate this limitation a feed network is designed not only to match the antenna input impedance to a 50Ω port but also to enable frequency tunability in the range of 1.6 MHz to 2.8 MHz with a minimum realized gain of -25 dBi. A stepped frequency waveform that is synchronized with the tuning network of the antenna will allow the radar operation over almost an octave bandwidth. Using a pair of borehole antennas in different wellbores, a bistatic imaging radar can be configured to detect and monitor the progression of hydraulic fractures. Traditional ground penetrating radar can transmit a pulse and analyze its reflected signal. With a wide-band frequency spectrum, one can obtain a relatively fine range resolution and eliminate direct-link signal by applying time-domain gating to the received signal.

In this Chapter, the concept of borehole imaging system is introduced in Section 2.2. Then, a continuous wave (CW) imaging algorithm is proposed to apply to the MF band borehole fracture imaging system. This technique is discussed in Section 2.3, referred to as cross-hole or multi-hole setup. Another imaging technique takes advantage of the frequency tunability of the

feeding network. The proposed method makes stepped frequency measurements with CW signals at a series frequency points and then mathematically generates a short pulse to achieve range resolution and direct-link suppression. This technique only requires one hole to place both the transmitter (TX) and receiver (RX) antennas. Applying the concept of synthetic aperture radar (SAR), one can move antennas to form a synthetic array and obtain a relatively fine resolution along the direction of the well. Finally, with range and elevation focusing, a two-dimensional image with angular symmetry along the borehole can be generated. This single-hole imaging system is introduced in Section 2.4. Finally, Section 2.5 summarizes the paper.

2.2 Borehole Imaging System

The proposed subsurface imaging method relies on synthetic aperture beamforming. Basically miniaturized transmit and receive antennas are sent down a wellbore in steps with specific intervals smaller than half a wavelength at the lowest operational frequency in the band. For a fixed receiver position the received signal for all transmitter locations are recorded coherently. Then the receiver position is changed by one interval step and the transmitter is moved again along the borehole. This process is repeated so that the received signals are measured for all transmitter and receiver locations. Post processing of the receive data can yield radar image of the subsurface area with spatial resolution proportional to λ/D where λ is the wavelength in the rock medium and D is the length the antenna traveled in the wellbore (length of synthetic aperture). It is also important to mention that the proposed synthetic aperture array compared to the conventional airborne or spaceborne SARs, has a much smaller f/D and as a result better resolution can be achieved. The goal is to detect subsurface dielectric inhomogeneties and map the extent of such regions. Of particular interest to the method

presented in this paper is the fact a major solvent used in the pressurized water is salt that can change both the real and imaginary parts of the dielectric constant of the fractured area drastically. This change in dielectric constant of exist over areas that fracking occurs and it is this contrast that can be mapped by the proposed imaging radar.

2.3 Cross-Hole Imaging System

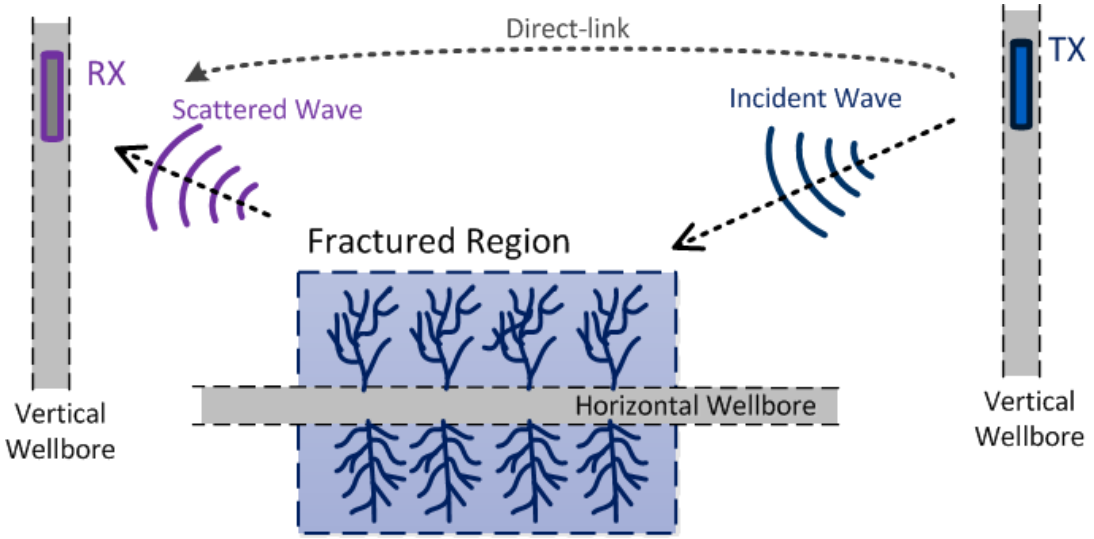

Figure 2.1. Cross-hole imaging system configuration.

The first proposed imaging algorithm requires one borehole for transmitter (TX) array and one or more boreholes for receiver (RX) arrays as the configuration setup shows in Figure 2.1. For this configuration let us consider a continuous wave (CW) signal waveform since the miniaturized TX and RX antennas that can be placed in wells are narrowband. One advantage of operating underground and away from the ground-air interface is that signal interference is very low. Also using CW signal allows for application of a very narrowband filter in the receiver, which in turn improves signal-to-noise ratio (SNR). Such bistatic radar system has very high receiver sensitivity in detecting scattered signal from subsurface regions with dielectric inhomogeneities.

2.3.1 Synthetic aperture beam forming

A one dimensional vertical array with omnidirectional elements can focus its beam along conical surfaces around the wellbore with different cone (elevation) angles. By controlling both TX array and RX array beams, the focus spot, which is the overlapped area of two conical beams, can sweep throughout the region in between the TX and RX wellbores. It is emphasized here that the depth and direction of the horizontal wellbore are known and therefore the elevation (cone) angles of the TX and RX beams can be varied together so that the beams overlap area can scan along the horizontal wellbore at different depths. The received signal strengths at different focus spots along the horizontal wellbore and different depths can be plotted to create a two-dimensional map of the fractured region. The resolution of such maps depends on the length of the synthetic array relative to the wavelength. As mentioned earlier in deep vertical boreholes long synthetic apertures can be formed that are comparable to the range of focus ($f/D<10$). Ideally, in the absence of natural drastic dielectric variations around the region of interest, the 2-D image in the vertical plane that contains the horizontal wellbore can image the extent of the fractured region where the maximum scattered field is generated. A miniaturized sub-wavelength antenna is guided down the transmitter well in a controlled manner so that the position of the antenna from the surface is known with a high degree of accuracy (a very small fraction of wavelength). An identical antenna is also guided down in the receiver well in a similar manner. A high-power source from the surface feeds the TX antenna and also a portion of the transmit signal is sent to the receiver by a surface transmission line for coherent (magnitude and phase) measurement of the received signal. During the measurement, the RX antenna is fixed at one position, while the TX antenna is moved along the transmitter wellbore and a series of received

data is collected. Then the RX antenna is moved to the next position and the TX antenna is moved to sweep the entire synthetic length of the TX array. This is done until the RX antenna has been moved to all locations over the receiver synthetic array length and all possible TX-RX position pairs are measured. Having the magnitude and phase of the measurement at each TX-RX position pair, the TX and RX array beams can be focused at different locations using post-processing.

2.3.2 Null generation

One issue with the proposed imaging approach outlined above is the direct signal linkage between the transmitter and receiver antennas. Basically, since the antennas are small and omnidirectional, the received signal from the transmitter is much stronger than the expected scattered signal from the target of interest. Hence, it is necessary to suppress this direct-link signal while focusing at the target region. To do this a novel beam forming technique is proposed to cancel out the direct coupling at the post-processing step. The RX array is located in front of the TX array, while the target area is chosen to be at a much lower depth. The top of the RX and TX arrays are chosen to be near the surface to guarantee the imaging area of interest fall below the bottom of the arrays. This way, as explained next, a radiation null for the TX array in the direction of receiver can be generated while keeping the focused beam in the desired direction. This approach can improve the isolation by a factor of 30~40 dB without increasing the complexity of the system hardware. Inspired by sum-and-difference direction finding antenna pairs [83], two successive elements of the array added with 180 °phase shift can be viewed as the element of a new array. This new element has a radiation null in the boresight direction. Modifying the 180 °phase shift slightly, the null direction can be shifted in upward or downward

directions to track the location of the receiver from the modified array element point of view. This approach is referred to as adaptive null steering while focusing. For example the complex feeding voltage coefficients to the modified array can be expressed as,

$$[a_n'] = (a_1 \quad a_2 \quad a_3 \quad ... \quad a_{N-1} \quad 0) + \\ + (0 \quad a_1 \quad a_2 \quad ... \quad a_{N-2} \quad a_{N-1}) \cdot (-1), \tag{2.1}$$

where $(a_1 \quad a_2 \quad a_3 \quad ... \quad a_{N-1})$ denotes the complex coefficients for the (N-1) array that allows for focusing in a desired direction. For near-field focusing the coefficients a_n can be computed from

$$a_n = A_n e^{jk_S\left|\overline{r_n} - \overline{r_f}\right|} e^{\alpha\left|\overline{r_n} - \overline{r_f}\right|} \cdot \left|\overline{r_n} - \overline{r_f}\right|, \tag{2.2}$$

where A_n represent windowing coefficients, $\overline{r_n}$ and $\overline{r_f}$ are, respectively, the array element and focusing positions. Also k_S and α represent the wave number and attenuation factor in the rock medium. This equation assumes the ground is homogeneous, but even for a layered medium the phase conjugation required for focusing can be obtained from Eikonal equation [84] assuming change in dielectric constant is slowly varying. It should be noted that the variation of the rock index of refraction as a function of depth can be estimated directly during the drilling process.

For adaptive null steering, instead of subtracting the coefficients in Eq.(2.1) for the broadside condition, the second row must be multiplied with term $e^{-jk_S(r_{n,m} - r_{n+1,m})} \cdot e^{-\alpha(r_{n,m} - r_{n+1,m})} \cdot r_{n+1,m} / r_{n,m}$ and then be added together. Here $r_{n,m} = \left|\overline{r_n^t} - \overline{r_m^r}\right|$ is the spacing between the n^{th} position of the TX antenna array and m^{th} position of the RX element, where $\overline{r_n^t}$ and $\overline{r_m^r}$ denote their positions.

2.3.3 Focusing process

The radar image is formed by focusing the synthetic arrays at different spot (pixel) over the monitoring area and pthen loting the signal amplitude pixel by pixel. Figure 2.2 shows the flowchart of the focusing process. $I(p)$ represents the signal when focusing at p^{th} pixel, which is obtained by multiplying the raw data V_0 with array factors a_{TX} and a_{RX}. Since the adaptive null generation is implemented on TX array, the TX array factor a_{TX} will also depend on RX antenna location. Thus, $a_{TX}(m,n,p)$ is a three-dimensional matrix, where m,n,p correspond to the indices of RX location, TX location and focus location, respectively. RX array does not have null generation, so the RX array factor matrix $a_{RX}(m,p)$ only has two dimensions: RX location m and focus location p. The raw data $V_0(m,n)$ is a two-dimensional matrix, which records the voltage when TX is at the nth location and RX is at the mth location.

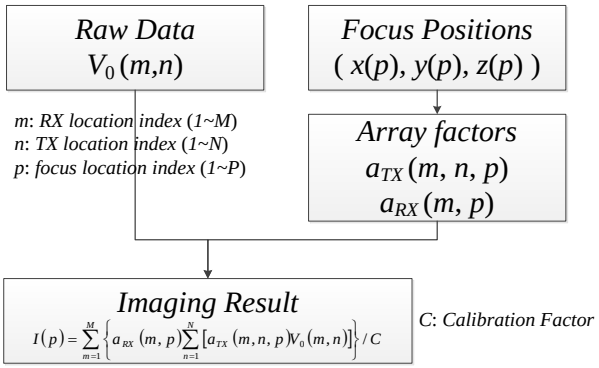

Figure 2.2. Flowchart of cross-hole system focusing process.

2.3.4 Imaging demonstrations

To demonstrate the performance of this imaging technique, several targets representing the fractured region in oil fields are generated, and then for typical wellbore configurations transmit and receive synthetic arrays are formed to plot the extent of the fractures. In this simulation, bistatic radar cross-section (RCS) of the target is simulated in a full-wave analysis (HFSS), and used in predicting the signals at the receiver. In order to preserve both the

magnitude and phase information, the complex RCS values as a function of incident and scattering angles are collected from the simulated results and stored as:

$$\sqrt{\sigma}\left(\theta,\varphi;\theta^{inc},\varphi^{inc}\right)=2\sqrt{\pi}R\frac{E_{scat}\left(\theta,\varphi\right)}{\left|E_{inc}\left(\theta^{inc},\varphi^{inc}\right)\right|}. \tag{2.3}$$

In addition to the scattered signal from the target, the direct-link signals from TX antennas to RX antennas, which are calculated by Friis transmission equation, is also considered.

The dielectric constant of the rock layer has to be determined at the operation frequency f_0 = 2 MHz. Since there is no good measurement data for shale rock at that frequency, an empirical formula for solid-rock permittivity provided in [85] (p.147) is used, which gives a permittivity of about 4 based on the measured density of shale rock of 2g/cm^3 [86][87]. The imaginary part of permittivity is estimated by the MHz band measurement of sandstone [88], since sandstone and shale are similar and both belong to clastic sedimentary rocks. [88] gives a maximum conductivity of sandstone to be around 0.01 mS/m, This is used to calculate the imaginary part of permittivity to be 0.1 at 2 MHz. Thus, we are using this number to estimate the propagation loss in our simulations. In field test, the rock properties may vary from site to site which can be measured and used to map the target correctly.

To begin, a point metallic target is initially considered. For simple calculation a metallic sphere with a radius of 10 m buried in a homogeneous rock with dielectric constant ε_r =4-*j*0.1 located at a local origin is chosen. This target in the rock medium shows a maxim RCS value of 30 dBsm, according to a full-wave simulation, shown in Figure 2.3. Note that the radius of the sphere is much smaller than the wavelength and thus its RCS is a function of wavelength. The simulated RCS of the sphere in the rock medium is four times of that in free space since the wavelength in the medium reduces by factor of two and the sphere has stronger scattering according to Mie solution [89]. Both RX and TX arrays are considered to have 40 elements with

vertical separation of Δ = 25 m between adjacent elements. The synthetic length of the arrays are L = 1000 m = 13.3 λ_{rock}. Bottom element of the TX array is placed at the coordinate (-1000m, 0, 250m), corresponding to horizontal distance of 1000 m away from the target and 250 m above it and the frequency is set to 2 MHz. Since RX array is not necessary to be placed on the plane of incidence (the plane that contains the target and the TX array), the RX array coordinates is set to be (1200m, 200m, 250m). Figure 2.4 shows the image of the detected target. In this setup, the proposed imaging system is shown to detect the relatively small spherical target (a = 0.26 λ_{rock}) at kilometers range. The 3dB depth and lateral resolutions are found to be 95 m and 145 m respectively. For this near-filed focusing system it is expected that the depth resolution be higher than the lateral resolution as the arrays are vertically oriented.

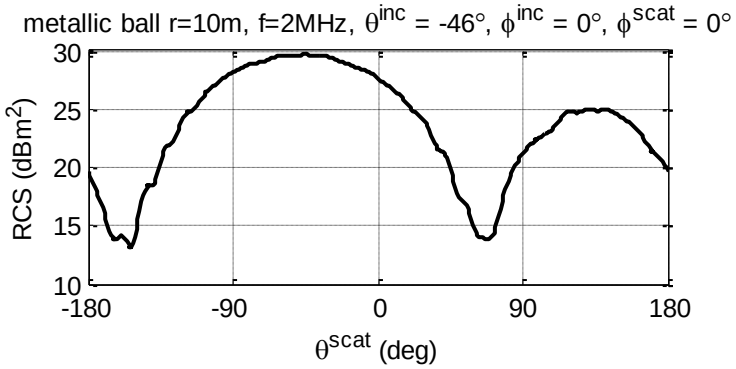

Figure 2.3. RCS of the point target with incident elevation angle of -46 °.

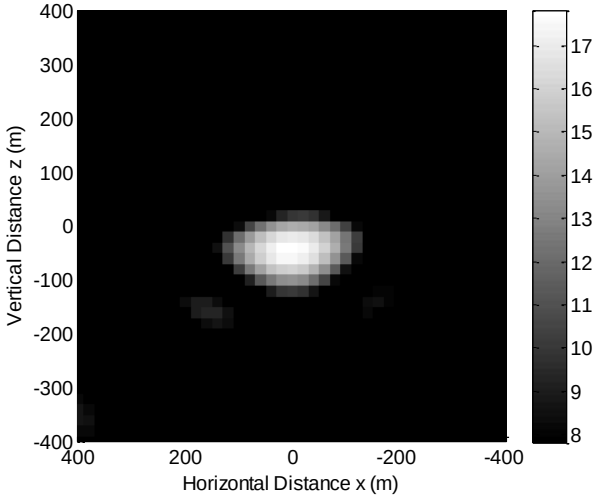

Figure 2.4. Cross-hole imaging result of a point target.

For the second simulation a cylindrical region having different dielectric constant from the surrounding rock is considered. The dielectric constant and conductivity of this region is chosen to be the same as that of an equivalent fractured region. Since in the fractured region, the separations between the adjacent cracks are much smaller than the wavelength, this region can be treated as a homogenous medium with higher conductivity than the surrounding area. Considering 9,000 cubic meter (2.3 million gallon [3] (p.114)) fracturing fluid injected into a cylindrical area with a diameter of 100 meter and a length of 1000 meter, the volume fraction of hydraulic fluid is ρ_{fliud} = 0.11%. The permittivity of the fractured region is computed from a dielectric mixing formula and is given by [85] (p.133)

$$\varepsilon_{frac} = \left(1 - \rho_{fluid}\right)\varepsilon_{rock} + \rho_{fluid}\,\varepsilon_{fluid} \quad . \tag{2.4}$$

If we use ε_{fluid} = 81-j9000 (conductivity σ_{fluid}=1S/m, 0.5% chemicals [90]), ε_{rock} = 4-j0.1, the effective permittivity of the fractured region can be found to be ε_{frac} = 4.08-j10.

In oil fields, the hydraulic fracturing process in the horizontal wellbore is usually divided into several stages [91]. Each stage is used to create cracks into surround rocks along a portion of the lateral length. To simulate the fractured region, cylindrical targets are generated with length of 400 m and with different radii for the purpose of comparison.

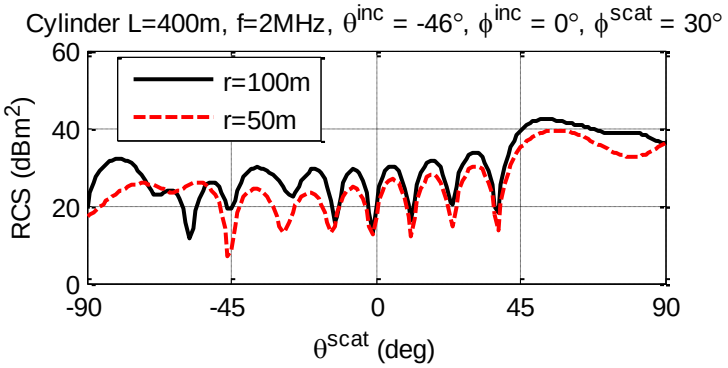

Figure 2.5. RCS of the cylindrical target with incident elevation angle of -46 °.

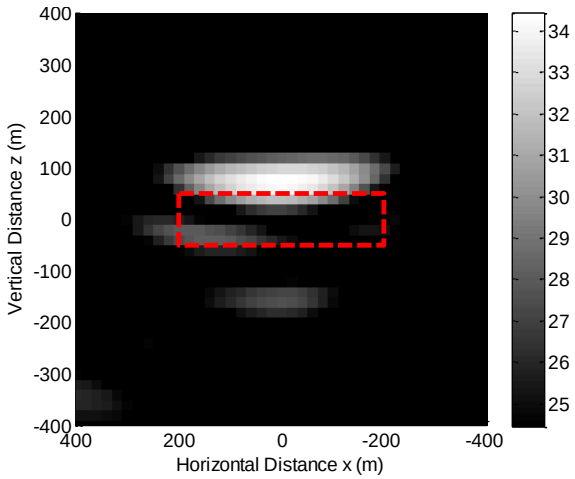

(a) Target Radius = 50m

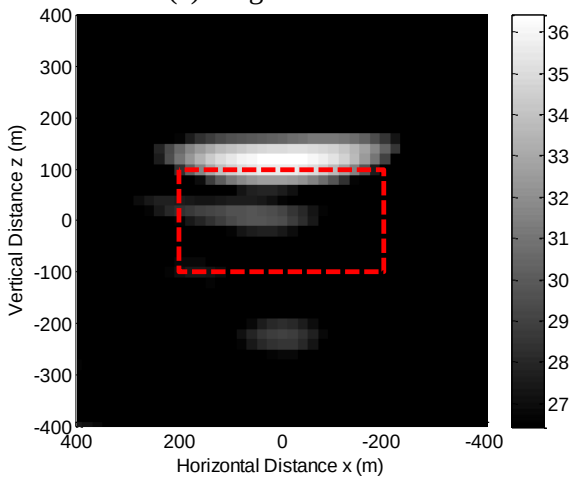

(b) Target Radius = 100m

Figure 2.6. Cross-hole fracture detection results using cylindrical targets with different radii

In Figure 2.5, the bistatic RCS of cylindrical targets having radii of 50 m and 100 m are simulated using HFSS. Figure 2.6 shows the radar images of the fractured region (gray scale map) and the actual cylindrical target boundaries (dash lines). Since the incident wave illuminates the region from the top-right side, and the wave cannot penetrate the fractured region due to the high conductivity of the fractures there, only the upper half surface of the cylindrical region can be detected. The detected boundary indicates the depth from the surface and the extent of the fractured region from the horizontal wellbore. This information is important for oil and gas companies estimating the volume of fractured region and for optimizing the fracturing

process. Figure 2.6 (a) and Figure 2.6 (b) show the simulation results for two cylindrical models having radii of 50 m and 100 m respectively. The images generated by proposed algorithm well estimates the upper boundaries.

The simulations and tests based on cylindrical model have demonstrated the feasibility of the proposed imaging system. However, due to the homogenous properties and specular surface of the model boundary, volume scattering from this model is ignored. The smooth cylindrical surface in the model produces significant specular reflection which in practice is not the dominant scattering mechanism. For more realistic simulations, a more complex fracture model is needed. As shown in Figure 2.7 (a), an inhomogeneous fractured region is generated by a MATLAB code. Fractures are presented by some thin rectangular planes with different sizes and random locations and orientations. To imitate the fractures in shale rock which is naturally formed by layers, rectangular planes in this model are oriented horizontally with a small angular variation from plane to plane, since the layers in shale rock are not necessarily perfectly parallel. There are also some smaller and narrower vertical rectangular planes in the model which represent the fractures generated during the hydraulic fracturing and connect layers. The plane on the bottom is located on the plane of the pipeline, which is the largest plane since the fluid pressure is the highest there. Other planes are growing from this plane but their sizes reduce statistically as they move away from the pipeline. The thickness of the each plane is about 1 cm. The complex dielectric constant of $\varepsilon_{fluid} = 81\text{-}j9000$ is used for the fractures.

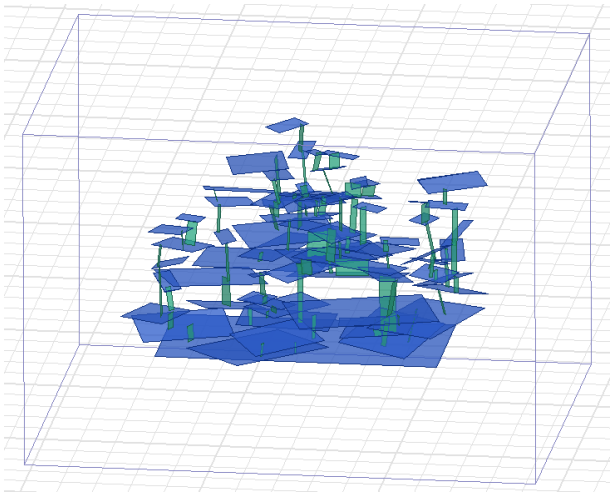

(a) Geometry of the Fracture Model

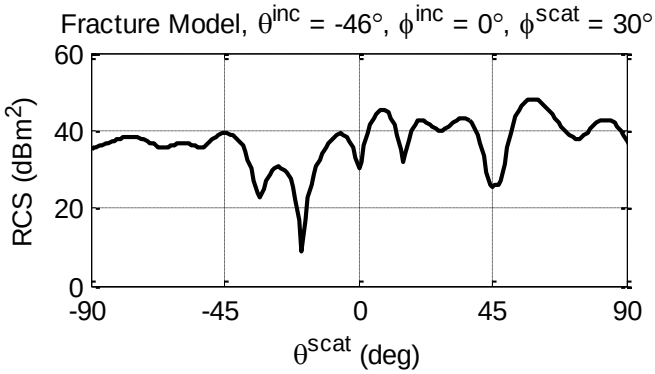

(b) RCS of the fracture model with incident elevation angle of -46 °.

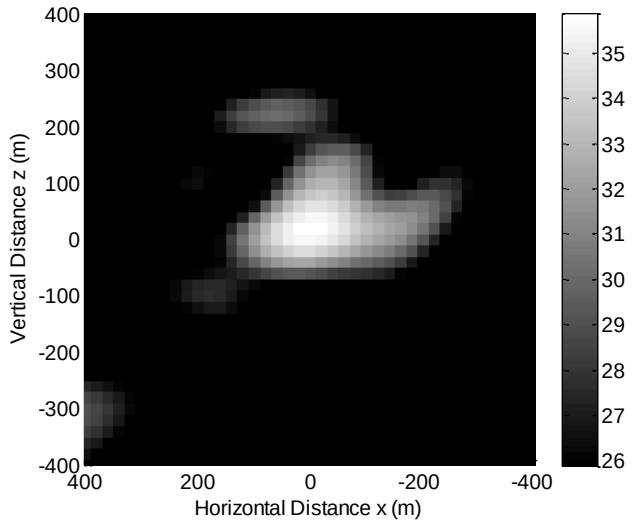

(c) Vertical Plane Image

Figure 2.7. Radar map of the fractured region based on the fracture model shown in (a).

The fracture model in Figure 2.7 (a) has 148 fracture surfaces occupying a volume of 400 m (length) × 300 m (width) × 250 m (height). The RCS of this target at incident angle of -46 ° is shown in Figure 2.7 (b). The radar image for this structure is shown in Figure 2.7 (c) and to some extent depicts the overall shape of the fractured region. Due to the resolution limitation, individual fractures cannot be distinguished but some small groups such as a few of highest fractures can be found in the mapping result at around z = 250 m. It is also worth mentioning that the spot on the left-bottom corner is caused by the sidelobe of the receiving array beam which is coming from the upper-left direction. If a tapered array coefficient is applied, the sidelobe level can be suppressed at the expense of losing some resolution. However, once using the low-resolution sidelobe-suppressed array coefficient to eliminate the aliasing images, one can switch back to normal resolution and observe the target with the knowledge of the aliased image positions.

2.3.5 Multi-RX-hole setup

As mentioned earlier this imaging technique based on focusing the transmitter and receiver has fine resolution in the vertical direction. To improve lateral resolution, particularly in a plane perpendicular to the line connecting the two boreholes, additional receiver boreholes are needed. In what follows few simulation scenarios are presented to show lateral resolution enhancement using multiple holes. Of course this makes the imaging and monitoring more expensive as multiple holes must be drilled.

In a scenario shown in Figure 2.8(a), two parallel horizontal wellbores are drilled and fractured on y=0 plane and y=400m plane. To distinguish the cylindrical fractured regions on two planes, multiply RX wells may be needed. If only one TX well (TX1) and one RX well (RX1) are used, the mapping result on *y*=0 plane shown in Figure 2.8 (b) will show the

cylindrical target on *y*=400m plane overlapping with the one on *y*=0 plane. If RX1-RX5 are all utilized to map the targets, these targets can be isolated laterally and will appear on *y*=0 and *y*=400m plane separately, as shown in Figure 2.8 (c)-(d).

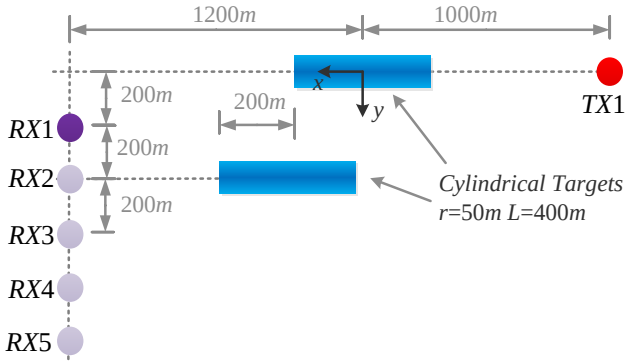

(a) Scenario setup top view: two cylindrical targets locate at y=0 plane and y=400m plane

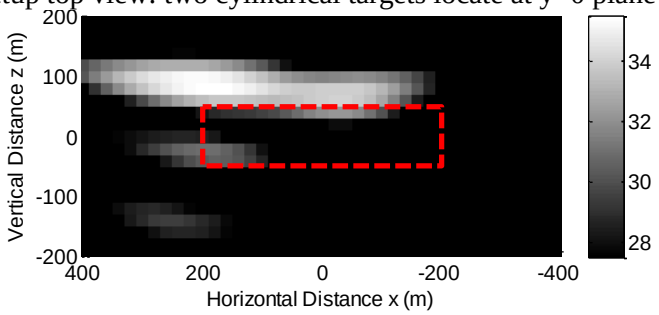

(b) Mapping result at y=0 plane using RX1 and TX1

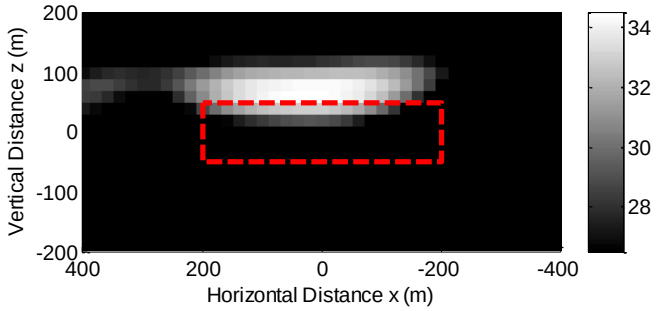

(c) Mapping result at y=0 plane using RX1~RX5 and TX1

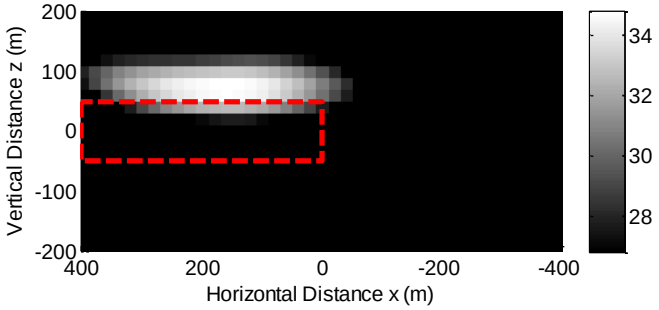

(d) Mapping result at y=400m plane using RX1~RX5 and TX1

Figure 2.8. Multi-RX-hole setup demonstration

2.4 Single-Hole System

The previous section presented the multi-hole fracture imaging system that is composed of a transmitter (TX) and receiver (RX) separated by a distance comparable to the target distance. CW signal is used for this system which reduces the complexity of the transmitter and receiver. Usually drilling wells for multi-hole approach is not cost effective. An alternative approach is to place the TX and RX antennas in the same borehole provided that enough isolation between the TX and RX antennas can be achieved. Figure 2.9 demonstrates the configuration of single-hole imaging system. Some monostatic radar systems use the same antenna to transmit and receive signal and isolation is achieved using time-domain multiplexing. However, in a short-range application such as the problem at hand, a typical round-trip time of the signal is on the order of microseconds (μs) and pulsed radars that require wide bandwidth are not practical for the available narrowband antennas. It is necessary to use two antennas for the purposes of transmitting and receiving individually. In this configuration, two antennas are separated by a short distance but large enough for electrical isolation.

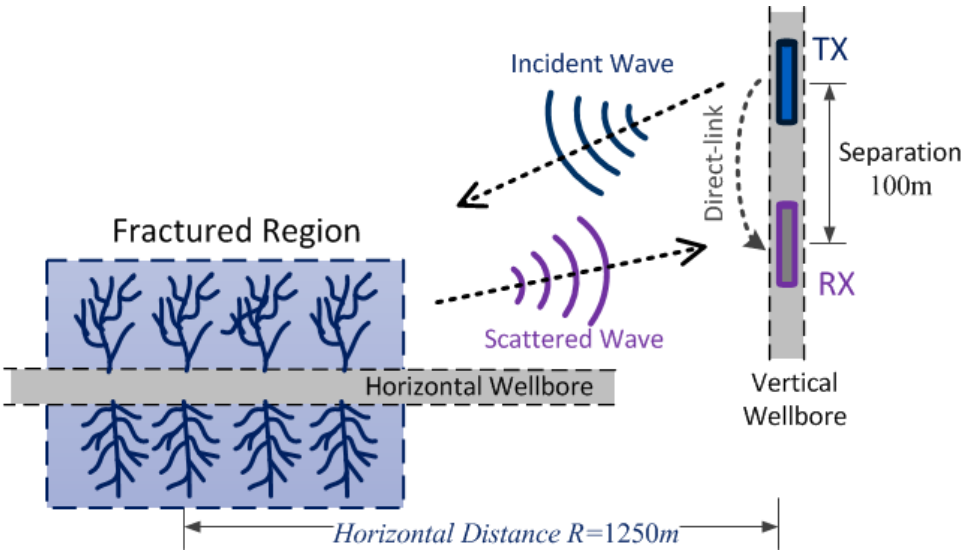

Figure 2.9. Single-hole imaging system configuration.

Similarly to the cross-hole imaging system, the single-hole setup takes coherent measurements of backscattered fields when both TX and RX antenna pair are moving along the vertical wellbore. Taking advantage of the phase and magnitude information, a vertical synthetic array can focus at different locations along a horizontal distance from the wellbore with fine resolution in elevation. However, this focusing is azimuthally symmetric and the knowledge of direction of horizontal wellbore is needed to map the extent of the fractured rocks. Different from the multi-hole system that has two sweeping beams from separated TX and RX arrays whose intersection defines the pixel of image, the single-hole system can only preform one-dimensional sweep. Hence another scanning scheme has to be introduced to map the target in two-dimension. Most synthetic aperture radars (SAR) use narrow pulse (wide bandwidth) to achieve range resolution. Limited by the antenna dimension, wide bandwidth small antenna design is not available. However, inspired by stepped frequency continuous wave (SFCW) ground penetrating radar (GPR) [92][93], one can use frequency tunable antennas to transmit a series of single frequency waveform within a wide spectrum and record the phases and magnitudes of the reflected waves at each frequency. During the post processing, by implement inverse fast Fourier transform (IFFT), time domain multiplexing can be synthesized. With a narrow synthesized pulse, not only a fine range resolution can be achieved, but also TX to RX isolation can be improved as will be discussed later. As a result, the single-hole system measurement process contains a two-dimensional frequency - position sweep. Each measurement is performed with a narrow-band CW signal. In this case, the signal-to-noise ratio (SNR) is expected to be very good as the instantaneous receiver bandwidth can be made very small.

2.4.1 Isolation

Compared to multi-hole system, the direct-link between the TX and RX antennas is much higher since the separation distance is much shorter. Here, the null-steering approach described before cannot be implemented. In a typical scenario, the scattered signal power will drop more than 180 dB from TX antenna to the target and scattering back to RX antenna. To prevent the scattered signal from being jammed by the direct-link signal, a TX-to-RX isolation close to 200 dB has to be achieved. In the proposed system, the spatial isolation and the time-domain isolation are applied simultaneously, and together they can provide the desired isolation level.

The wellbore antennas are folded spiral elements that present radiation null along their axis. Stacking the RX and TX antennas in the wellbore benefits from this arrangement in so far as isolation between the two antennas are concerned. However, if the RX and TX antennas are not far enough apart, the near-field coupling dominates and limits the isolation. Thus, it is necessary to study the mutual coupling between antennas by a full-wave simulation in their underground environment. Figure 2.10 demonstrates the simulated isolation between two folded spiral antennas stacked on top of each other as a function of center-to center distance. Note that, at frequencies close to the antenna resonance, it is difficult to match the antenna using the proposed feeding network, so the isolation data near the resonance are omitted. The isolations at the two ends of the tunable frequency range are lower than that in the center frequency. There is a similar trend with the efficiency curve as well. At the separation distance of 100 meter, the spatial isolation values over the band are lower than -50 dB.

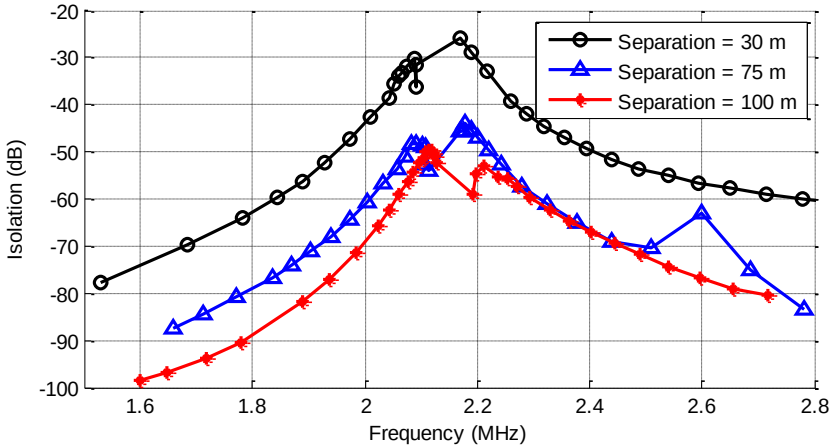

Figure 2.10. Isolations between two axial aligned antennas with different separations

Another approach to filter out the direct-link signal is time-gating. In time domain, in order to block the direct-link signal, the maximum effective pulse width should be less than the time delay between the two signals and this determines the minimum frequency bandwidth of the system. For a signal with a finite bandwidth, the synthesized time domain waveform shows side-lobes that depend on the window or taper function of the frequency domain data. The side-lobe level determines how much isolation in time domain can be achieved. It is noted that there is a tradeoff between the side-lobe level and the effective pulse width, as shown in Figure 2.11.

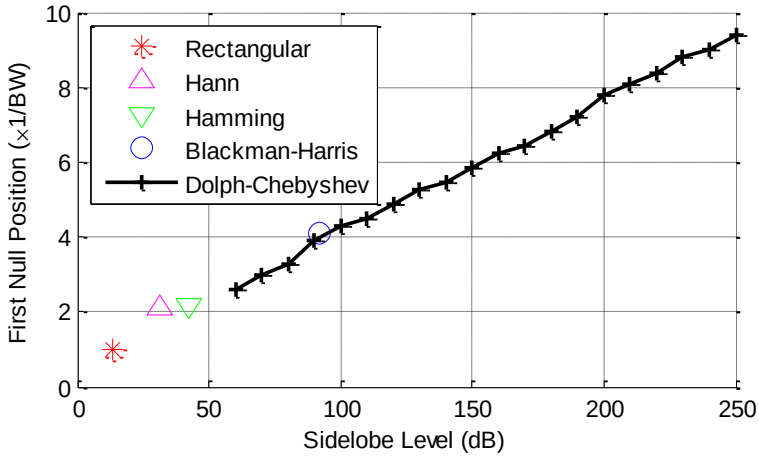

Figure 2.11. The tradeoff between window function's sidelobe level and effective pulse width

In this application the Dolph-Chebyshev window is used to suppress the sidelobes and maintain a desirable range resolution. This windowing function is optimal in that for a desired side-lobe level it has a minimum main-lobe width. It is also noted that this window function provides a constant level side-lobe [94].

The flowchart of time-gating process is shown in Figure 2.12, in which the input raw data is a two-dimensional array, corresponding to the stepped frequency samples and z-direction location sweep. Time-gated signal is obtained in the time domain and then is transformed to frequency domain to be used in the following process.

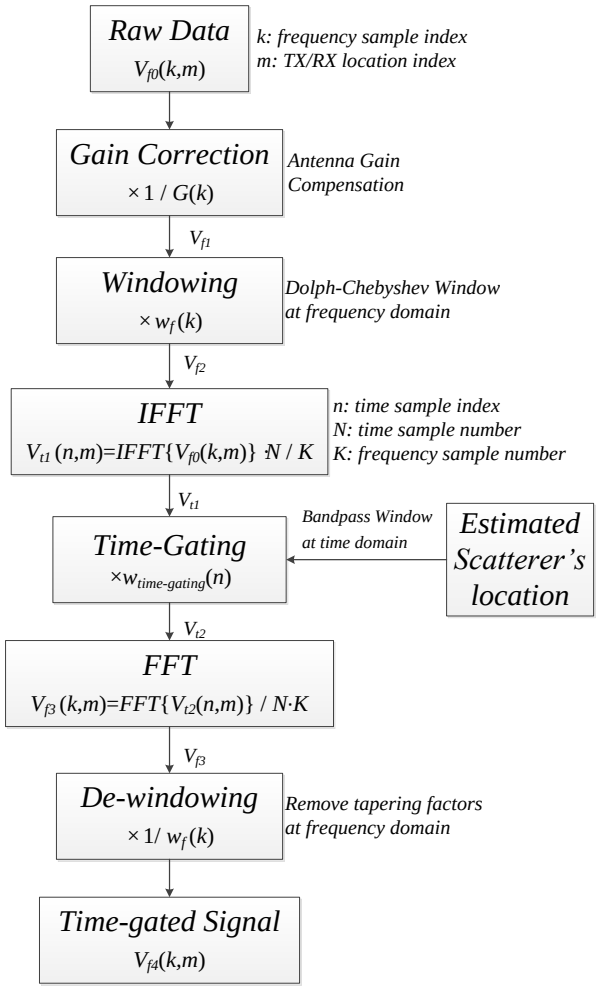

Figure 2.12. Flowchart of time-gating process

2.4.2 Focusing Process

The time-gated signals usually have large distortions over a fewer points at the edges of the frequency band, due to the renormalization edge effects [95]. To reduce its effect on the focusing process, some samples are eliminated. The truncated data is then multiplied by array factors a_0 to focus on each pixel of the mapping area. The array factors compensate the phase delays and propagation attenuations for different frequencies and different antenna locations, which can be determined by

$$a_0(k,m,p) = e^{j\frac{2\pi}{\lambda_{rock}(k)}(r_t(m,p)+r_r(m,p))} e^{\alpha(k)(r_t(m,p)+r_r(m,p))} \times r_t(m,p)\cdot r_r(m,p)\cdot w_{2D}(k,m) \quad (2.5)$$

The indices *k,m,p* correspond to frequencies, TX/RX locations and focus locations, respectively. r_t and r_r denote the distance between the focus and the TX/RX. The exponential terms in (2.5) take the phase delay and medium attenuation into consideration while the $r_t r_r$ term compensates the 1/*r* decay in the wave propagation. A 2-D window function w_{2D} is added into a_0 to reduce the sidelobe in the image. This function is chosen as a triangular window (-26dB sidelobe level). The flowchart of the focusing process is shown in Figure 2.13. It is noted that a calibration factor can be multiplied to the imaging result so that the loss in the system can be calibrated.

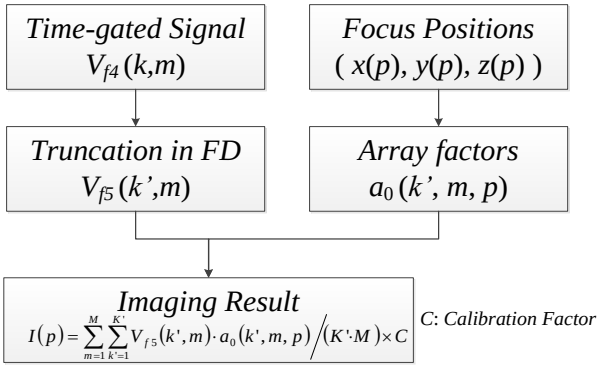

Figure 2.13. Flowchart of Single-hole focusing process.

2.4.3 Detectable Range

The detectable range is affected by two aspects, thermal noise level and the direct-link suppression. To estimate the detectable range, the system and environmental parameters in Table 2.1 are used. Also given in Table 2.1 are calculated noise power and received signal for the target at a horizontal distance of 1250 m. It is shown that the direct-link signal has been suppressed after time-gating by 180dB and it is 34dB lower than scattered signal level. After the focusing process, the image noise due to the direct-link is 52 dB lower than the image of the target.

Table 2.1. Main parameters in imaging process

Parameter	**Formula / Comment**	**Value (min/max)**
Source Power	P_0=1000 W	30 dBW
Cable Loss	L_C=0.3dB/100ft @ 2MHz	-5 dB
Antenna Realize Gain	G_t/G_r: includes loss and mismatch	-20 dB
Background Permittivity	$\varepsilon_r = \varepsilon_r' - j\varepsilon_r''$	4 – 0.1j
Attenuation Coefficient	$\alpha = k_0\sqrt{\varepsilon_r'}\tan\delta/2$	0.009 dB/m
Array Length	M = 40 with 25 m separation	1000 m
Bandwidth	1.6~2.8 MHz, K=121 samples for time-gating, K'=91 smaples for focusing	1.2 MHz
Spatial Isolation	I_{spac}, Separation = 100 m	>50 dB
Time-domain Isolation	I_t, Pulse width = 7.6 μs	150 dB
Direct-link Signal Power	$P_{dir} = P_0 L_C^2 / I_{spac}$	-30 dBW
Time-gating Leakage	$P_{n2} = P_{dir} / I_t$	-180 dBW
Target Distance	Horizontal Distance = 1250 m	1266 m / 1733 m
Target RCS	Fractured region	~1000 m^2
Scattered Signal Power	$P_S = \frac{P_0 L_C^2 G_r G_t \lambda^2}{(4\pi)^3 r_1^2 r_2^2}\sigma \cdot e^{-\alpha(r_1+r_2)}$	-156 dBW / -137 dBW
Direct-link Power After Time-gating	Apply time-gating on direct-link signal only	-198 dBW / -190 dBW
Thermal Noise Power	$P_n = k_B TB$, B = 10 Hz	-194 dBW
Image Magnitude	I, after calibration	31 dBsm
Direct-link Leakage Noise in Image	I_{n2}, apply focusing algorithm on the direct-link signal only	-21 dBsm
Thermal Noise in Image	I_{n1}, apply focusing algorithm on the thermal noise only	-40 dBsm
Total SNR	SNR = $I / (I_{n1}+I_{n2})$	52 dB

As the target distance changes, the scattered signal, time-gating leakage and the noise level is plotted in . It demonstrates that as the distance increases, the scattered signal power drops exponentially due to the loss of the rock medium. This reduces the single-to-noise ratio (SNR) since the thermal noise power is constant. Thus, the noise performance sets the upper limit of the detectable range. In this stepped frequency continuous wave system, the noise bandwidth is very low. With using dielectric constant of ε_{rock} = 4-0.1j, it still takes kilometers of propagation distance to drop the scattered signal level below the noise floor. As shown in Figure 2.14, assuming source power of 1000W, the target RCS of 1000 m^2 and the SNR threshold of 0 dB, the maximum detectable range will be around 2700 m.

On the other hand, the lower limit of the detectable range is set by direct-link signal suppression. When the distance is short, the effective pulse width of the time-gate has to be narrow, which increases the sideband level and results in a large leakage. As indicated in , the minimum detectable range corresponding to signal-to-leakage of unity is about 400 meter. In order to improve this, the separation between TX and RX antennas can be increased, or use wider absolute bandwidth. It is interesting to point that when focusing distance is shorter than the minimum detectable range from , some measurement points may suffer from large direct-link interferences but the overall imaging result may still be useable. As will be discussed in Figure 2.15, the minimum detectable range can be as short as 250 m with minor degradation on resolutions.

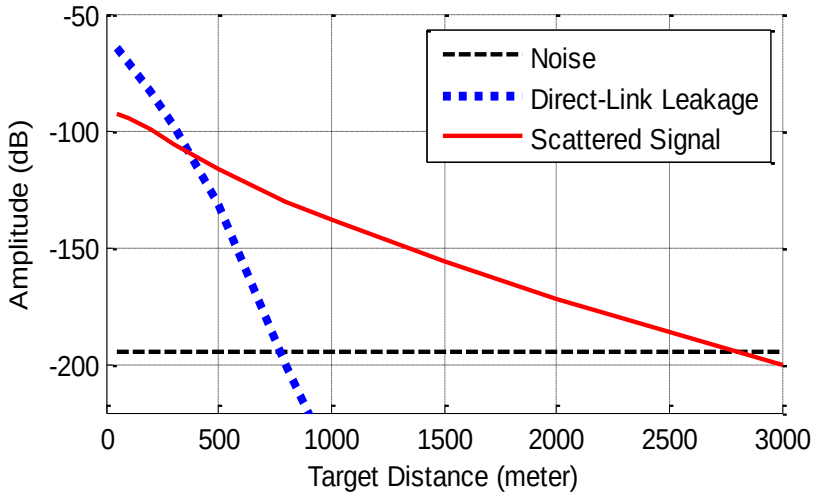

Figure 2.14. Comparison of scattered signal, time-gated direct-link and noise level, as function of target distance

2.4.4 Resolution

Similar to synthetic aperture radar (SAR), the resolution of the single-hole fracture imaging system comes from aperture length and bandwidth. The vertical synthetic aperture can generate a beam steerable in elevation plane, and thus an elevation resolution can be obtained. Although the radar is focusing in the near-field with relatively small f/D, resolutions can be estimated by SAR formulas. The angular resolution is determined by $r_\theta = \lambda_{rock} / 2D$ [85]. Range resolution is determined by the transmitter bandwidth BW as $r_R = c_{rock} / (2 \times BW)$, where c_{rock} is the speed of wave in the medium.

If the synthetic array consists of 40 elements with separation of 25 m with relative permittivity of 4, and the horizontal distance between the target and the RX antenna is R = 1250 m, the bandwidth is 0.9 MHz, the range and elevation resolutions are calculated to be 83 m and 54 m, respectively. These numbers are slightly different than the simulated results (in the following paragraph) due to far-field focusing approximation.

Resolutions of proposed system as a function of horizontal range are tested by point target simulations. The target is fixed at origin and the borehole is moved from x = -200 m to x = -2500 m. Vertical coordinates of the antenna array keep the same, which is z = 200~1200 m. Two Dolph-Chebyshev windows with different sidelobe suppressions (80dB and 150dB) are used in simulations in order to handle the near-end and the far-end of the detectable range. As demonstrated in Figure 2.15, the range resolution is almost independent of distance. In fact, it mainly affected by the available bandwidth as discussed previously. The elevation resolution grows linearly when the distance increases. However, when the target is very close to the radar, the resolutions also go larger, due to small incident angles and time-gating leakages.

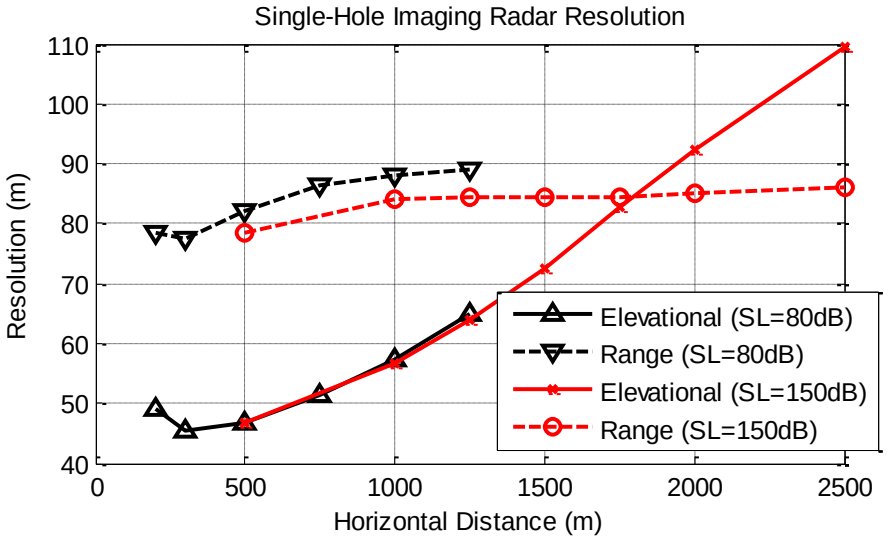

Figure 2.15. Range and elevation resolutions of single-hole imaging radar as a function of horizontal range from the point target. Two window functions with different sidelobe levels are used in time-gating.

2.4.5 Imaging Result Demonstration

The imaging result demonstration of the single-hole system also starts with a point target at the origin. The point target RCS is obtained by simulating a metallic sphere in HFSS at each frequency sample and many backscattering directions in the surrounding rock medium. The frequency span matches the antenna frequency tunable range, namely 1.6 MHz to 2.8 MHz, and

a frequency step is 0.01 MHz. The antenna wellbore (which contains both the TX and RX antennas) is located at x = -1250 m and z = 200~1200 m. In time-gating process, the window function is selected to have a sidelobe of -150dB and the gate center is at the origin position in the time series. Figure 2.16 (a) shows the received signal before time-gating and after that in time domain. The gated signal dominants by the scattered signal component while the direct-link signal occurring at t = 1 μs is nicely suppressed. The mapping result is shown in Figure 2.16, which clearly shows a spot at the origin with its size matching the theoretical resolution.

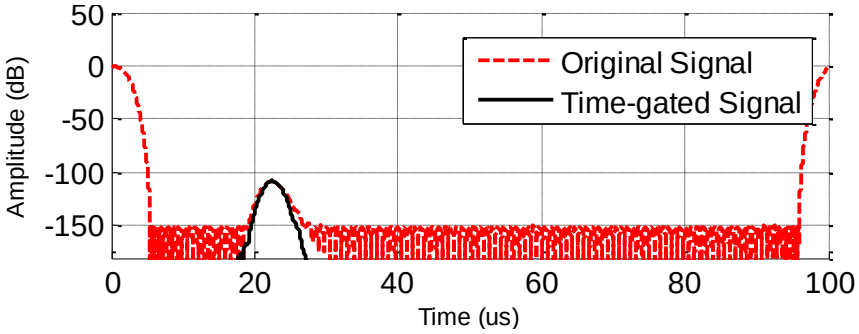

(a) Time domain gating.

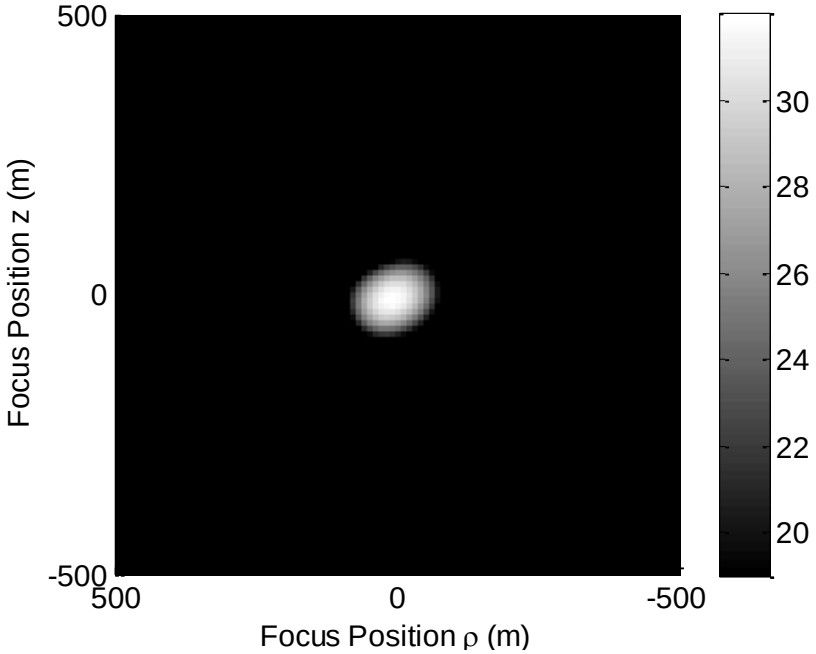

(b) mapping result that shows the point spread function.

Figure 2.16. Single-hole point target mapping demonstration.

The cylindrical model with effective permittivity introduced previously is also tested with single-hole system. However, since in single-hole system, it is the back-scattering that provide us the information of the target instead of the bistatic scattering in the cross-hole system, the cylindrical model does not produce a strong backscatter. The smooth flat surface produces little back-scattering and thus the surface of the target becomes undetectable. Only the edges of two ends of the cylinder show up in the image as shown in Figure 2.17, The lower left corner produces the most pronounced backscatter due to double-bounce effect and its position is shifted due to longer delay of the signal propagating through the higher dielectric cylinder .

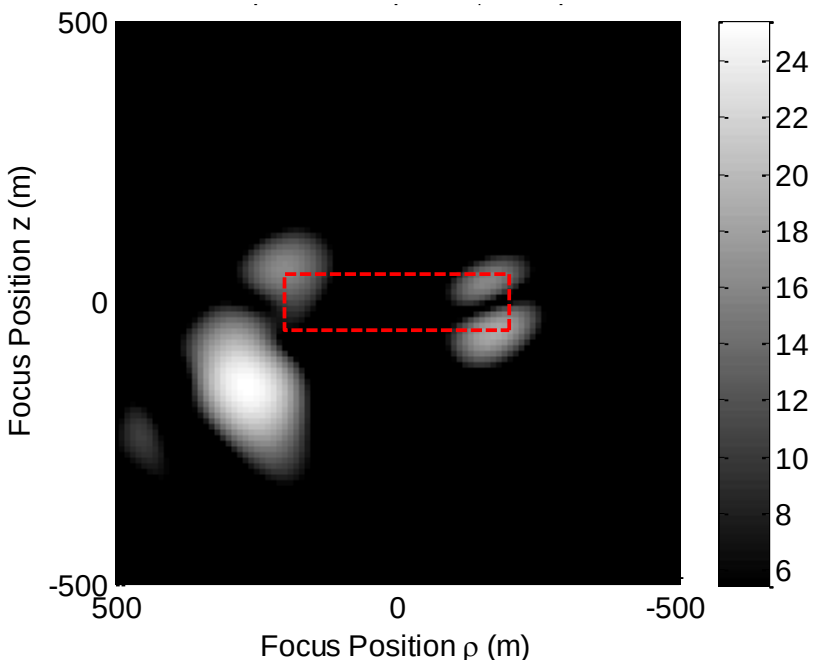

Figure 2.17. Single-hole cylindrical model mapping result: The dash line depicts the cylinder position and shape.

Finally, the mapping result of the realistic fracture model shown in Figure 2.7 (a) is demonstrated in Figure 2.18. This model consists of many thin layers that are orientated close to vertical or horizontal directions and can produce much higher backscatter at the discontinuities caused by the hydraulic fracture pattern in shale rock [96]. The target image is brighter on upper right side, because of the illumination direction and the shadowing effects. Though the detailed

feature of each individual fracture is not clear, the overall shape of the fractured region is well depicted.

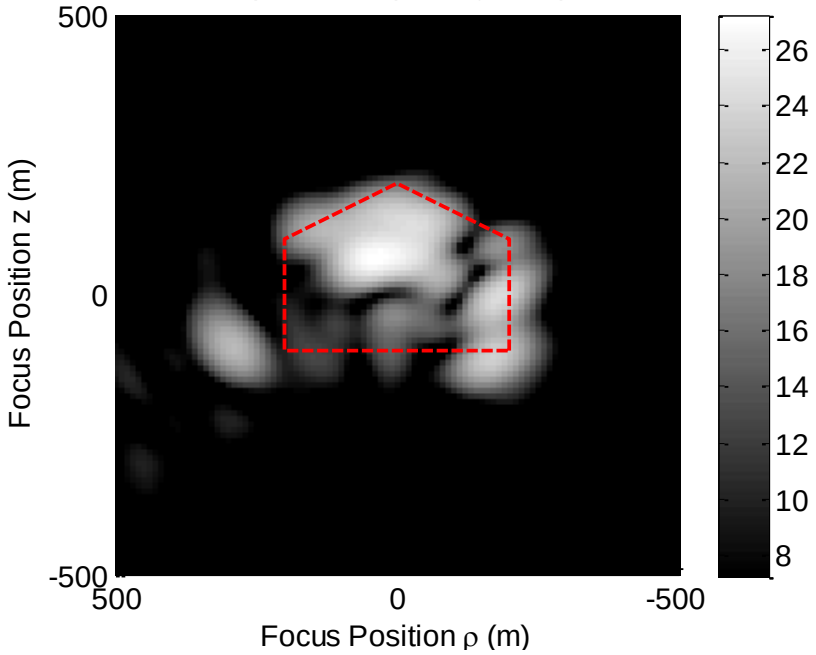

Figure 2.18. Single-hole fracture model mapping result. The dash line depicts the fracture region and the approximate outline.

2.5 Conclusion

This paper presents a subsurface imaging radar at MF band for detection of the extent of fracture region in hydraulic fracking for oil and gas extraction. Two approaches are proposed and demonstrated: 1) a bistatic synthetic aperture radar (SAR) arrangement that places TX and RX antennas in different wellbores and uses CW signal, and 2) an almost monostatic SAR with a tunable narrowband TX and RX antennas in the same borehole. With focusing the synthetic TX and RX arrays simultaneously at different depth and lateral directions along the horizontal wellbore around which fracking occurs, a 2-D map of the underground fractured region is generated. Such 2-D maps indicate the vertical and lateral extent of the fractured region due to the fact that the dielectric constant and conductivity of this region is significantly different than the surrounding medium. An adaptive null steering while focusing beamforming approach is

developed to suppress the direct signal from the TX to RX elements. The second imaging setup is called single-hole system for which the TX and RX arrays are placed in a single well with a separation to achieve a desired isolation. A series of stepped frequency continuous wave measurements are performed and a time-gating process is applied to further reduce the direct signal leakage between TX and RX in time-domain. Taking advantage of frequency bandwidth and the synthetic aperture beam forming, good range and cross-range resolutions are achieved. Both setups are tested with a point target, a cylindrical target, and a realistic fracture model. It is shown that the extent of fractured region (outline of the region) can be clearly mapped from a standoff position within the vertical wellbores.

CHAPTER III

Super-Miniaturized MF Antenna for Borehole Radar Application

3.1 Introduction

Borehole antennas have been widely used for underground radio sounding systems used for geological exploration purposes [9]-[11]. In the thesis, a highly-miniaturized borehole antenna operating at 2MHz is needed as a part of the proposed hydraulic fracture imaging system at MF band.

This chapter presents a ferrite-loaded non-uniform helical folded-dipole antenna for borehole application. The ferrite core is composed of a bundle of small ferrite cylinders designed in such a way to minimize the loss. The dimensions of the antenna are miniaturized to 98 mm × 98 mm × 4100mm or $\lambda_0/1500 \times \lambda_0/1500 \times \lambda_0/35$, while the radiation efficiency is kept relatively high. High power transmitters cannot be sent down with the antenna in the borehole, thus the antenna must be fed by a transmission line connected to a source on the surface. As will be shown, passing a transmission line, such as coaxial line, through the center of the helical antenna significantly reduces the antenna impedance match and its radiation efficiency. Two layers of disjointed cluster of ferrite core is considered to mask the effect of a conducting cylinder placed inside the antenna to mitigate the adverse effects of the transmission line at the center of the antenna.. Moreover, we also proposes a feeding network that not only matches the antenna input impedance to the standard 50 Ω transmission line, but also enables frequency tunability within a

relative bandwidth of 40%. This tunable bandwidth can be utilized in radar system to synthesis the frequency response of a target through the narrow band antenna.

3.2 Helical Antenna Design

For borehole applications, the antenna diameter has to be less than 0.1 m and for handling its length should be less than 4m. The proposed antenna structure is shown in Figure 3.1. An open-end wire is wound around magnetic cores, forming a normal mode helical antenna. When excited at the center, a standing wave along the wire can be generated and the current is distributed along the helix in a sinusoidal manner similar to dipole antennas. Thus the antenna has a similar radiation pattern as that of a dipole antenna. The total arc length of the helical wire is approximately equal to half of the wavelength in the surrounding medium. It should be noted that as the wire is wound around the core there is a mutual magnetic coupling that can further reduce the antenna size, but similar to short dipoles the radiation resistance drops. The more turns per unit length, the higher is the miniaturization factor but the lower is the radiation efficiency.

In order to maximum the radiation efficiency, a non-uniform pitch distance for the proposed antenna is proposed whose geometry is shown in Figure 3.1. In the helix, the horizontal component (φ-component) of the current can be viewed as forming small circular loops with extremely small radiated far-field. The axial component (z-component) of the helix is responsible for the major component of the far field radiation. The axial component is proportional to the pitch of the helix. Keeping the total antenna height constant, by increasing the pitch where the current is high and decreasing it in locations where the current is low, one can optimize the helical antenna's radiation efficiency. From the knowledge of half-wavelength

dipole antenna, the current distribution reaches its maximum in the middle and decreases gradually to zero at the two ends. Hence, in the proposed antenna, the pitch is chosen larger in the middle and gradually reduced towards the two ends. For simplification, we only changed the pitch along the antenna length in a linear fashion.

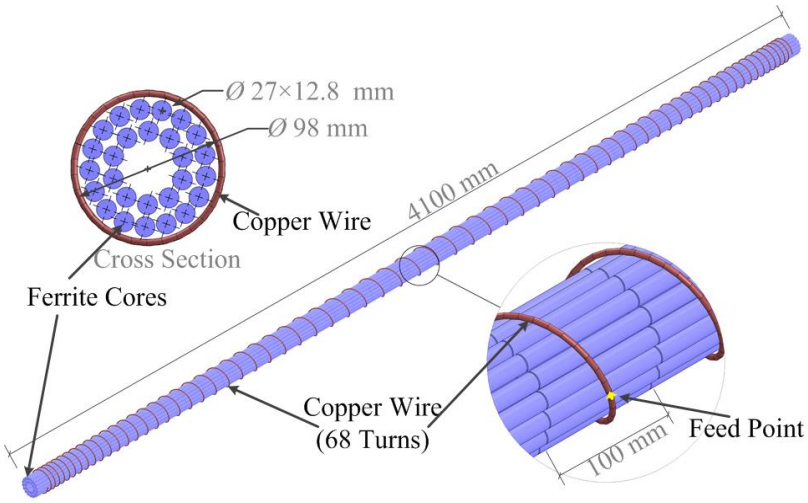

Figure 3.1. Illustration of the non-unifrom helical antenna with two-layer disjointed clustered ferrite cores.

The spiral current generates strong axial magnetic field inside the helical antenna, which inspires the application of high permeability material to further miniaturize the antenna. The Nickel Zinc (NiZn) "61 material" from CWS ByteMark is a high frequency ferrite developed for a range of magnetic devices up to 25 MHz with a relatively high permeability of 125 [97]. A cylindrical ferrite core can be placed inside the helix to reduce the size, as Figure 3.2 (a) shows, but transverse eddy currents are excited due to the ferrite finite conductivity. The induced current in the ferrite will not only dissipates energy but also cancels part of the radiated field. Both effects will negatively impact the radiation efficiency. To reduce the eddy current in the core, we can cut several slots alone the ferrite axis to stop the flow of eddy currents, as Figure 3.2 (b) shows. Alternatively, we can use several insulated thin ferrite cylinders to create a low loss high permeability "composite core", shown in Figure 3.2 (c). If the thin cylinders are not connected,

the transverse current can be significantly reduced. Since the magnetic field inside the helix is predominantly axial, the ferrite discontinuity in transverse plane will not affect the effective permeability or the miniaturization factor very much. The effective permeability of the proposed disjointed ferrite core is anisotropic with the axial value proportional to the ferrite volume fraction. Let's consider the solid core situation, in Figure 3.2 (a). Because of the high permeability, the electromagnetic field will mainly distribute near the surface of the core. Thus, if we remove part of ferrite near the center, the fields cannot "see" this change. For the composite core in Figure 3.2 (c), we can still remove the inner ferrite and maintain a high effective permeability. In reality, one layer of ferrite cores will be thick enough to achieve 80% of the miniaturization factor of the solid core. But in situation where a conducting cylinder in the center is needed (the feed cable for the antenna), two layers of ferrite cores will be necessary to preserve higher efficiency as will be discussed later.

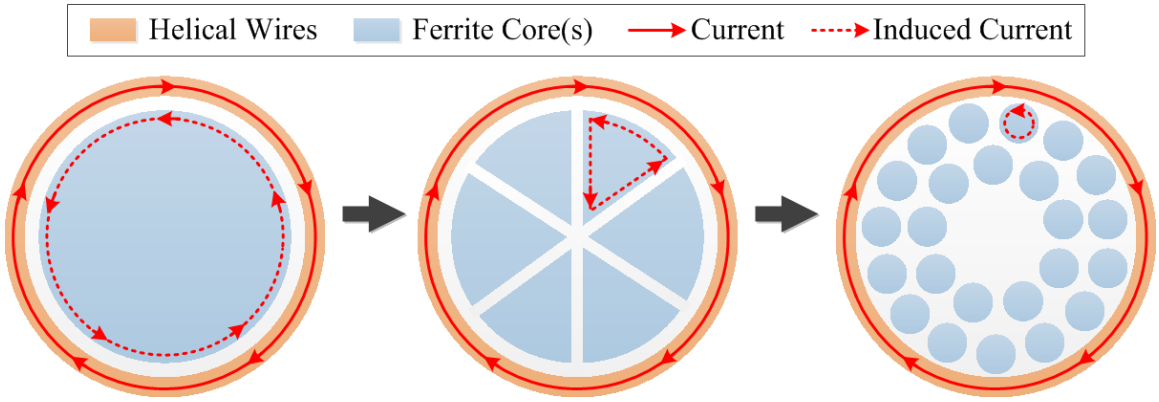

Figure 3.2. Optimization of composite ferrite core in the helical antenna from the cross section view.

Ideally, we can use long ferrite cylinders throughout the entire length of the antenna to form the composite core without disturbing the continuity in axial direction. However, ferrite rods are usually commercially available with a typical length less than 15 cm. Besides, out of the consideration for their thermal expansion and the mechanical strength, to form a long (>4 m)

composite ferrite core, many short rods have to be jointed. Unlike the transverse discontinuity, the gap between each segment may have marked impact. Thus, we modeled the ferrite cores by many rods, 100 mm in length and 12.8 mm in diameter, with 1 mm gap between the rods, as shown in the detail view in Figure 3.1.

The simulation results are shown in Figure 3.3. As expected, both the radiation pattern and the input impedance plots are similar to that of a small dipole antenna. At the resonance of 2.1 MHz, the radiation impedance is merely 1.3 Ω, which corresponds to the radiation impedance of a small dipole [98]. The bandwidth of this antenna is simulated to be 1.4 kHz.

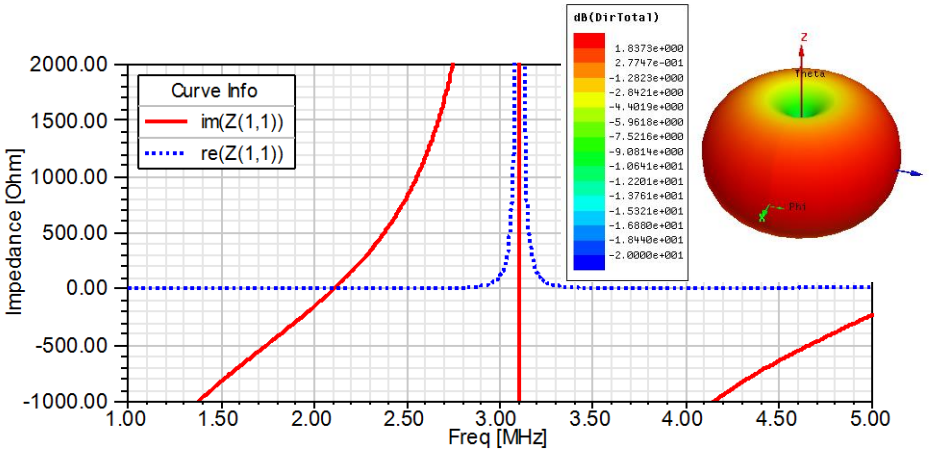

Figure 3.3. The real part and imaginary parts of the input impedance and the radiation pattern of the proposed helical antenna.

3.3 Effect of a Central Conducting Cylinder

Generally, dipole antennas are very sensitive to the placement of a nearby conductor. However, for the borehole application, the feeding cable must pass through the center to reach the middle of the helix. Moreover, in the case that multiple antennas are needed in the same borehole (vertical array), the cables have to go through the entire length of the helix to connect the other antennas underneath. We examined this case by placing a long conductive cylinder along the axial direction at the center of the helix as Figure 3.4 shows. In the absence of the ferrite core, the conductor will significantly change the performance (e.g. efficiency) of the

helical antenna due to the close proximity of the conductor ($<\lambda_0/1000$). The induced current on the conductor will cancel out the radiated field from the antenna itself. The presence of the ferrite cores between the helix and the inner conductor can reduce that negative impact. The simulation also indicates that the two-layer ferrite cores can achieve much higher efficiency than single-layer as shown in Table 3.1 (Ant II and III). An efficiency value of the order of 10% can be achieved for this antenna.

Another effect of the central conductor is the frequency shift. Table 3.1 indicates that from Ant I (without a conductor at the center) to Ant III (with a conductor at the center), 40% frequency shift has been observed. This potentially provides another method to miniaturize the antenna but the tradeoff is the efficiency drop. However, if we decrease the number of turns to increase the resonant frequency to back 2 MHz, the antenna efficiency, bandwidth, and input impedance improve, which to some extent can compensate the negative effects of the presence of a central conductor.

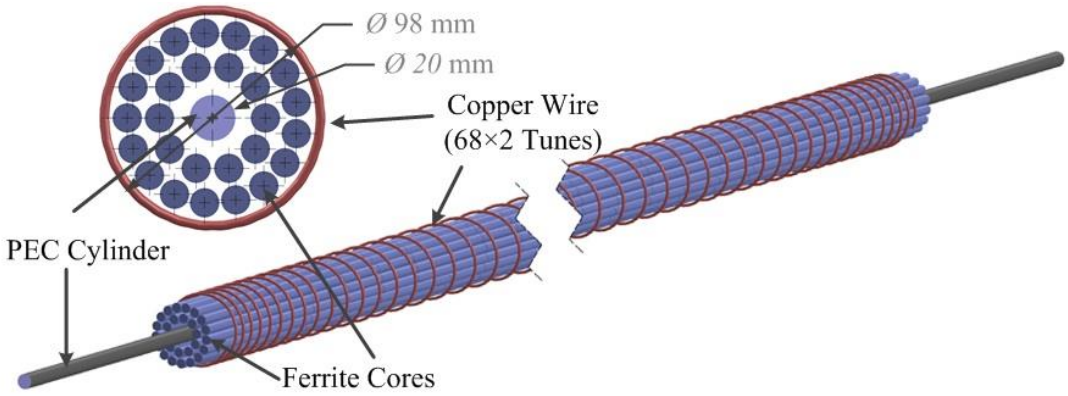

Figure 3.4. Illustration of the proposed helical antenna with two-layer disjointed ferrite cores in the presence of the central conductor.

3.4 Folded Helical Antenna Design

One problem of the proposed antenna is that the value of its input impedance is too low to be matched without additional penalty in power efficiency. This also is mainly due to the fact that the loss resistance of the matching network becomes comparable to or larger than the radiation impedance. Inspired by folded dipole antenna whose radiation impedance is four times that of the normal dipole antenna, we consider a folded helical antenna as shown in Figure 3.5. The simulation result is compared to the unfolded designs in Table 3.1. As expected, the input impedance is increased nearly by a factor of four. The folded version with a central conductor has also been studied (Ant V in Table 3.1).

Table 3.1. Simulation Results of Proposed Antennas.

	Ant I	Ant II	Ant III	Ant IV	Ant V
Folded-Dipole Design				●	●
Number of Layers in Composite Core	2	1	2	2	2
With Conductor at Center		●	●		●
Illustration	Figure 3.1		Figure 3.4	Figure 3.5	
Frequency f_0 /MHz	2.1	1.5	1.22	2.06	1.14
Antenna Length L1	$\lambda_0/36$	$\lambda_0/50$	$\lambda_0/61$	$\lambda_0/36$	$\lambda_0/66$
Bandwidth BW /KHz	1.4	1.1	1.1	1.5	0.8
Radiation Efficiency	29%	4%	10%	50%	10%
Impedance R_0 / Ω	1.3	0.5	0.7	5.0	2.3

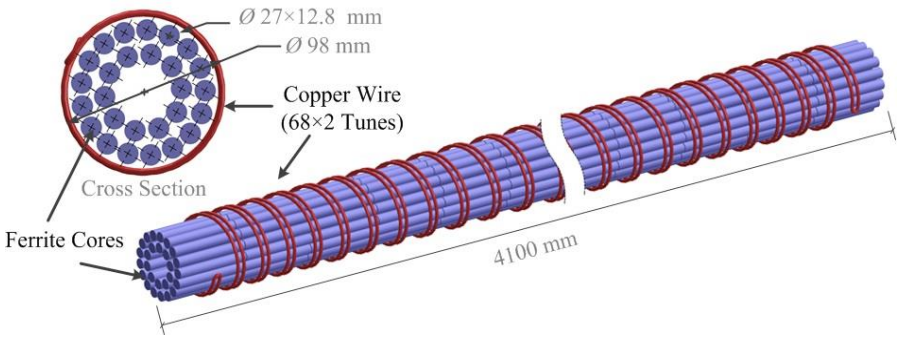

Figure 3.5. Illustration of the proposed folded-dipole helical antenna with two-layer disjointed ferrite cores.

3.5 Feeding Network Design

As demonstrated above, the proposed ferrite loaded folded helical antenna input impedance is much lower than a standard coaxial cable's impedance Another drawback is the antenna bandwidth which is very low due to the high quality factor nature of resonant small antennas. For many radar applications fine range resolution which is inversely proportional to the waveform bandwidth is needed. This requires antennas with relatively wide bandwidth. In order to match the antenna input impedance to the standard impedance of 50 Ω, it is necessary to design a matching network for the proposed antenna. As observed earlier, the proposed antenna has a very narrow bandwidth of about 0.1% at its resonance, which is acceptable only for a continuous wave (CW) system and thus limits its applications for most practical cases. For instance, for an underground subsurface imaging system, the frequency bandwidth could be used to achieve a range resolution or to perform the time gating process. To counteract the inherent narrow bandwidth of the antenna, the feeding network can be designed to enable frequency tunability. The antenna frequency agility can be utilized to obtain a frequency bandwidth, which can be used to synthesis the frequency response of a target through the narrow band antenna.

At MF frequencies, lumped circuit elements are suitable for matching circuit. The proposed feeding network consisting of a toroid transformer to convert low antenna input impedance to 50 Ω standard impedance and a capacitor to compensate the inductance introduced by the transformer is shown in Figure 3.6.

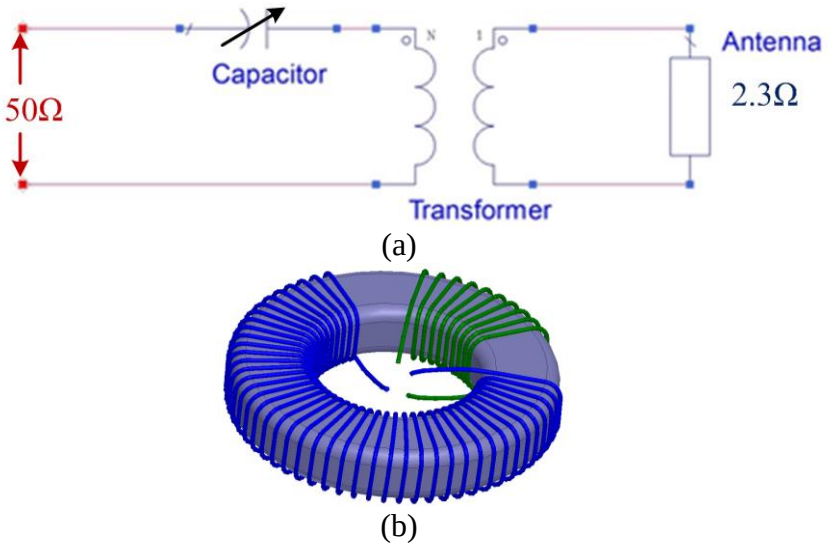

Figure 3.6. (a) Feeding network configuration and (b) the geometry of the toroid transformer

One advantage of using transformer and series capacitor in the feeding network is the frequency tunability. By tuning the series capacitor, the resonant frequencies can be shifted up and down over a wide range as shown in Figure 3.7(a). The relationship between the resonant frequencies and the series capacitor values are shown in Figure 3.7(b), noting that each capacitor value corresponds to two resonances. In order to cover most of the desired frequency range, a capacitor with a tunable range of 10 pF to 40 pF is enough. However, at frequencies near 2.05 MHz where the original antenna resonance is, a much larger or smaller capacitor value is needed. Thus, the tunable range is approximately from 1.5 MHz to 3 MHz but excluding 2 MHz to 2.1 MHz.

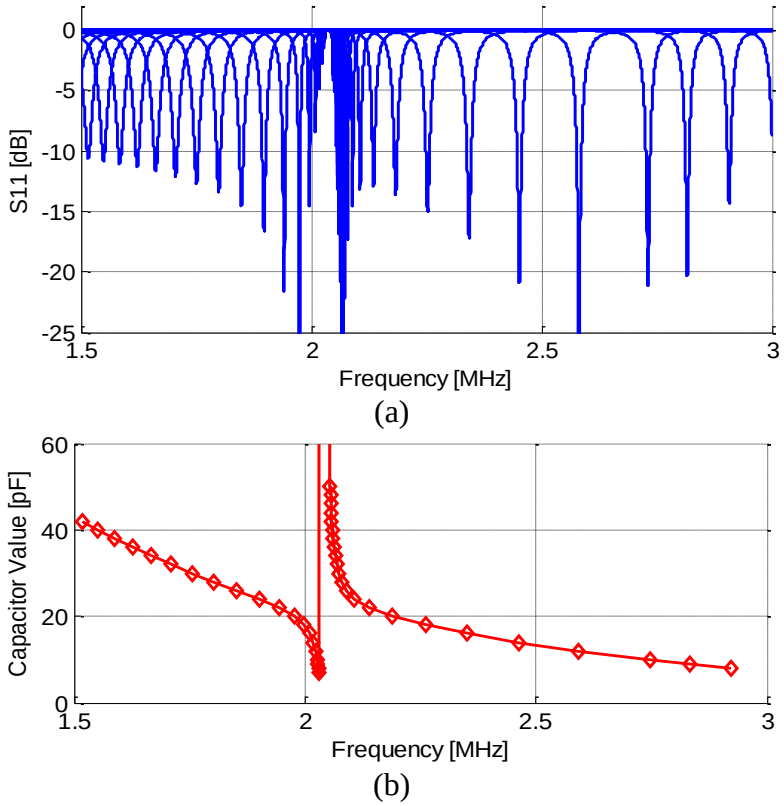

Figure 3.7. (a) S11-parameter curves with various series capacitor values. (b) Relationship between the resonant frequencies and the corresponding capacitor values.

The efficiency values of the feeding network and the antenna are simulated in Ansoft HFSS and Agilent ADS. If a fixed capacitor is used in the feeding network, the frequency response of the delivered power to the antenna is shown as the thin blue curve in Figure 3.8. The maximum delivered power occurs at the resonant frequency of the each blue curve. At most frequencies in the tunable range, by tuning the capacitor value according to Figure 3.7(b), the feeding network can efficiently deliver power to the antenna with a small reflection loss (<10 dB) and a reasonable insertion loss (~50%), shown as the thick green curve in Figure 3.8. The transformer is characterized by a full-wave simulation. The quality factor (Q) of the capacitor in the simulation is set to be 100.

The antenna's efficiency is shown as the black dash curve in Figure 3.8. The efficiency decays when the frequency is shifted away from the antenna resonant frequency. This is caused

by the dielectric loss from the increasing reactive field applied to a lossy ferrite core when shifting operation frequency away from antenna's resonance. By combining the antenna's efficiency curve and the feeding network's, the overall efficiency is shown as the thick red curve in Figure 3.8. The efficiency reaches -9 dB near the antenna's resonance at 2.1 MHz. If we use -25 dB overall efficiency as a threshold, the tunable range can extend to more than 1.2 MHz (from 1.75 MHz to 3 MHz). Since the efficiencies within the tunable range vary by 16 dB, it requires a gain compensation technique to achieve a flat frequency response which is not difficult to be realized in the post processing.

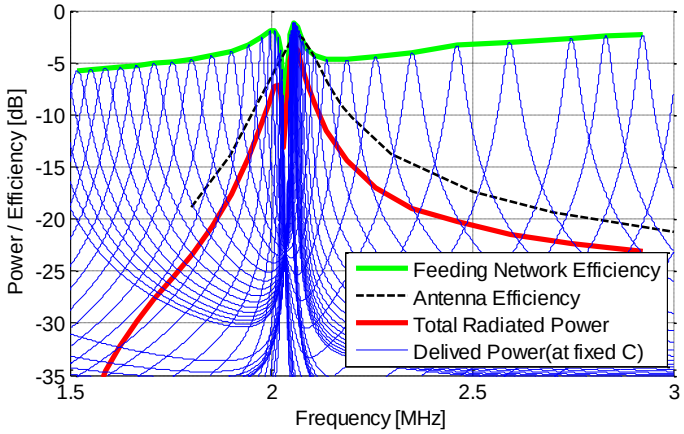

Figure 3.8. Efficiencies of the feeding network and the antenna within its tunable frequency range.

3.6 Conclusion

In this chapter, a super-miniaturized borehole antenna working at MF band with the dimensions of $\lambda_0/1500 \times \lambda_0/1500 \times \lambda_0/35$ with reasonable radiation efficiency is presented. The proposed antenna is based on a folded helical dipole which is loaded with disjointed composite ferrite core. The antenna is envisioned for borehole imaging radar application. To preserve efficiency, composite ferrite core and non-uniform winding pattern are employed. According to the simulations, the radiation efficiency can reach as high as 50% at 2.06 MHz. In the presence of a conducting cylinder in center, the proposed antenna can still maintain a good radiation

efficiency of 10% provided that two layers of composite ferrite core cover the conducting cylinder. A matching network composed of a transformer and an adjustable capacitor is also presented. By tuning the series capacitance of the resonant matching network, it is shown that the antenna can work over a wide range of frequencies. Such antenna can be used with a stepped frequency radar which allows range compression through a post frequency synthesis process.

CHAPTER IV

Scattering Phenomenology of Arctic Lake Ice

Besides the application of radar sensing in hydraulic fracture detection, remote sensing in Arctic lake region is also an important topic. By exploring the scattering mechanism of the lake ice, the imaging results of radar remote sensing can be quantitatively analyzed and from which many useful physical information can be extracted. Thus, scattering phenomenology becomes one of the most important research areas in applied electromagnetics. In this Chapter, a numerical method for analyzing Arctic lake ice scattering is studied. This method can be further used to study the scattering mechanism of other random medium such as hydraulic fractured rock region.

4.1 Introduction

Lakes and ponds are widely distributed characteristic features of the Arctic north. With growing concern for ecosystem changes due to global warming, lakes and lake ice change take on greater research interest [99]. Since mid-1970s, a number of satellite SAR missions have provided a wealth of archival data that can be used to explore lake evolution over more than several decades.

Figure 4.1 shows two ERS-2 acquisitions of frozen lakes on the Barrow Peninsula of Alaska, acquired in January and February of 2009 [73]. The red ovals serve to highlight lakes that transitioned from bright to dark. This behavior is observed for many of the shallower lakes

in the region, which exhibit reduction in backscatter as the lake ice thickens through the winter and grounds to the underlying sediment. Other lakes, seen as dark in the figure, were even shallower and had grounded earlier in the season. This effect has been noted by numerous researchers [100]-[104].

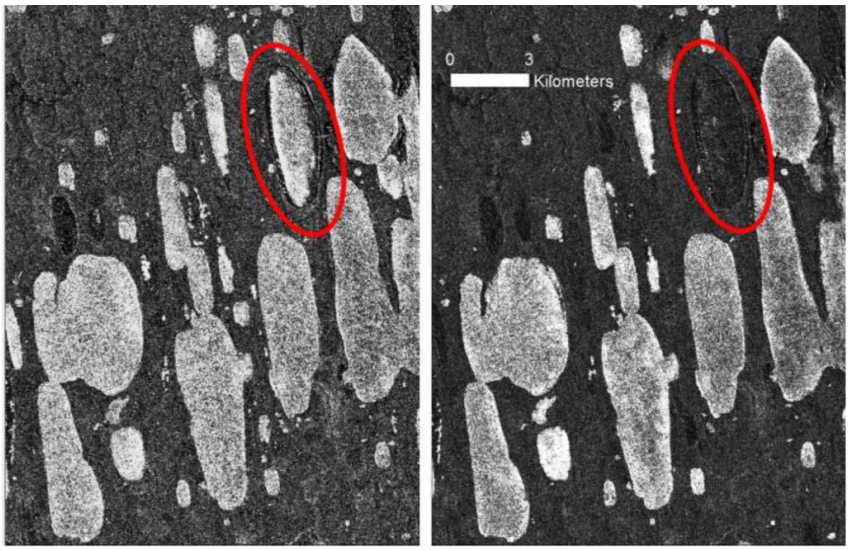

Figure 4.1. ERS C-band images acquired on (left) January 10 and (right) February 14 of 2009 show changes in radiometry as ice grounds to the bottom of the lake. [73]

A distinctive aspect of many high latitude lakes is the presence of vertically-oriented, columnar air bubbles in the ice. Many researchers [104]-[106] have attributed the characteristically high backscatter from floating ice to double bounce from these bubbles and the ice/water interface. Other authors [99][107] have suggested the mechanism is backscatter from the ice/water interface. Fortunately, the introduction of polarimetry in satellites such as ALOS-1 and-2 (L-band), RADARSAT-2 (C-band), and TerraSAR-X (X-band) can provide useful insight into the actual scattering mechanism. In a recent paper by the authors, polarimetric satellite data, ground-based radar, and numerical modeling were used to investigate the dominant cause of lake ice backscatter. All empirical tests pointed strongly to the dominant scattering being caused by

single bounce reflection from the rough bottom surface of the ice/water interface. In addition, rigorous coherent numerical modeling of C-band radar was unable to show any significant impact of the bubbles upon the backscatter, except for what one would expect from their contribution to modulating the effective refractive index of the ice.

The goal of this paper is to explain in greater detail the numerical modeling used to investigate microwave scattering from floating ice and to reinforce the single bounce explanation for its strong backscatter. In order to study as many physical mechanisms as possible and to minimize the approximations and the assumptions made in the model, a full-wave simulation model is preferred. When running a full-wave simulation model for random surfaces, the Monte Carlo method is often employed to average the fluctuation due to the randomness in individual simulations [108]-[114]. The infinite random region can be studied by a finite simulation by applying either tapered incident field [115][116] or periodic boundary condition [117]. In this Chapter, a numerical model based on full-wave finite element method (FEM) solver is presented in Section 4.2. The model handles most of the scattering mechanisms in the lake ice, including the rough ice/water surface, the inclusion of the columnar gas bubbles and all the interaction between them. The periodic boundary condition is applied and is carefully analyzed to give the corresponding far-field scattering coefficient of the random surface from the finite area simulation. Section 4.3 presents some numerical simulation results, including the bistatic scattering coefficient, the effects of the clear ice layer thickness, a rough ice/water interface and the presence of columnar bubbles. Section 4.4 concludes that the rough ice/water interface usually dominants the C-band backscattering on the lake ice while the double-bounce reflection is negligible for the most scenarios of Arctic lake ice.

4.2 Numerical Model

In order to study the lake ice microwave scattering mechanism, we use a model consisting of plane wave illumination of a heterogeneous medium with a rough ice/water interface. The formulation is based on finite element method with periodic boundary condition (PBC) in two lateral directions (*x*- and *y*- directions). The model setup is shown in Figure 4.2, where the bottom surface in the model represents the interface between the ice and lake water. Due to the high dielectric constant contrast of water at microwave frequencies, the ice/water interface can be modeled by an impedance boundary condition where the surface impedance is determined by

$$Z_{water} = \eta_0 / \sqrt{\varepsilon_{water}} = (43 + 5j)\Omega . \quad (4.1)$$

This is a good approximation as the angle of refraction is very small ($\theta_t < 10°$) and in this case the ratio of electric field to magnetic field at the interface is almost constant and independent of angle of incidence ($\frac{E}{H} = Z_{water}$)[118][119].

To take the roughness of the ice/water interface into consideration, this interface is created with a 2-D random surface generator having a desired RMS height and correlation length. Backscattering calculation using Monte-Carlo simulations can be carried out by a finite-size box that is many correlation lengths on each side to fully represent the statistical property of the rough surface. The ice/air interface may also be rough, but this roughness contributes less to backscattering since the dielectric mismatch between air and ice is significantly lower than that between ice and water. Also, the wavelength in ice is 44% shorter than the freespace wavelength, which makes the effective roughness of the ice/water interface to appear larger in terms of the medium wavelength. Thus ice/water interface roughness dominants the single-bounce backscattering and the ice/air interface roughness is not included in the simulation model.

In thick lake ice scenery, columnar bubbles may exist in the lower half of the ice layer [101][120]. These bubbles, perpendicular to the ice/water interface, can potentially produce a double-bounce reflection and contributes to the backscattering. Thus it is necessary to include some randomly located columnar air bubbles in the simulation model in order to investigate their contribution to the backscattering. The top two layers in the model are air and a perfectly matching layer (PML) which absorbs the outward waves for modeling purposes.

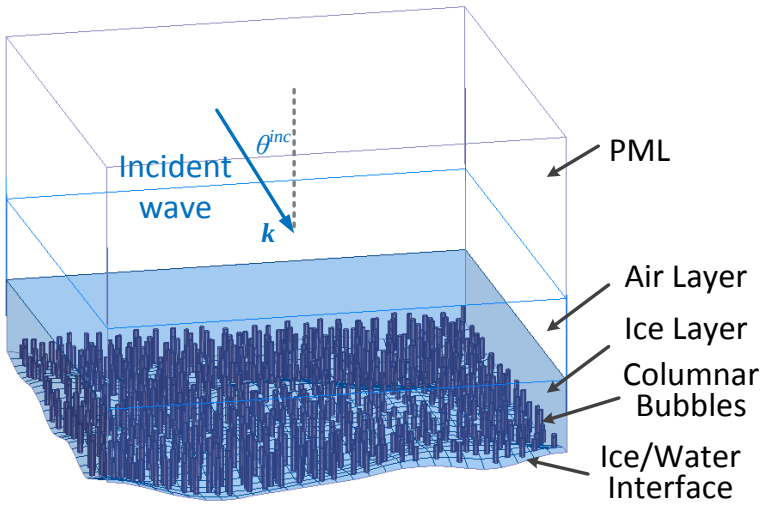

Figure 4.2. The simulation model setup for lake ice scattering study

Many rough surface simulation models use absorbing boundary condition (ABC) as the side walls of simulation box [115][121]. This setup usually requires large box size to minimize the truncation effect. However, for a complex multi-layer rough surface structure with large thickness, the computational complexity may not allow one to create a simulation domain to extend over larger than ten wavelengths. An alternative approach is to take the truncation effect into consideration using a periodic boundary condition (PBC). However, in this case, it is important to ensure the surface boundaries match at the beginning and end of PBC to avoid surface discontinuity. Such surface discontinuity can be a major source of diffraction and thus can perturb the statistics of the backscattered fields. Here, it is ensured that the periodic surface

function and its first derivative are continuous at the boundaries. According to Floquet's theorem, the bistatic scattering field for a given incident direction occurs along certain discrete angles. Since the backscattered response is of interest, the period of the 2-D periodic surface is chosen so that one of the Bragg scattering directions coincides with the backscatter direction. The near field calculated in the FEM domain is then transformed into far field radiation at these angular points, to calculate the radar cross section (RCS) or scattering coefficient.

In a 2D periodic structure, the scattered field can be written as the following form where the incident angle determines the phase propagation term between different unit cells:

$$\mathbf{E}\left(x + nL_x, y + mL_y, z\right) = \mathbf{E}(x, y, z)e^{jk_0\left(nL_x \sin\theta_i \cos\phi_i + mL_y \sin\theta_i \cos\phi_i\right)}. \tag{4.2}$$

One can express the field in terms of its inverse Fourier Transform given by:

$$\mathbf{E}(x, y, z) = \frac{1}{4\pi^2}\int_{-\infty}^{+\infty}\int_{-\infty}^{+\infty}\tilde{\mathbf{E}}\left(k_x, k_y, z\right)e^{-jk_x x - jk_y y}dk_x dk_y \ . \tag{4.3}$$

According to the wave equation, the Fourier transform must be of the form of:

$$\tilde{\mathbf{E}}\left(k_x, k_y, z\right) = \mathbf{A}\left(k_x, k_y\right)e^{-jk_z z}. \tag{4.4}$$

from which the scattered field can be computed:

$$\mathbf{E}(x, y, z) = \frac{1}{4\pi^2}\int_{-\infty}^{+\infty}\int_{-\infty}^{+\infty}\mathbf{A}\left(k_x, k_y\right)e^{-jk_z z}e^{-jk_x x - jk_y y}dk_x dk_y \ . \tag{4.5}$$

Assuming $\mathbf{A}(k_x,k_y)$ is known and using the stationary phase approximation [122], the far field radiation can be computed from:

$$\mathbf{E}(\mathbf{r}) = \frac{jk_0 \cos\theta_s e^{-jk_0 r}}{2\pi r}\mathbf{A}\left(k_0 \sin\theta_s \cos\phi_s, k_0 \sin\theta_s \sin\phi_s\right), \tag{4.6}$$

whose components are explicitly given by:

$$E_\theta(\mathbf{r}) = jk_0\frac{e^{-jk_0 r}}{2\pi r}\left(A_x \cos\phi_s + A_y \sin\phi_s\right), \tag{4.7}$$

$$E_{\phi}(\mathbf{r}) = jk_0 \frac{e^{-jk_0 r}}{2\pi r} \cos\theta_s \left(A_y \cos\phi_s - A_x \sin\phi_s\right). \tag{4.8}$$

By taking the Fourier Transform of Eq. (4.5), $\mathbf{A}(k_x,k_y)$ can be expressed as an integral of near field at $z = z_0$ plane,

$$\mathbf{A}(k_x, k_y) == e^{jk_z z_0} \int_{-\infty}^{+\infty}\int_{-\infty}^{+\infty} \mathbf{E}(x, y, z_0) e^{jk_x x + jk_y y} dxdy \ . \tag{4.9}$$

In a source-free region, the electric field is solenoidal, so we have:

$$\mathbf{A} \cdot \mathbf{k} = A_x k_x + A_y k_y + A_z k_z = 0 \ , \tag{4.10}$$

$$k_x^2 + k_y^2 + k_z^2 = k_0^2 \ . \tag{4.11}$$

That relationship states that only two components of $\mathbf{A}(k_x,k_y)$ are independent, so only tangential components are calculated,

$$\mathbf{A}_{\mathbf{t}}(k_x, k_y) = e^{jk_z z_0} \int_{-\infty}^{+\infty}\int_{-\infty}^{+\infty} \mathbf{E}_{\mathbf{t}}(x, y, z_0) e^{jk_x x + jk_y y} dxdy \ . \tag{4.12}$$

Recalling the spatial periodicity, the integrals over infinite intervals can be reduced to one unit cell. And the summation limits N and M should approach infinity.

$$\mathbf{A}_{\mathbf{t}}(k_x, k_y) = e^{jk_z z_0} \sum_{n=-N}^{N} e^{jk_0 nL_x \sin\theta_i \cos\phi_i} e^{jk_x nL_x} \sum_{m=-M}^{M} e^{jk_0 mL_y \sin\theta_i \sin\phi_i} e^{jk_y mL_y}$$

$$\cdot \int_0^{L_y}\int_0^{L_x} \mathbf{E}_{\mathbf{t}}(x, y, z_0) e^{jk_x x + jk_y y} dxdy \tag{4.13}$$

The first summation term can be evaluated as following,

$$\sum_{n=-N}^{N} e^{jk_0 nL_x \sin\theta_i \cos\phi_i} e^{jk_x nL_x}$$

$$= 1 + 2\cos\left[\frac{N+1}{2}\left(k_x L_x + k_0 L_x \sin\theta_i \cos\phi_i\right)\right] \cdot \frac{\sin\left[N/2 \cdot \left(k_x L_x + k_0 L_x \sin\theta_i \cos\phi_i\right)\right]}{\sin\left[1/2 \cdot \left(k_x L_x + k_0 L_x \sin\theta_i \cos\phi_i\right)\right]}$$

$$= \begin{cases} 1+2N, & k_x = -k_0 \sin\theta_i \cos\phi_i + \dfrac{2\pi n}{L_x} \\ << N, & k_x \neq -k_0 \sin\theta_i \cos\phi_i + \dfrac{2\pi n}{L_x} \end{cases}, \tag{4.14}$$

where peaks are observed at certain k_x values, where the scattered waves contributed by different unit cells have the same phase and can be added up coherently. A similar statement holds for the other summation at certain k_y values. At these angles, the total field is just the field contributed by a single unit cell (the integral term), multiplied by the number of cells (1+2*N*)(1+2*M*). Thus, one can extract the scattered wave contributed by a single cell at these special k_x and k_y.

$$\mathbf{A}_{t0}(k_x, k_y) = e^{jk_z z_0} \int_0^{L_y} \int_0^{L_x} \mathbf{E}_t(x, y, z_0) e^{jk_x x + jk_y y} dxdy \ , \tag{4.15}$$

where $k_x = -k_0 \sin\theta_i \cos\phi_i + \dfrac{2\pi n}{L_x}$, $k_y = -k_0 \sin\theta_i \sin\phi_i + \dfrac{2\pi m}{L_y}$ and $\sqrt{k_x^2 + k_y^2} < k_0$. These wave vectors correspond to the Bragg angles [123].

Finally, far-field scattering electric field in horizontal and vertical polarizations can be obtained at the Bragg angles and scattering coefficients can be calculated from the following formula:

$$\sigma^0 = \frac{4\pi r^2}{L_x L_y} \left| \frac{E^{scat}}{E^{inc}} \right|^2 \ [dBm^2/m^2]. \tag{4.16}$$

Generally speaking, the larger the box is, the greater is the number of Bragg angles. However, more computational resources will be needed. So there is a tradeoff between the angular resolution of bistatic scattering and the computational cost. For the calculation of backscattering coefficients, for which $k_x = k_0 \sin\theta_i \cos\phi_i$, $k_y = k_0 \sin\theta_i \sin\phi_i$, the box size can be determined from the following formula:

$$L_x = \frac{n\lambda}{2\sin\theta_i \cos\phi_i}, L_y = \frac{m\lambda}{2\sin\theta_i \sin\phi_i}. \quad (4.17)$$

At a user-selected incident angle of 30°, the simulation box lateral size can be as small as one wavelength.

To sum up the section, the PBC is applied on four sidewalls to reduce the computational cost. But the drawback is the creation of discrete visible bistatic scattering angles due to the Bragg's Law for periodic structures. However, by using a proper unit cell size from eq. (4.17), the backscattering can be accurately determined. HFSS FEM solver is used to complete full-wave simulations with this model. The scattered near-field data calculated on the top surface of the air layer is used to calculate the far-field.

4.3 Simulation Results

In this section, the lake ice layer illuminated by a plane wave at C-band (5.4 GHz) and at 30° incident angle is analyzed for the calculation of polarimatric bistatic scattering data. For this scattering problem a full-wave simulation solver based on FEM formulation is used (Ansoft HFSS). To calculate the statistics of the scattered fields and in particular the scattering coefficients, Monte-Carlo method is used. Basically many realizations introduce statistical randomness into the lake ice scattering. A series of setups with different random surfaces are generated and solved, and the coherent average bistatic scattering coefficient can be computed by,

$$\sigma^0_{ave} = \frac{4\pi r^2}{N_{MC} L_x L_y} \frac{\sum \left| E^{scat}(\mathbf{r}) \right|^2}{\left| E^{inc} \right|^2}. \quad (4.18)$$

4.3.1 Bistatic Scattering Coefficient

First, the role of the bottom roughness shown in Figure 4.3(a) is investigated. The Monte-Carlo simulation results for vv- and hh-polarized scattering on the incident plane are reported in Figure 4.3(b) and (c), where the box size are set to be $L_x = L_y = 5\lambda_0$ and $L_x = L_y = 9\lambda_0$, respectively. The ice layer was given a thickness of 50 mm and its bottom is set to be rough (thickness s = 5 mm, correction length l = 50mm). In this case, no columnar bubbles are included, so the results only present the contribution of single-bounce scattering. As shown in Figure 4.3(b)(c), the specular direction (at $k_x = -0.5k_0$) has the strongest scattering/reflection while the backscatter direction (at $k_x = 0.5k_0$) gives the backscattering coefficient. With 10 Monte-Carlo simulations, the variation due to fading can be reduced to an acceptable level. To examine the effect of box size in the estimated backscattering coefficients, two different box sizes are used and shown to provide similar trends. With larger numbers of Monte-Carlo simulations, the variation can be further lowered proportional to $1/\sqrt{N_{MC}}$. But additional computation resources will be required. The backscattering coefficients for two polarizations are read to be -2.57dB (vv-pol) and -3.73dB (hh-pol) in $5\lambda_0$ box simulation, and -3.78dB (vv-pol) and -4.75dB (hh-pol) in $9\lambda_0$ box simulation. The difference of about 1 dB shows that box dimension of $5\lambda_0$ is at the verge of an acceptable criterion for simulation domain.

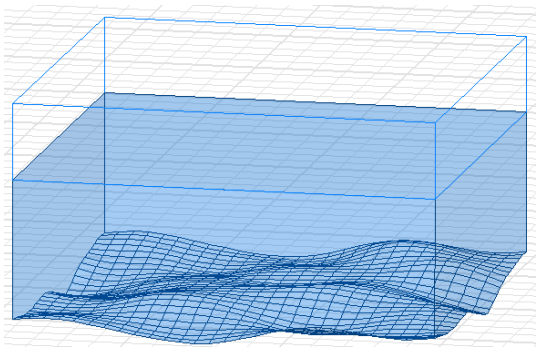

(a) Geometry of the simulation setup.

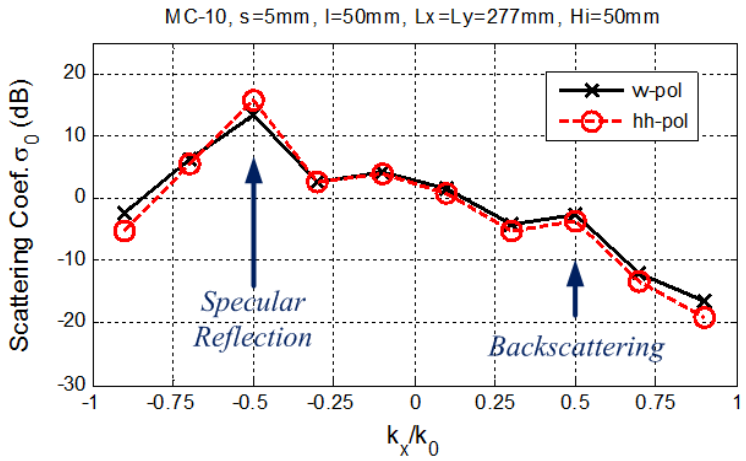

(b) The average of 10 Monte-Carlo simulations with box size of $5\lambda_0$

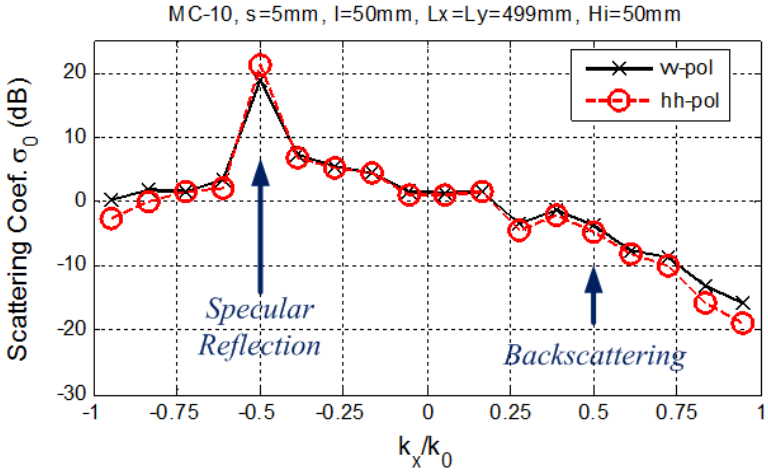

(c) The average of 10 Monte-Carlo simulations with box size of $9\lambda_0$.

Figure 4.3. The bistatic scattering coefficients on vv- and hh-pol of a rough-bottom ice layer of 50 mm thickness.

From Figure 4.3(b) and (c), the specular reflections between two cases are seen to have large differences. This is caused by the fact that the scattering strength (RCS) at the specular

direction is a proportional to the square of the scatterer's area due to the coherent effects. Thus, it should be the reflectivity that is be compared between these two cases, which is defined as:

$$R = \left| \frac{E^{scat}\left(\theta_i, \phi_i + \pi\right)}{E^{inc}} \right|^2 . \tag{4.19}$$

In unit cell simulation, reflectivity can be calculated by comparing the scattering coefficient at specular direction with a flat PEC surface:

$$R = \sigma^0\left(\theta_i, \phi_i + \pi\right) \cdot \frac{\pi}{k_0^2 L_x L_y \cos^2 \theta_i} . \tag{4.20}$$

And here, the calculated specular reflectivities for vv- and hh-pol are respectively -10.85dB and -8.32dB ($5\lambda_0$ box), and -10.14dB and -7.77dB ($9\lambda_0$ box). These can be also compared with the flat-bottom ice layer reflectivity, which can be theoretically calculated using Fresnel equations as -2.40 dB and -1.82 dB for vv- and hh-pol, respectively.

4.3.2 Effect of Ice layer thickness

It is interesting to examine the effect of the ice layer thickness (H_i) on backscatter. Repeating the simulation in Figure 4.3 with different thickness settings, the backscattering coefficients and specular reflectivities are computed and shown in Figure 4.4. It is shown that the scattering strengths fluctuate with respect to ice layer thickness. The fluctuation is caused by the constructive and destructive interference of the waves reflecting between the top and bottom surfaces of the ice layer. The fluctuation period can be calculated from:

$$\Delta H_{ice} = \lambda_{ice} \cos\left(\theta_{ice}^{inc}\right) / 2 = 15.09\, mm , \tag{4.21}$$

which matches the simulation result well in Figure 4.4. Due to the low propagation loss (1.3~1.6 dB/m [101]) in the lake ice at C-band, the average scattering coefficient decay is negligible as the thickness grows. Figure 4.4 also presents the cross-polarized backscattering

coefficients and the specular reflectivities are too small to be displayed in the figure. They are negligible compared to the co-polarized scattering and reflection.

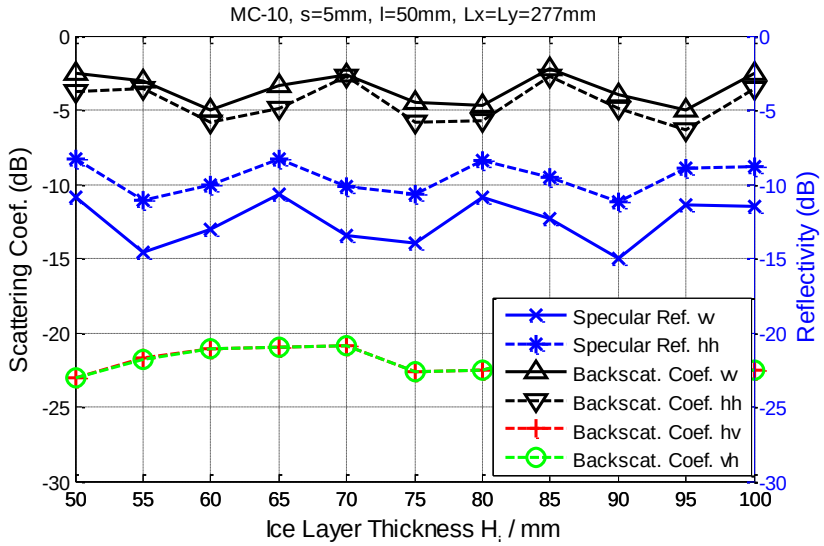

Figure 4.4. Backscattering coefficient and Specular scattering with different polarizations as functions of the lake ice thickness (H_i). Note that the specular reflectivities for hv- and vh-pol are lower than -50 dB and are not shown in the plotting range.

4.3.3 Effects of Columnar Bubble Density (Porosity)

As mentioned before, it is possible that the columnar bubbles interact with the ice/water interface and produce a double-bounce scattering; the predominant explanation for backscatter from floating ice. However, dense randomly located bubbles tend to cancel out their backscattering since their average separation is considerably less than the wavelength in ice and their random phases tend to cancel one another similar to the summation of random vectors. Mathematically, the magnitude of summation of random complex variables is proportional to the square root of the number of variables. Then it can be proven that the backscattering coefficient (power) due to the double-bounce reflection grows linearly for sparsely distributed bubbles. But as the bubbles density increases, the interaction between bubbles increases and the ice-bubble mixture acts as an effective medium for which there is little to no scattering. This region can be treated as uniaxial medium with an effective dielectric constant and the surface scattering

occurring on the region boundaries dominants the scattering. We call this phenomenon as effective medium effect. To verify the analysis, a series of simulations are performed to study the backscattering coefficients variations with volume fraction of air bubbles (porosity). To investigate the level of backscattering coefficient contribution by the double-bounce scattering from bubbles, the ice/water interface is set to be flat in these simulations.

Figure 4.5(a) shows the geometry of simulation scenario, where the periodic boundary conditions and the PML boundary are applied as before. The number of bubbles is calculated for each porosity value. The radii of bubbles are set to be 1.5mm constantly according to field measurements [104][124]. The bubbles are distributed randomly within the simulation domain according to a random number generator and keeping a minimum separation between them. The box size is reduced to 111 mm ($2\lambda_0$) from previous simulations so that thicker ice layers can be simulated. This dimension still allows a Bragg mode to coincide with the backscattering direction. The case without any bubble is firstly simulated to test the accuracy of the model. At ice thickness of H_i =150mm, the flat ice/water interface simulation gives vv-and hh-polarized specular reflectivity of -3.32dB and -2.68dB, respectively, very close to the theoretical value -3.26dB and -2.65dB. The backscattering coefficients are -51dB (vv-pol) and -59dB (hh-pol), indicating that the computational noise (round off errors) is less than -50dB.

In Figure 4.5(b), three different bubble lengths are studied, 50mm, 100mm and 200mm. Each point in the figure is obtained by averaging 10 Monte-Carlo simulations. Models with different bubble lengths share the same bubble distributions. The figure demonstrates that as the porosity increases, initially the backscattering from bubbles increases linearly, e.g., 10dB stronger in scattering coefficients when porosity is increased by factor of 10. When porosity reaches 10%, backscattering starts to drop as the random medium transition to a homogeneous

anisotropic as discussed before. It is interesting to point out that when bubbles have longer length, the effective medium effect appears earlier. This can be explained noting that the longer the bubbles have stronger coherent interaction with other nearby bubbles in the forward direction.

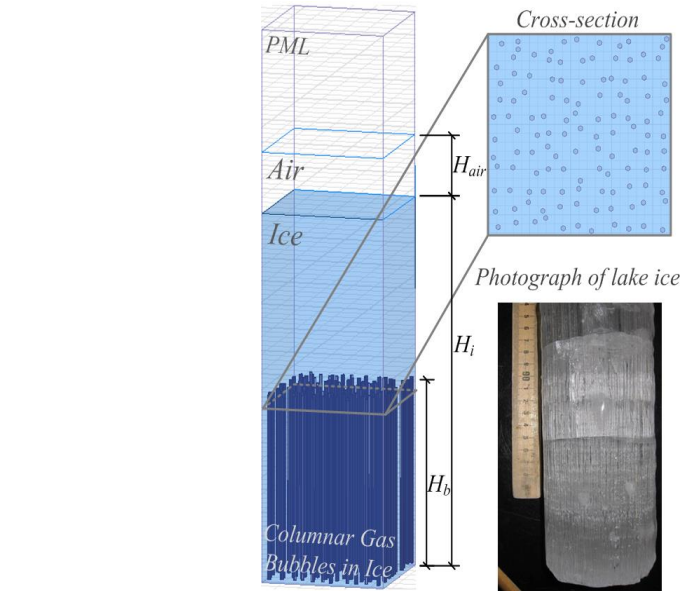

(a)

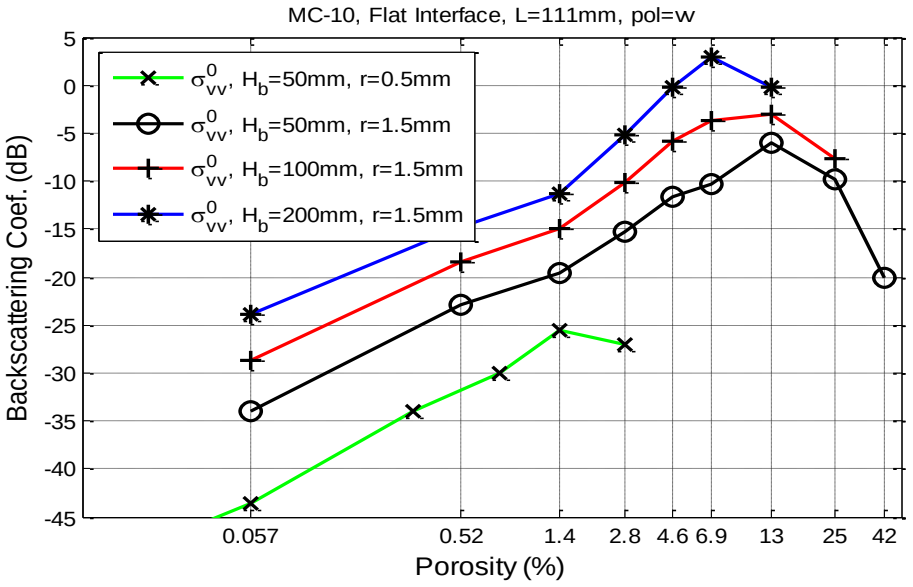

(b)

Figure 4.5. (a) Simulation model studying the backscattering of columnar gas bubbles in lake ice with flat ice/water interface. (b) Simulated backscattering coefficients as functions of porosity at different bubble lengths (H_b) and different bubble radii (r).

4.3.4 Bubbled Ice Thickness

Figure 4.5 (b) also reveals that when the bubble radius reduces, at the same porosity, the backscattering decreases and the effective medium effect appears much earlier. This suggests that for the freshwater ice with thin bubbles (r<0.5mm), the backscattering coefficient is limited to lower than -25dB no matter what porosity it has.

For realistic simulation of scattering from bubbles in freshwater ice, realistic porosity bubble heights are needed. It is known that at 1 atmosphere pressure and 0℃, 1 liter of freshwater can dissolve 0.03 liter of air [125]. If we assume that it is the dissolved air that is released and forms columnar bubbles when water is freezing, the maximum porosity that ice can achieved is less than 3%. Considering the non-uniform bubble distributions a function of depth, the porosity at certain depth can be higher. In Arctic lake ice observations, a maximum porosity is 4.6% is observed, but in most cases measured porosity is smaller than 3% [120]. For running waters when there is higher opportunity of dissolving air in water, such as rivers, ice porosity as high as 7% has been reported [124][104]. It should be noted that the diameter of bubbles vary throughout the ice layer with a maximum air bubble diameter of 0.3 cm. In this simulation model, the columnar bubble's diameter is set to be 0.3 cm and is given the porosity is 2.9%. This is a maximum setting for a freshwater ice to estimate an upper bound for scattering contribution from air bubbles.

Double bounce backscattering coefficient from cylindrical structures varies with length as length squared for cylinders whose length is much larger than the wavelength (H_b / λ >> 1) [126][127].This suggests that when the length of bubbles is doubled, the backscattering coefficient will increase by 6dB. This trend can be seen in Figure 4.5 at low porosity values. However, there are two conditions that are assumed in this analysis. First, the complex

interactions between bubbles, such as shadowing effects or multi-reflection effects, are not considered. These effects should be analyzed with a full-wave simulation, especially for longer bubble lengths or denser bubble distribution. According to Figure 4.5, at porosity of 2.9% and bubble length less than 200mm, these effects are not significant yet. Second, the ice/water interface is assumed to be flat and the bubbles are assumed straight and perfectly vertical. Otherwise, the double-bounce reflection will not be in the backscatter direction. Variations from this assumption cause the backscattering coefficient to increase more slowly than the squared bubble length. The columnar bubbles are not likely to have a long continuous length throughout the ice layer. The bubbled ice usually contains many pieces of short vertical columnar bubbles distributed in the ice layer.

Instead of using long bubbles that grow through the entire bubbled ice layer, we generate some short bubble pieces with an average length of H_b=50mm, as shown in Figure 4.6(a). Their coordinates and length are randomly selected but overlaps are avoided. The porosity is set to be 2.9%.

In Figure 4.6(b) solid curve and dash curves show the average specular reflectivities and average backscattering coefficients for different ice layer thicknesses, respectively. The bars on this figure show the backscattering coefficients derived from each Monte-Carlo simulations, from which average backscattering coefficients are calculated. As the layer thickness is increased, the backscattering coefficients are shown to increase but even at thickness of 400mm it is still less than -10dB. This is an upper bound since a maximum bubble diameter of 3mm is assumed for the cylindrical inclusions. Figure 4.6 (b) shows the hh-polarized backscattering coefficients which is higher than the vv-polarized backscattering coefficients. As explained in [128] this counter intuitive result is due to Brewster angle effect.

Another aspect that needs to be taken into consideration is the effect of rough surface on the double-bounce scattering. Since the double-bounce scattering includes a specular reflection from the ice/water interface. When this interface becomes rough and the specular reflectivity decreases rapidly with increasing surface roughness and thus, the double-bounce reflection is also expected to decrease accordingly. According to rough surface simulations shown previously, there is a reflectivity drop of factor of 6~8dB on both polarization. Hence, the upper limit of the double-bounce contribution to the overall scattering should be less than -16dB in backscattering coefficients, which is by an order of magnitude smaller than the rough surface backscattering coefficients of about -5 dB as shown in Figure 4.4.

It should be mentioned that there is no good way of isolating the double-bounce contribution from the direct rough surface in an exact manner. Part of the problem is that with bubbles are present the effective dialectic constant of the ice layer changes and that affects the scattering from the rough interface.

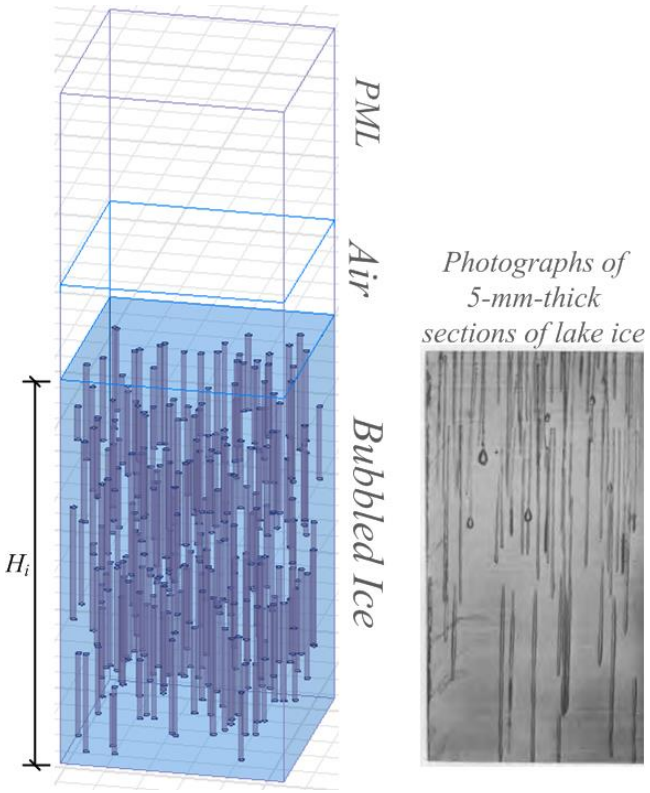

(a)

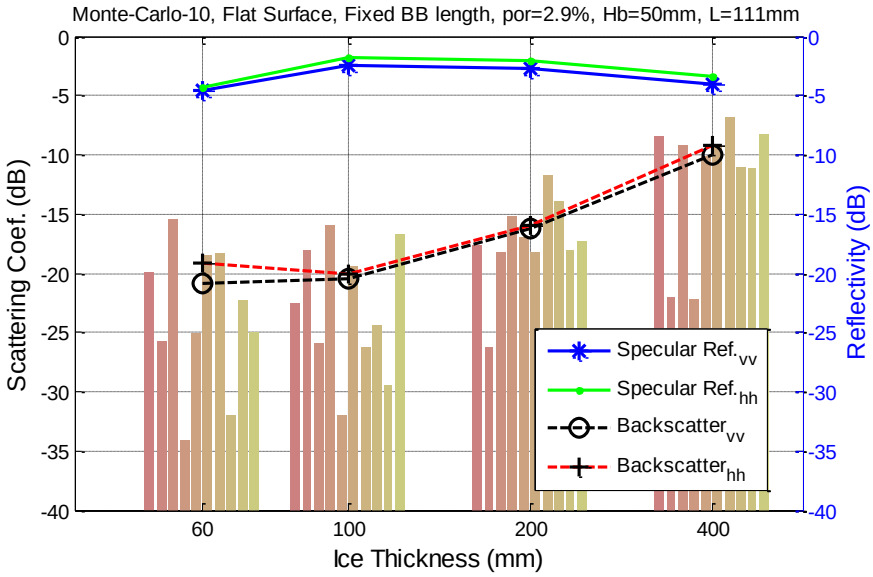

(b)

Figure 4.6. (a) The simulation model studying the backscattering of columnar gas bubbles in lake ice with flat ice/water interface, compared with a photograph of lake ice sample [120]. (b) The simulated backscattering coefficient and specular reflectivity at different bubbled ice thickness (H_i).

The next simulation involves scattering from both bubbles and rough ice/water interface. This simulation accounts for the single-bounce scattering from the rough interface and double-bounce reflection at the same time. As shown in Figure 4.7, when the bubbled ice thickness increases from 0 (no bubbles) to 400mm, backscattering coefficients for both simulations only have minor changes within 3dB. And this can be also caused by the change of effective electric length of the ice layer, which can affect as much as 5dB in backscattering as discussed previously. Bars in Figure 4.7 give the vv-pol backscattering coefficients for individual simulations, which indicate the variations between Monte-Carlo simulations using different random distributions of bubbles. These variations are very small compared with the variations observed in Figure 4.6 (b) for the same bubble density and length. All of these facts verifies that the presence of columnar bubble have a secondary effect on backscattering from lake ice.

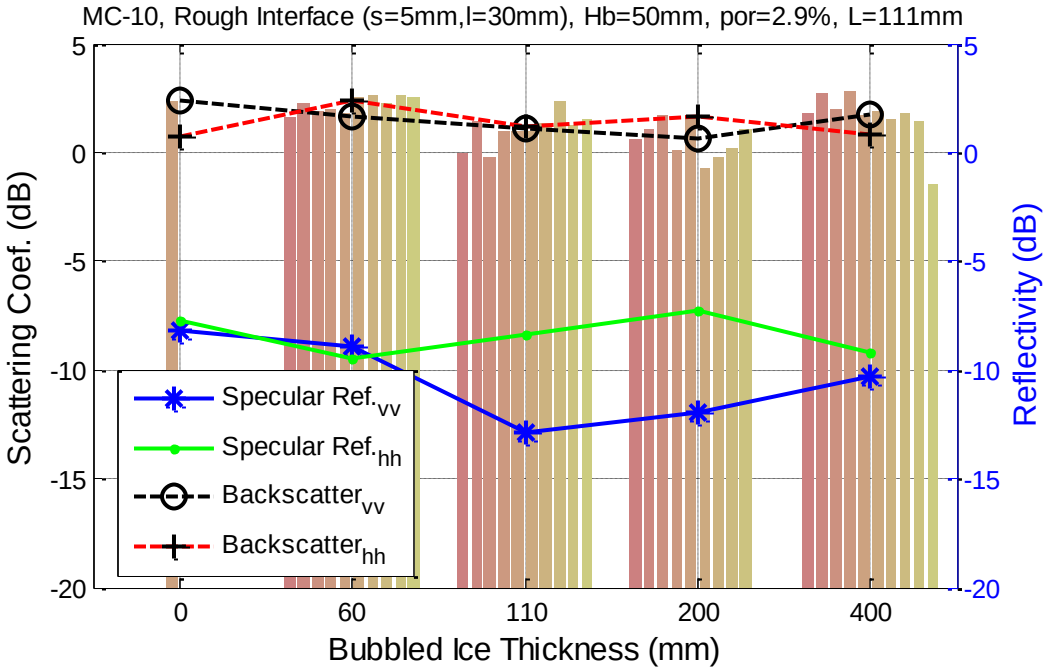

Figure 4.7. The simulated backscattering coefficient and specular reflectivity from columnar bubbles and rough ice/water interface with different bubbled ice thickness (H_{bi}). The rough surface remains the same for all Monte-Carlo simulations.

4.4 Conclusion

In this Chapter two different scattering mechanisms that contribute to radar backscatter from freshwater lake ice are studied. Numerical simulations in conjunction with realistic models of ice layers with air bubble over fresh water are used to carry out the radar scattering phenomenology. The full-wave simulation provides reliable results and high flexibility in modeling. This model is used to study the lake ice scattering problem at C-band. There are two sources that can generate backscatter: 1) rough water/ice interface at the bottom of the ice layer, and 2) columnar air bubbles in ice through a double-bounce scattering mechanism. Without columnar bubbles, the rough ice/water interface generates a strong backscatter which fluctuates periodically with respect to the ice layer thickness. The scattering from air bubbles are also studied and examined with different sweeping parameters such as the bubble length and bubble density (porosity). The results reveal that for the most Arctic lake ice conditions, columnar bubbles contribute less than -16dB to the backscattering coefficients at nominal SAR incidence angles at C-band which is much lower than the backscattering expected from the ice/water rough interfaces.

CHAPTER V

Miniaturized Planar Antenna Design

Previous Chapters have introduced a subsurface imaging system with cross-hole and single-hole setups. An alternative design for such system, known as ground-to-borehole setup, can establish a link between borehole and the surface. For this setup, a planar antenna array is often deployed on the surface as TX or RX. As the operation frequency goes down, the increasing antenna size becomes a problem when considering the mobility of the system. The effort on shrinking the antenna size would be important to the radar sensor design. In this chapter, a miniaturized planar antenna is designed to benefit the design of a low-frequency ground-to-borehole imaging system.

5.1 Introduction

With the recent advances on reactive impedance surface (RIS), which is also referred to as electromagnetic band gap (EBG) material or high impedance surface (HIS) for different applications, this electromagnetic artificial materials surface can minimize the antenna dimension as well as the coupling between the antenna and its image, and hence can easily be matched to 50 Ω lines without external impedance matching networks [51][129]-[131]. But one of drawbacks of using traditional RIS elements is the need for a large area to form a usable RIS substrate. In fact, previous research [132] indicated that traditional RIS substrate performance

degrades and becomes similar to a PEC ground plane when the area or the number of RIS cells is decreased.

Focusing on shrinking the overall size of antenna and RIS substrates, the performance degradation due to RIS substrate size reduction can be attributed to two factors: 1) the limited number RIS unit cells under the antenna, and 2) the limited RIS substrate area under the antenna. The former factor does not allow the proper field distribution for RIS to be established due to the limited number of unit cells. The latter pertains to the fact that only part of the antenna's field can excite the desired RIS mode responsible for antenna miniaturization, that is, the antenna "sees" a mixed RIS and PEC substrate. Fortunately, for the patch antenna, most of its electromagnetic field is concentrated right under the patch, which indicates that the RIS substrate's area can be made almost the same as that of the patch if one can place a large number of RIS unit cells under the patch antenna. This will require shrinking the size of the RIS unit cell to ensure there are enough RIS unit cells in the substrate needed for creating the appropriate field distribution.

In this research, the focus is put on minimizing the cell size of RIS substrate and then using it for designing a very small patch antenna (including its substrate). Simple RIS structures of metallic patches have been utilized in the design of miniaturized planar antennas in previous researches [131]-[136]. However, a typical dimension of these traditional type of RIS cell is about $\lambda_0/20$ in length and $\lambda_0/40$ in thickness (λ_0 is free-space wavelength at the resonant frequency) while usually using a high dielectric constant of 10-12, or even 25. The dimensions of these RIS cells are almost the same as the size of the intended miniaturized planar antenna. Thus, for extreme antenna miniaturization, RIS surfaces with very small constituent elements are needed. To establish the required field distribution within RIS with extremely small elements,

their conventional geometry must be modified. In making single-layer RIS structures small by increasing the gap capacitance, one reaches the fabrication limit very fast as very small air gap widths are not realizable. Sievenpiper et al. presented a two-layer patches structure to achieve a lower resonant frequency [129]. Many similar two-layer RIS structures have been studied [137]-[142], but have not been applied for the application of antenna miniaturization.

In Section 5.2, an two-layer mushroom-like RIS with very small unit cell dimensions (cell area reduction by 95.6% compared to traditional RIS) is proposed and utilized to design a miniaturized antenna over the RIS substrate with the same size as the antenna itself. Based on a surface impedance model, the dispersion diagram of the surface wave is presented and the propagation characteristic of microstrip lines over such RIS substrate is studied. The effect of vias in mushroom-like RIS is also discussed. In Section 5.3, a UHF band patch antenna working at 356 MHz is developed. The overall size of the antenna is reduced to $\lambda_0/11.4 \times \lambda_0/11.4$. The sensitivity of alignment of patch antenna and the RIS substrate is also analyzed. Different sizes of the RIS substrate and the ground plane are tested in the simulation domain. In Section 5.4, several prototypes are fabricated and the measured results are shown to agree with the simulation results very well.

5.2 Reactive Impedance Surface Design

5.2.1 Two-Layer Mushroom-like Reactive Impedance Surface

To make the size of the unit cell small and keeping the thickness and the dielectric constant of the RIS substrate low, as originally suggested in [129], an alternative RIS geometry, consisting of two metallic patch layers and vias, is introduced. As Figure 5.1 shows, the periodic mushroom-like structures on each layer, with same size but different height, are interleaved with

overlapped areas to form the required capacitance. The adjacent patches in different layers are placed with an overlapped width of L_0 and are separated vertically by a thin dielectric (Rogers 4350B) having a dielectric constant of 3.5 and a thickness of 0.1 mm. The lower dielectric (DiClad 522B) has a larger thickness (d=4.75 mm) but a lower permittivity (ε_r=2.5). This way much larger capacitance values can be formed and thus the need for increasing the size of the patch or increasing the inductance can be eliminated. The shape of the patches is modified to octagons in order to maximize the overlap area without increasing the period (the separation between adjacent patches).

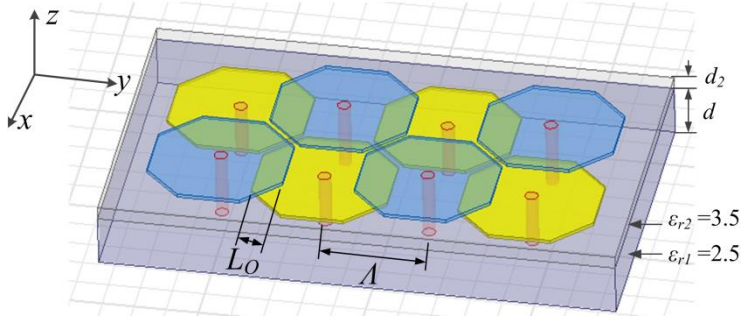

(a) A 2×4 perspective view of the proposed structure

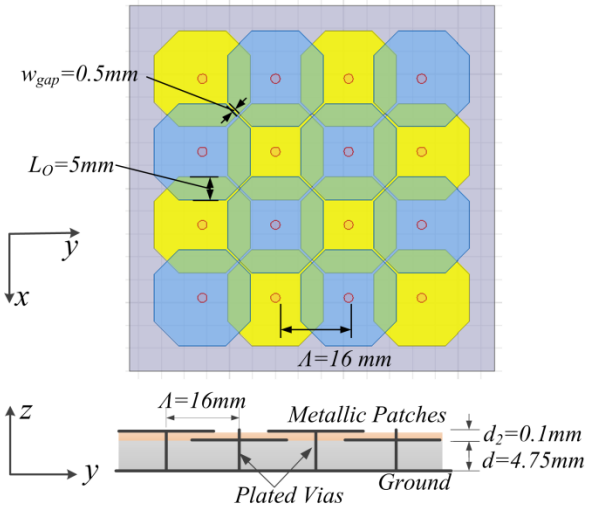

(b) RIS substrate shown in top view and front view, consisting of 4×4 array of RIS units

Figure 5.1. The geometry of the dual layer mushroom-like RIS.

The vias connecting patches and the ground plane form a closed current loop in every single cell and thus ensure that the effective circuit parameters in the RIS region remain the same at oblique incidence and in conditions where the unit cell size is made very small compared to the wavelength. This improves the angular stability of the electrical properties of the RIS structures. Some literatures has demonstrated other structures without via can operate over a wide range of incidence angle [131][141]-[144]. This can be only done when the cell size is relatively large. For the miniaturized RIS cells considered in this design, the inclusion of vias are essential for exciting the desired mode as will be discussed later.

5.2.2 Reflection Phase Analysis

The equivalent shunt LC circuit model of the RIS has been introduced in [129], which can successfully predict the resonant frequency and the surface impedance at normal incidence but fails at very steep incidence angles. A more accurate model based on epsilon-negative (ENG) approximation of the wire-medium (WM) slabs and a grid impedance model for the square patch array has been developed by [144]-[147], and is rearranged as following.

The surface impedance of the RIS Z_S is given by the parallel connection of the WM slab surface impedance Z_{wm} and the grid impedance of the patch array Z_g [139]:

$$\left(Z_S^{TM/TE}\right)^{-1} = \left(Z_g^{TM/TE}\right)^{-1} + \left(Z_{wm}^{TM/TE}\right)^{-1}. \tag{5.1}$$

To apply this analysis for the two-layer RIS, the formulas for WM slab impedance calculation can be directly used as described in [146] (eq.6~9), but the surface impedance of the patch array has to be modified.

The WM slab surface impedance Z_{wm} can be written as:

$$Z_{wm}^{TM} = j\omega\mu_0 \frac{\tan(\gamma d)}{\gamma} \frac{\varepsilon_{r1}k_0^2 - k_p^2 - \beta^2}{\varepsilon_{r1}k_0^2 - k_p^2}. \tag{5.2}$$

$$\gamma = \sqrt{\varepsilon_{r1}k_0^2 - \frac{\varepsilon_{r1}}{\varepsilon_n}\beta^2}\ ,. \tag{5.3}$$

$$\frac{\varepsilon_n}{\varepsilon_{r1}} = 1 - \frac{k_p^2}{\varepsilon_{r1}k_0^2} \tag{5.4}$$

$$k_p = \frac{1}{\Lambda\sqrt{\frac{1}{2\pi}\ln\frac{\Lambda^2}{4r_0(\Lambda - r_0)}}}. \tag{5.5}$$

$$Z_{wm}^{TE} = j\omega\mu_0 \frac{\tan\left(\sqrt{\varepsilon_{r1}k_0^2 - \beta^2}\,d\right)}{\sqrt{\varepsilon_{r1}k_0^2 - \beta^2}}. \tag{5.6}$$

To apply this analysis for the two-layer RIS, the formulas for the surface impedance of the patch array has to be modified. This is calculated based on grip parameter α and the incident angle θ from the normal [145] (eq.16~17),:

$$Z_g^{TM} = -j\frac{\eta_0}{2\alpha}\frac{1}{\sqrt{\varepsilon_{eff}}}. \tag{5.7}$$

$$Z_g^{TE} = -j\frac{\eta_0}{2\alpha}\frac{1}{\sqrt{\varepsilon_{eff}}}\frac{1}{1-\sin^2\theta/(2\varepsilon_{eff})} = -j\frac{\eta_0}{2\alpha}\frac{1}{\sqrt{\varepsilon_{eff}}}\frac{1}{1-(\beta/k_0)^2/(2\varepsilon_{eff})}. \tag{5.8}$$

For the two-layer RIS, the parallel-plate capacitors replace the coplanar capacitors in the conventional RIS, and their value, including the fringing effect, is given by [148]:

$$C = \frac{\varepsilon_{r2}\varepsilon_0 S}{d_2} + \varepsilon_0\varepsilon_{eff}\Lambda\left[0.77 + 1.06\left(\frac{\Lambda}{d_2}\right)^{0.25} + 1.06\left(\frac{t_c}{d_2}\right)^{0.5}\right]. \tag{5.9}$$

This change influences the grip parameter. By comparing the grid parameter for the grid of metal patches and the capacitance in its parallel circuit model in [147] (p.223), a relationship between the grid parameter α and the capacitance C can be established:

$$\alpha = \frac{1}{2}\frac{\eta_0}{\sqrt{\varepsilon_{eff}}}\omega C \ . \tag{5.10}$$

Substitute Eq.(5.2), Eq.(5.7) to Eq.(5.1), one can obtain the expression of the surface impedance of two-layer RIS with vias as a function of frequency and the tangential propagation constant for TM mode. To compute the surface impedance of TE mode, Eq.(5.6) and Eq.(5.8) should be used instead.

Then, the reflection coefficients for the TE- and TM-polarized incident fields can be written as:

$$\rho^{TM} = \frac{Z_S^{TM} - \eta_0 \cos\theta}{Z_S^{TM} + \eta_0 \cos\theta} \tag{5.11}$$

$$\rho^{TE} = \frac{Z_S^{TE} - \eta_0 / \cos\theta}{Z_S^{TE} + \eta_0 / \cos\theta} \tag{5.12}$$

To verify the theoretical analysis, the reflection coefficient characteristics of the proposed RIS have been simulated in Ansoft HFSS by periodical boundary condition and Floquet port. As shown in Figure 5.2, the RIS substrate unit cell is illuminated by a TM plane wave. The periodical boundary condition is setup on the vertical faces to control the plane wave incident angle. The simulated reflection phases at different incident angles are compared with calculated ones, which is given by Eq.(5.11). Figure 5.3 (a) indicates that two-layer RIS has much lower resonant frequency, defined as the zero-reflection-phase frequency at the normal incidence. By increasing the overlap area in the two-layer RIS, the capacitance is increased and consequently the resonant frequency shifts downward. Hence, by changing the overlap width L_O, one can adjust the RIS resonant frequency to the desired values and can easily shrink the unit size to λ_0 /51 × λ_0/51 × λ_0/167 (when L_0=8 mm) and even further. As is shown the resonant frequency has been deceased from 1.75 GHz (single layer RIS) to 0.37 GHz. This is equivalent to shrinking the

cell size to 21% of its original size (area and volume reduction to about 4% and 1% of the original values). This reduction in size comes at the expense of losing the bandwidth. Here the ±90 °reflection phase bandwidth of 21.5% is reduced to 3.7%.

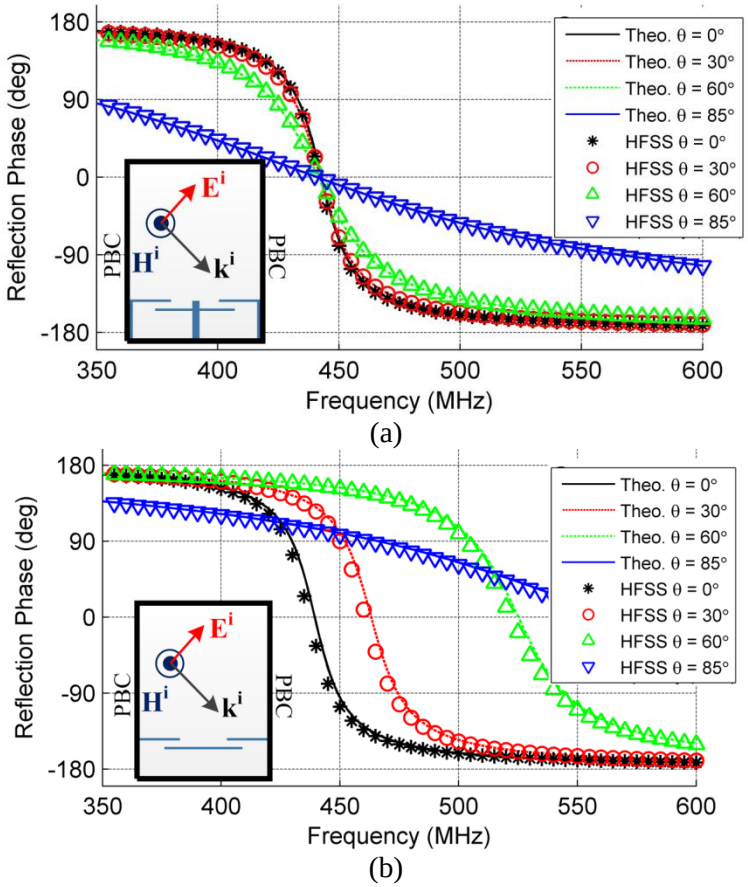

Figure 5.2. Reflection phase plots of two-layer RIS (L_o = 5 mm) at different angles of TM incident waves for (a) RIS with vias and (b) RIS without vias.

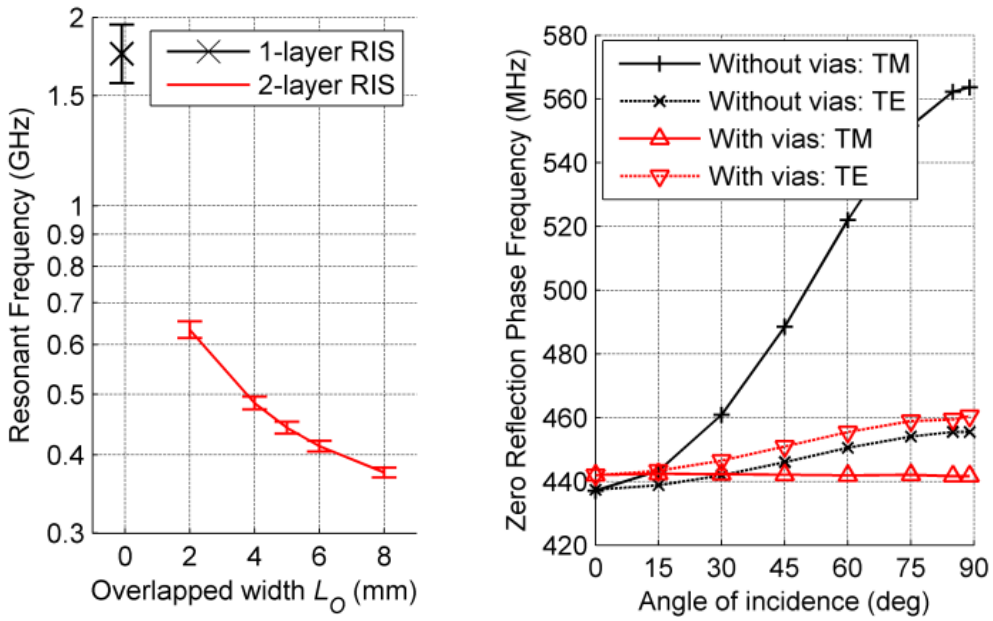

(a) (b)

Figure 5.3. Simulated results of different RIS cell types.
(a) The resonant frequencies of one-layer and two-layer RIS structures with different overlapped width L_O based on unit cell simulations. The ±90 °bandwidths are presented by error bars. The RIS cell size of each type is fixed to 16 mm (L) ×16 mm (W) ×4.8 mm (H). The gap width of non-overlap one-layer RIS is 0.5 mm. Note that the semi-log plot is used. (b) The angular stabilities of RIS with and without vias for L_O = 5 mm at TM and TE modes, respectively.

It is interesting to compare the reflection phases of RIS with and without vias. In theoretical derivation, similar to the RIS with vias, the surface impedance of RIS without vias can be expressed as the parallel connection of the grid impedance z_g and the surface impedance of the dielectric slab z_d [144][145]. Figure 5.2 (a) and (b) compares the incident angle dependence of the reflection phase of RIS surfaces with and without vias. Figure 5.3 (b) also presents the comparison in a different format for both TE and TM polarizations. As observed the TM response of the RIS with vias is much less sensitive to the angle of incidence than that of the RIS without vias.

5.2.3 RIS-mode of Microstrip Line Wave Propagation

If one makes a microstrip line over the RIS substrate, different modes of propagation will be excited. These modes will be referred to the RIS-modes. As will be shown here, the RIS-modes of microstrip line have non-linear propagation constant curves with frequency as opposed to a linear dispersion curve observed for conventional microstrip line over a ground plane. For certain RIS-mode, a substantially higher propagation constant (low phase velocity) can be supported near the resonance. This slow wave propagation leads to a high miniaturization factor for a patch antenna over the RIS substrate.

The theoretical analysis is initially performed on a parallel plate waveguide formed by a top PEC plate and an RIS substrate. The RIS substrate can be represented by a homogeneous impedance surface with a surface impedance of Z_S which is a function of the tangential propagation constant β, shown as Eq.(5.1). Then the relations between the equivalent surface impedance, the height of the RIS/PEC parallel plate waveguide and the propagation constant for TM and TE modes are derived. Considering a TM wave propagating between an infinite large PEC plane and an RIS surface parallel to *xy*-plane with a distance of h, the magnetic field and the electric field can be expressed as a superposition of incident wave and reflected wave:

$$\mathbf{H}_{\mathbf{i}} = Ae^{-jk_z z}e^{-jk_x x}\hat{y} \tag{5.13}$$

$$\mathbf{H}_{\mathbf{r}} = -Be^{jk_z z}e^{-jk_x x}\hat{y} \tag{5.14}$$

$$\mathbf{E}_{\mathbf{i}} = \frac{\nabla \times \mathbf{H}_{\mathbf{i}}}{j\omega\varepsilon} = \left(\frac{k_z}{\omega\varepsilon}Ae^{-jk_z z}e^{-jk_x x}, 0, -\frac{k_x}{\omega\varepsilon}Ae^{-jk_z z}e^{-jk_x x}\right) \tag{5.15}$$

$$\mathbf{E}_{\mathbf{r}} = \frac{\nabla \times \mathbf{H}_{\mathbf{r}}}{j\omega\varepsilon} = \left(\frac{k_z}{\omega\varepsilon}Be^{jk_z z}e^{-jk_x x}, 0, \frac{k_x}{\omega\varepsilon}Be^{jk_z z}e^{-jk_x x}\right) \tag{5.16}$$

Applying PEC boundary condition at $z = h$, $E_{ix} + E_{rx} = 0$, then we have $B = -Ae^{-j2k_z h}$

Then we can rewrite the electric and magnetic field in the waveguide

$$\mathbf{E_t} = \mathbf{E_i} + \mathbf{E_r} = Ae^{-jk_x x} \cdot \left(\frac{k_z}{\omega\varepsilon}\left(e^{-jk_z z} - e^{jk_z z}e^{-2jk_z h}\right), 0, \frac{k_x}{\omega\varepsilon}\left(-e^{-jk_z z} - e^{jk_z z}e^{-2jk_z h}\right)\right)$$

$$= A^{-jk_x x}e^{-jk_z h} \cdot \left(\frac{k_z}{\omega\varepsilon} e\left(e^{-jk_z(z-h)} - e^{jk_z(z-h)}\right), 0, -\frac{k_x}{\omega\varepsilon}\left(e^{-jk_z(z-h)} + e^{jk_z(z-h)}\right)\right)$$

$$= Ae^{-jk_x x}e^{-jk_z h} \cdot \left(\frac{k_z}{\omega\varepsilon}(-2j)\sin\, k_z(z-h), 0, -\frac{k_x}{\omega\varepsilon} 2\cos\, k_z(z-h)\right) \tag{5.17}$$

$$\mathbf{H_t} = \mathbf{H_i} + \mathbf{H_r} = A\left(e^{-jk_z z} + e^{jk_z z}e^{-2jk_z h}\right)e^{-jk_x x}\hat{y}$$

$$= A\left(e^{-jk_z(z-h)} + e^{jk_z(z-h)}\right)e^{-jk_x x}e^{-jk_z h}\hat{y}$$

$$= 2Ae^{-jk_x x}e^{-jk_z h}\cos\, k_z(z-h)\hat{y} \tag{5.18}$$

For simplicity, we let $A_0 = 2Ae^{-jk_z h}$. Rewrite the tangential field as

$$\mathbf{E_t} = \mathbf{E_i} + \mathbf{E_r} = \left(A_0\, j\frac{k_z}{\omega\varepsilon}e^{-jk_x x}\sin\, k_z(h-z), 0, -A_0\frac{k_x}{\omega\varepsilon}e^{-jk_x x}\cos\, k_z(h-z)\right) \tag{5.19}$$

$$\mathbf{H_t} = A_0 e^{-jk_x x}\cos\, k_z(h-z)\hat{y} \tag{5.20}$$

At the RIS boundary $z = 0$, we have the surface impedance

$$Z_S = \frac{E_x(z=0)}{H_y(z=0)} = -\frac{A_0\, j\frac{k_z}{\omega\varepsilon}e^{-jk_x x}\sin\, k_z h}{A_0 e^{-jk_x x}\cos\, k_z h} = -j\frac{k_z}{\omega\varepsilon}\tan(k_z h) \tag{5.21}$$

Thus, we get the dispersion equation for TM mode

$$Z_S^{TM}(\omega, \beta^{TM}) = -j\frac{\sqrt{\varepsilon_r k_0^2 - \beta^{TM\,2}}}{\omega\varepsilon_0\varepsilon_r}\tan\left(\sqrt{\varepsilon_r k_0^2 - \beta^{TM\,2}}\, h\right) \tag{5.22}$$

Similarly, we can derive the dispersion equation for TE mode

$$Z_S^{TE}(\omega, \beta^{TE}) = j\frac{\omega\mu_0}{\sqrt{\varepsilon_r k_0^2 - \beta^{TE\,2}}\tan\left(\sqrt{\varepsilon_r k_0^2 - \beta^{TE\,2}}\, h\right)} \tag{5.23}$$

Using Eq.(5.1) together with Eq.(5.22) and Eq.(5.23), two equations for β^{TM} and β^{TE} are obtained that can be solved numerically. The resulting surface wave dispersion diagrams are

shown in Figure 5.4 (a) and (b), for the RIS plates with and without vias, respectively. The same problem is solved numerically using an FEM solver with periodic boundary conditions on the lateral directions. The results based on modal analysis are compared with the full wave simulations in Figure 5.4 (a) and (b) where very good agreements are shown.

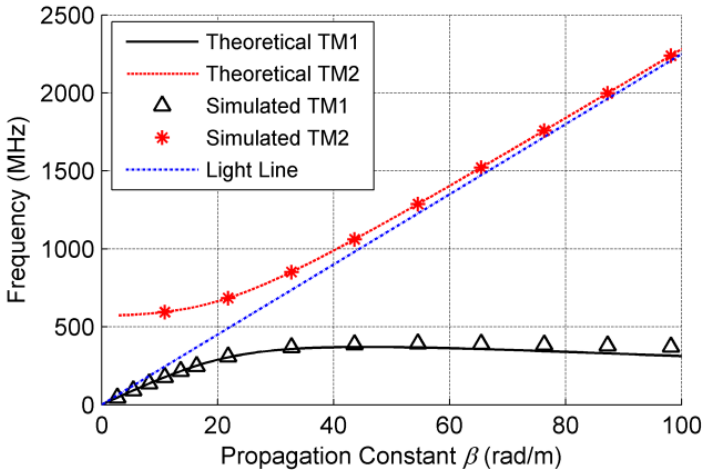

(a) with vias.

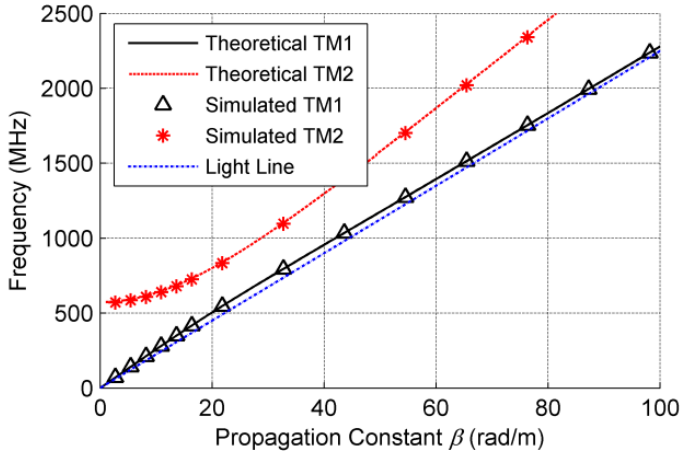

(b) without vias.

Figure 5.4. RIS-mode parallel plate waveguide dispersion diagrams.

As the dispersion diagram Figure 5.4 (a) shows, the dominant mode of propagation in the RIS/PEC parallel plate waveguide (RIS with vias) has propagation constants which are much larger than the propagation constant of conventional parallel plate waveguides (green line) $\beta > k_0\sqrt{\varepsilon_r}$. This means that the phase velocity of TM1 mode is slower than that of a TEM wave

in a PEC parallel plate waveguide. In this case, the surface impedance of the RIS is inductive as described by Eq.(5.22). Near the bandgap, the propagation constant increases drastically with small change in frequency. As a result, the TM1 mode can support a very high propagation constant which is suitable for miniaturizing patch antennas.

For the second TM mode of the RIS/PEC parallel plate waveguide the dispersion curve is above the light line and therefore $\beta < k_0\sqrt{\varepsilon_r}$. According to Eq.(5.22) indicates, the surface impedance is capacitive. A cut-off frequency exists due to the fact that the RIS cannot be capacitive below the resonant frequency. As the frequencies getting higher, the capacitive impedance becomes negligible and the RIS reduces to a metallic surface. Thus, TM2 mode dispersion curve becomes identical to the light line at high frequencies.

Figure 5.4(b) shows that the RIS structures without vias have a dispersion diagram similar to the conventional TEM mode. This is particularly true for situations where the cell size is much smaller than the wavelength. As a result, one cannot take advantage of high propagation constant and miniaturize patch antenna using an RIS structure without vias. Such phenomenon for RIS with and without vias is also reported in [138][145].

5.3 Antenna Miniaturization by RIS Substrate and Choice of Topology

In this section, we take advantage of high propagation constant of RIS-mode microstrip line to demonstrate that a topology-optimized patch antenna can be further miniaturized once placed over the proposed RIS substrate. The additional miniaturization factor is shown to higher than 2.6.

A microstrip patch antenna can be designed to have a patch length slightly smaller than half the effective wavelength at the desired frequency ($\lambda = 2\pi / \beta$). A geometry optimization can

reduce the patch length to a smaller fraction of the wavelength. In order to achieve a higher miniaturization factor, the RIS can be employed to provide a higher propagation constant (shorter wavelength) at the desired frequencies. To estimate the resonance of a rectangular microstrip patch antenna mounted on the RIS substrate, one method is to use the dispersion diagram shown in Figure 5.4(a). For a rectangular patch antenna with length $l = \lambda / 2$, the required propagation constant for microstrip line is $\beta \approx \pi / l$. The intersection of the constant line $\beta = \pi / l$ and the dispersion curve Figure 5.4(a) reveals the operating frequency. However, the fringing effects of the RIS and patch antenna are not considered in this estimation and thus cause an error of a few percent.

It should be noted that for a high propagation constant the surface impedance becomes lossier and thus high miniaturization factor is penalized by lower antenna efficiency. Also the feed location has to be chosen more carefully to achieve antenna impedance matching. For example the smallest rectangular patch antenna can be matched will require an RIS substrate with 3×3 elements and a 48 mm $\times$ 48 mm patch antenna, for which a resonance of 413 MHz can be achieved. The size of this antenna in wavelength is only $\lambda_0 /15$.

A microstrip patch antenna over an RIS can support a horizontal magnetic field and a normal electric field similar to a TM surface wave. For the purpose of patch antenna miniaturization, a high TM mode propagation constant is needed. Since the miniaturized RIS without vias cannot support the TM mode with high propagation constant as shown in the previous section, the inclusion of vias in the RIS structure will be critical. Although some papers show that the RIS without vias can still work as a substrate to miniaturize a patch antenna [131], as the cell size decreases, the propagation constant of TM wave in the RIS-mode microstrip line

decreases to that of the conventional microstrip line and eventually lose its ability to miniaturize the patch antenna.

As we discussed earlier, changing the shape of the radiating patch is an alternative way to miniaturize the antenna. By increasing the edge length of the metallic patch, the required propagation constant can be lower to recover the radiation efficiency. Inspired by this phenomenon, we design a face-to-face Σ-shaped patch antenna configuration, over the RIS substrate, as shown in Figure 5.5 (a) and (b). In this topology, the edge length is almost half the wavelength in the substrate if the antenna were to be designed on a homogeneous dielectric substrate. After much optimization, the size of the patch antenna is reduced to 66 mm × 66 mm or $\lambda_0/11 \times \lambda_0/11$ at the resonant frequency of 410.5 MHz. When using the RIS substrate containing 16 (4×4) cells, the overall antenna size can be limited to 70 mm × 70 mm or $\lambda_0/10.4 \times \lambda_0/10.4$. The antenna's total height is 11.4 mm or $\lambda_0/65$. Comparing with a rectangular patch having the same height and substrate dielectric constant of 4.5 without an RIS substrate, the total size is reduced by a factor of 2.6 (area reduction by a factor of almost 7).

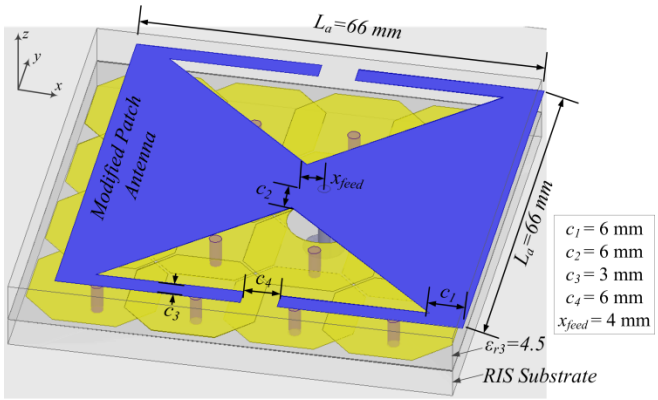

(a) Perspective view

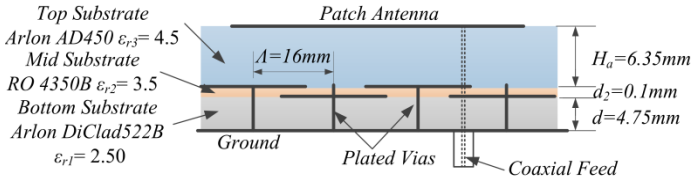

(b) Side view

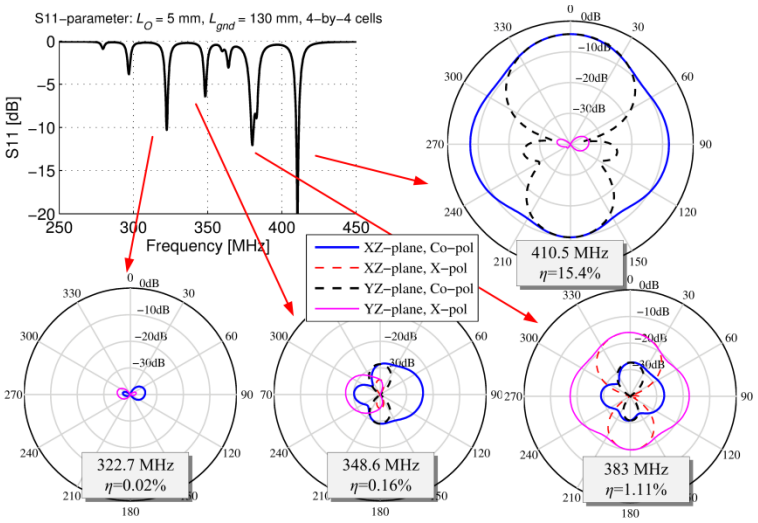

(c) S11 parameter simulation result and simulated radiation patterns and efficiencies.

Figure 5.5. Proposed patch antenna with RIS substrate and the simulation results.

According to the Figure 5.5 (c), the S11 parameter indicates multiple resonances within the band of 300 MHz to 400 MHz. However, after checking the radiation pattern and the radiation efficiency at each frequency, only the one at 410.5 MHz represents the desired mode since the radiation pattern at this frequency is the typical pattern of microstrip patch antennas and the cross-pol radiation at this frequency is also very low. Other spurious resonances at lower

frequencies are due to higher order resonances where propagation constants are higher or contain both x- and y-direction components. Since the TM1 dispersion curve in Figure 5.4(a) shows a negative slope rate at higher β, those higher resonances have even lower resonant frequencies than the desired mode. At these spurious resonances the radiation efficiencies are much lower than the desired mode. It is worth mentioning that the resonance at 383.5 MHz is responsible for the *y*-direction patch antenna mode and results in radiated far-field along *y*-axis, while the desired mode is along *x*-axis. This mode is also inefficiently fed since the feeding point is right in the center in *y*-direction. However, if the feed point were offset from the center, this mode in addition to the x-directed mode would be well-excited. In this case it is possible to design a highly miniaturized circularly polarized patch antenna.

For fabrication of the antenna, the issue of alignment tolerances must be considered. Since the antenna is highly miniaturized, the inhomogeneous nature of the RIS substrate is observable to the antenna. In addition the fringe effect is also sensitive when the antenna edge is close to the edge of the RIS area. To perform the sensitivity analysis, the setup in Figure 5.5(a) is used as the reference antenna. The relative position of the patch antenna with respect to the RIS substrate changes in *x*, *y* and *z* directions, respectively. As shown in Table 5.1, a displacement in *x*- or *y*-directions (in horizontal plane) will not affect the resonant frequencies very much. Using super glue (ethyl cyanoacrylate (ECA)) with a dielectric constant about 3.4 and a dielectric loss tangent less than 0.03 and thickness of less than 200 μm to bond the antenna to the RIS substrate it is found that the change in operating frequency will be less than 0.2%.

Table 5.1. The sensitivity Analysis of Relative Position Offset Between Patch Antenna and the RIS Substrate

Direction	***x***			***y***	
Offset (mm)	-0.8	+0.8	+1.6	+0.8	+1.6
Δf_0 (MHz)	+1.0	-0.15	-0.25	+0.2	-0.05
Direction	***z*** (ECA filled)				
Offset (mm)		+0.2		+0.5	
Δf_0 (MHz)		+0.5		-2.3	

As was previously discussed, using small RIS cells for a patch antenna, the RIS substrate size can be reduced to the same size as the patch antenna itself, without compromising the miniaturization factor. However, the RIS substrate size still influences the resonant frequency and the input impedance of the antenna due to the fringing effects. To explore this effect, a series of simulations are performed by keeping the antenna size constant and changing the RIS substrate. The results shown in Figure 5.6 indicate that the larger is the RIS substrate size, the higher will be the resonant frequency. The reason for this is higher fringing capacitance for the smaller RIS substrate. Another important factor is the size of the ground plane over which the RIS may be placed. Figure 5.6 indicates that larger ground planes will increase the resonant frequency of the antenna. As before the fringing capacitance is lower for larger ground planes and that is why the resonant frequencies shift upward.

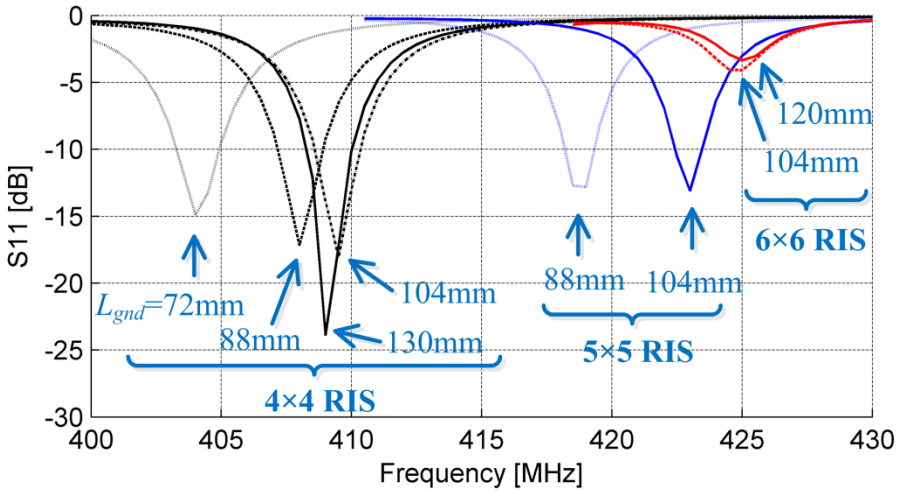

Figure 5.6. The resonant frequencies of the proposed antenna change with different RIS substrate sizes. The effect of ground plane length L_{gnd} is also studied. Each resonance in the figure is marked with its ground plane size and what RIS substrate is used for.

5.4 Prototype Fabrication and Measurements

In this section, prototypes of the RIS substrates and patch antennas are fabricated and measured. The combinations of antenna and several different kinds of RIS substrates are compared. These prototypes are measured and the results are used to examine the validity of the design and the simulation results.

Sensitivity analysis has shown that the position of the patch antenna with respect to the RIS substrate grid and very small gaps filled with super glue between the antenna substrate and the RIS substrate do not affect the antenna performance significantly. But the alignment of the two layers of the RIS patches, as well as the thickness of the dielectric between them will be very important. Hence, the RIS substrates are fabricated by a precision multilayer PCB fabrication method, while the patch antennas are fabricated separately. A few prototypes of the proposed RIS are shown in Figure 5.7.

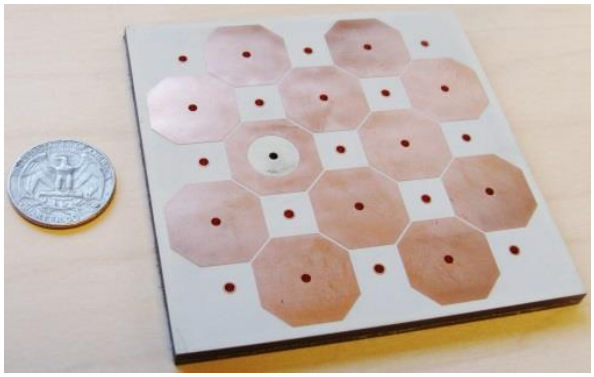

(a) Front side of fabricated 5×5 RIS substrate with overlap width Lo=5 mm

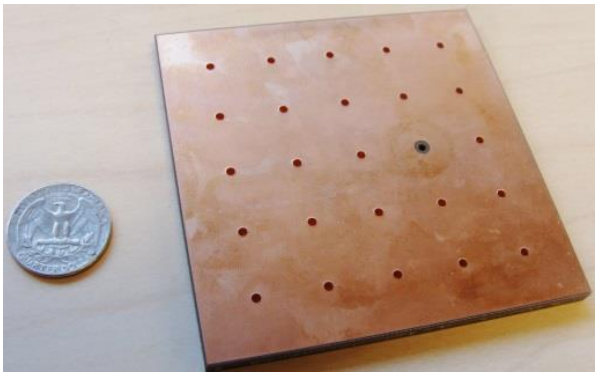

(b) Back side of fabricated 5×5 RIS substrate with overlap width Lo=5 mm

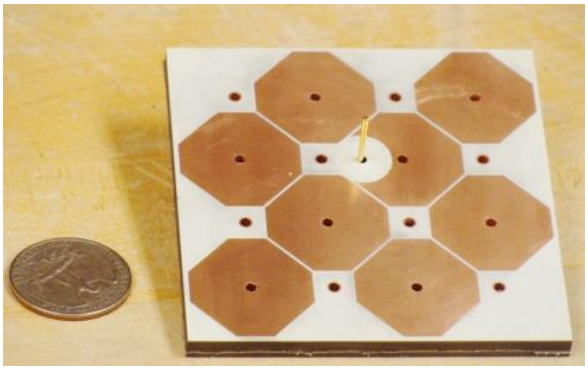

(c) 4×4 RIS substrate with Lo=5 mm, noting that a coaxial probe has been inserted

Figure 5.7. The two-Layer RIS substrate prototype with vias, the size of unit cell is 16 mm×16 mm×4.9 mm.

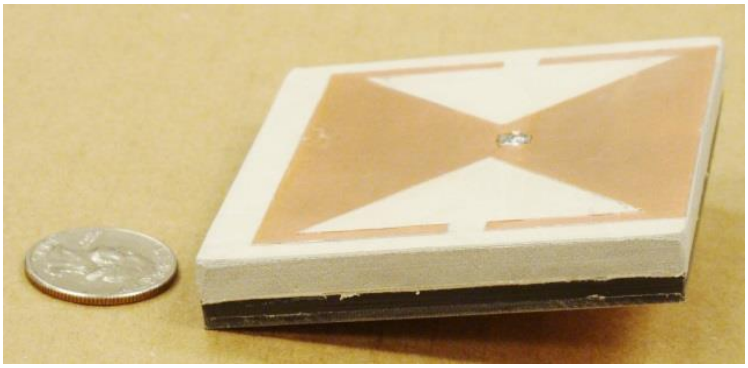

a) The front side

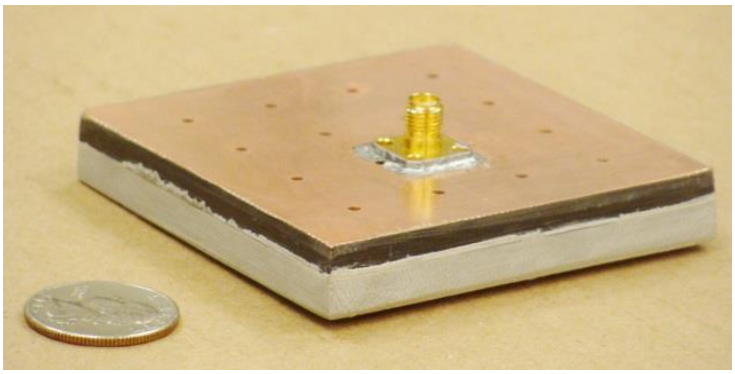

(b) The back side

Figure 5.8. Modified topology patch antenna mounted on a 4×4 RIS substrate.

The patch antenna shown in Figure 5.5(a) is fabricated on Arlon AD450 materials. The antenna is fed using an SMA connector with a long coaxial probe as shown in Figure 5.8. The ground body of the connector is soldered to the back of RIS substrate and the probe is connected to the top of the antenna. Glue is used to bond the RIS substrate and the antenna slab. One of the advantages of fabricating the RIS and the antenna separately is the ability to test several RIS substrate designs with a given antenna or vice versa.

Next the antenna is attached to a ground plane simulating the environment where the antenna is expected to work. The ground plane used in these measurements has a dimension of 130 mm × 200 mm, which is close to the values used in the simulation setup. The input reflection coefficient (S11) is measured using a calibrated vector network analyzer. The S11 in

Figure 5.9(a) shows a good agreement for all resonant frequencies in the spectrum between 250 MHz - 800 MHz. The proper patch antenna response is observed at 420 MHz. This performance is obtained from an RIS substrate with the patch overlap width of L_o =5 mm. The number of cells for the RIS layer under the patch antenna is 25 (5×5 array).

Also the radiation pattern of the antenna was measured in the anechoic chamber of the University of Michigan, and is shown in Figure 5.9(b). The antenna and its ground plane backing were supported by a Styrofoam block which was placed atop a wooden structure connected to an azimuth-over-elevation antenna positioner. The antenna gain was measured using a standard gain antenna and the measured gain is found to be -5dBi, which is the same as simulation result. The radiation patterns in both cuts are slightly different from the simulated results, due to parasitic radiation from the feeding coaxial cable on the back. When the size of ground plane is a small fraction of the wavelength, the ground plane cannot prevent the surface current from flowing over the outer surface of the coaxial cable. The current on the outer surface of the coaxial cable also radiates and contributes to the far-field radiation pattern. As a result, the predicted nulls in the H-plane are filled by the cable radiation. Also the twists and bends of the feeding cable create cross-polarized radiation. However, for the intended application, the antenna is usually directly fed by a small source in the back.

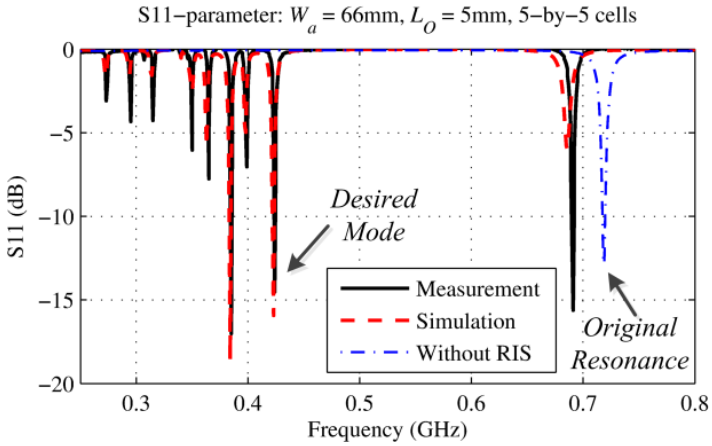

(a) The simulated and measured S11 of a patch antenna over the RIS comparing with that of the same patch antenna over a dielectric substrate.

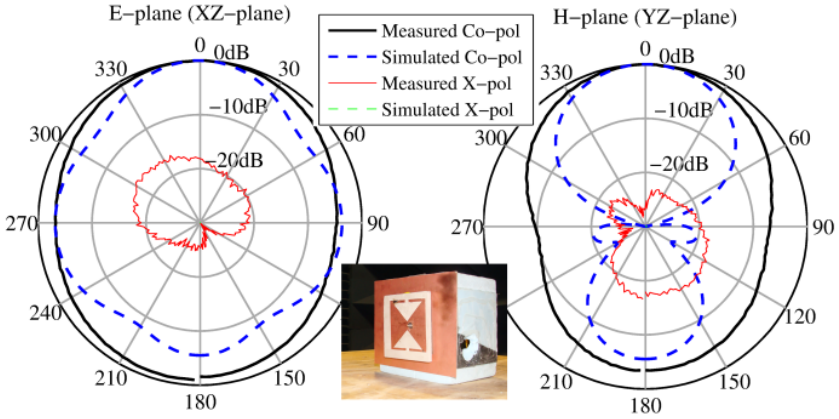

(b) The simulated and measured radiation patterns in the principal planes. The antenna and the RIS substrate are back with a copper ground plane with size of 130 mm×200 mm. Coaxial feed is connected through the back side of the antenna.

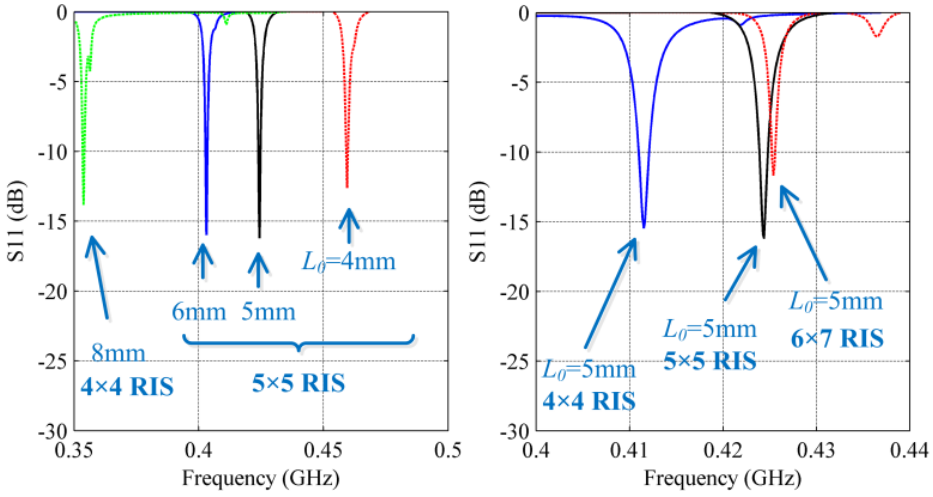

(c) Measured S11 vs. L_o. (d) Measured S11 vs. substrates sizes.

Figure 5.9. The measurement results of proposed antenna.

The overall dimension of the proposed antenna is $\lambda_0/10.4 \times \lambda_0/10.4 \times \lambda_0/65$, including the radiator and the RIS substrate. To address the improvement on the antenna efficiency, a brief comparison on antenna gain between several recently published low-profile planar antennas at lower UHF band is shown in Table 5.2. With the same total lateral size, the proposed antenna achieves approximately 10 dB higher gain than the best design reported. It is also noted that only one published design in Table 5.2 has achieved a total dimension comparable to that of the proposed antenna.

Table 5.2. The Comparison on Gain and Size between Previous Planar Antennas and the Proposed Antenna

Paper	Patch Size	Height	Overall lateral dimensions	Gain
[48]	$\lambda_0/9.9$	$\lambda_0/79$	$\lambda_0/4.9 \times \lambda_0/4.9$	-11 dBi
[49]	$\lambda_0/11$	$\lambda_0/55$	$\lambda_0/11 \times \lambda_0/11$	-15 dBi
[50]	$\lambda_0/9.7$	$\lambda_0/34$	$\lambda_0/5.1 \times \lambda_0/5.1$	-7.9 dBi
[51]	$\lambda_0/13$	$\lambda_0/60$	$\lambda_0/5 \times \lambda_0/5$	-3.9 dBi
This design	**$\lambda_0/11$**	**$\lambda_0/65$**	**$\lambda_0/10.4 \times \lambda_0/10.4$**	-5 dBi

Some parametric studies are shown in Figure 5.9 (c) and (d). To perform these studies, we use the same patch antenna with RIS substrates either having different the cell number or different overlap width L_O. When increasing the overlap width L_O of RIS from 4 mm to 8 mm, the resonance of the patch antenna decreases as predicted by simulation. Reducing the number of RIS cells from 6×7 to 5×5 and then to 4×4 will decrease the resonant frequency slightly. This agrees with the simulation analysis in Figure 5.6.

Among all the combinations we fabricated and measured, the lowest resonant frequency is 356 MHz, achieved by using RIS with L_O=8mm containing 4×4 cells. The overall size of the antenna and RIS substrate for this prototype is 74 mm × 74 mm × 11.4 mm or $\lambda_0/11.4 \times \lambda_0/11.4 \times \lambda_0/74$. If the rectangular patch antenna without the RIS but on the same dielectric is used as the reference antenna, the miniaturization factor is 2.7.

5.5 Conclusion

A two-layer overlapped mushroom-like reactive impedance surface is studied in this chapter and is used for designing a miniaturized patch antenna with very small overall volume. The key point to this design is realization of a functional small size RIS substrate that consists of compact size of two-layer RIS unit cells using a low permittivity material. Placement a finite number of such unit cell directly under a planar antenna with the overall lateral dimensions not exceeding the original antenna's boundary, realization of a very small patch antenna is possible.

The surface impedance and the wave propagation characteristics of the two-layer mushroom-like RIS are reviewed and compared with the same design without vias. The importance of the vias is addressed. The propagation constant of the RIS/PEC parallel plate waveguide is studied to accurately predict the ability of miniaturization factor for a patch antenna over the RIS substrate at a desired frequency.

Finally, a topology optimized patch antenna over the two-layer overlapped mushroom-like reactive impedance surface is designed using low dielectric constant material. The resulting patch antenna is shown to have a very small volume ($\lambda_0/11.4 \times \lambda_0/11.4 \times \lambda_0/74$). Compared to existing planar antennas with similar dimensions, the proposed antenna achieves a remarkable efficiency.

The salient feature of the proposed antenna include: 1) no requirement for lossy external matching network, 2) planar architecture with extremely low profile ($\sim\lambda_0/74$), 3) a very stable resonant frequency that is not affected by the size of the metallic plane or dielectric surface on which the antenna is mounted, 4) ease of fabrication using the standard multilayer PCB fabrication process, and 5) polarization purity which can easily be exploited to design highly

miniaturized circularly polarized or dual polarized antennas. Due to these properties, the proposed antenna is suitable for many applications in the complex environments such as RFID tags as well as, mobile and wearable devices. The antenna topology is also appropriate for designing on-chip antenna at much higher frequencies.

CHAPTER VI

Small Planar Azimuthal Omnidirectional Circularly Polarized Antenna

6.1 Introduction

As we discussed in Chapter I, circularly polarized (CP) antennas are commonly needed for imaging radar and many other systems. Azimuthal omnidirectional antenna gives radar system $360°$ azimuthal coverage, which is desired by surveillance radars and some imaging radars.

In this Chapter, a planar CP antenna with azimuthal omnidirectional radiation pattern is designed. The CP polarization is synthesized by combining two linearly polarized omnidirectional antennas and feeding them with signals having the same amplitude but 90 degree phase difference. When placing the antenna vertically and letting the horizontal plane (azimuthal plane) to be the omnidirectional radiation plane, one will need a horizontally polarized antenna and a vertically polarized antenna. Both antennas should have azimuthal omnidirectional radiation. As will be introduced in Section 6.2, the first antenna is a vertically oriented slot antenna on a small ground plane with horizontally polarization. To achieve that, the radiation null on the E-plane that exists on conventional slot antennas is removed by constructing a parallel plate waveguide delay line between the two sides of the antenna and forming an antiparallel field distribution on the aperture of each side. As a result, the far field radiation from both apertures adds up in phase and becomes uniform. The other antenna, in Section 6.3, consists

of two PIFA elements which contribute to vertical polarization to the radiation pattern. Section 6.4 introduces the feeding network that splits the input power equally to excite both antennas and introduces an extra 90 degree phase delay for one of the antennas. The feeding network is realized by microstrip lines and is optimized to have an axial ratio lower than 1.3. The gain of this small antenna is 1dB with small fluctuation as a function of angle in the azimuthal plane. Section 6.5 describes the fabrication process and presents chamber measurement results.

6.2 Horizontally Polarized Antenna Design

Loop antennas are common structures to build a horizontally polarized antenna but oftentimes it is hard to avoid a complex 3D structure when combining with a vertically polarized antenna and feeding network. If one considering a planar structure, Babinet's Principal states that a complementary planar antenna has an identical radiation pattern but an orthogonal polarization (E-filed and H-field directions exchange). Thus, a slot antenna, which is the complementary antenna to a conventional dipole, should have a donut-shaped pattern as a dipole antenna has but should be horizontally polarized, shown in Figure 6.1 (a). Here, slot antenna is placed vertically or aligned with *z*-axis. However, the dissatisfaction for the assumption of infinite ground plane prevents people from using a simple slot to achieve an omnidirectional antenna with horizontal polarization. The finite ground plane introduces radiation nulls on the antenna plane at *x*-axis direction in Figure 6.1. To analysis the radiation from a slot, the tangential electric field inside the slot can be equivalently considered as magnetic currents on both sides of the slot. However, the magnetic currents on two sides have opposite directions due to the flip of the normal vector and consequently the far-field electric fields on the two sides of the ground plane are anti-parallel, as shown in Figure 6.1 (b). They tend to cancel each other and create radiation nulls at

the plane of the slot, as shown in Figure 6.1 (c). This phenomenon prevents a finite-ground-plane slot antenna from having an omni-directionality on azimuthal plane (*xy*-plane).

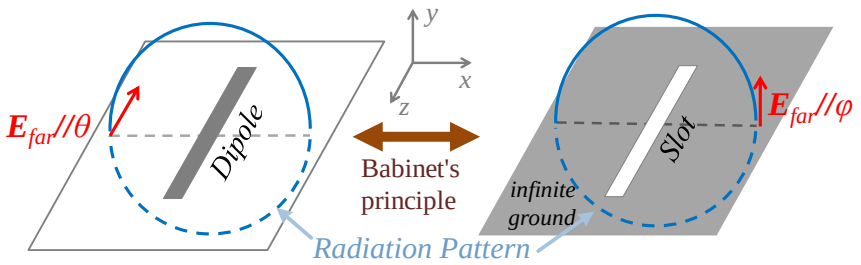

(a) Infinite-ground-plane slot antenna has an omnidirectional radiation pattern predicted by Babinet's Principle.

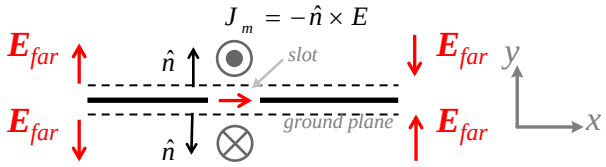

(b) Finite-ground-plane slot antenna can be equivalently treated as two anti-parallel magnetic currents and the far field electric field due to them tend to cancel each other at the x-axis direction.

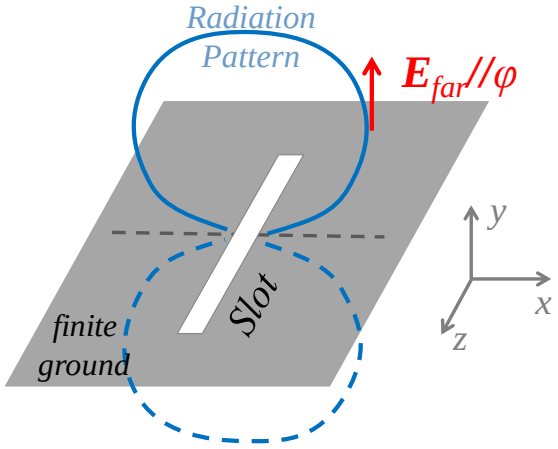

(c) Finite-ground-plane slot antenna has radiation nulls on azimuthal plane.

Figure 6.1. Slot antenna radiation pattern analysis

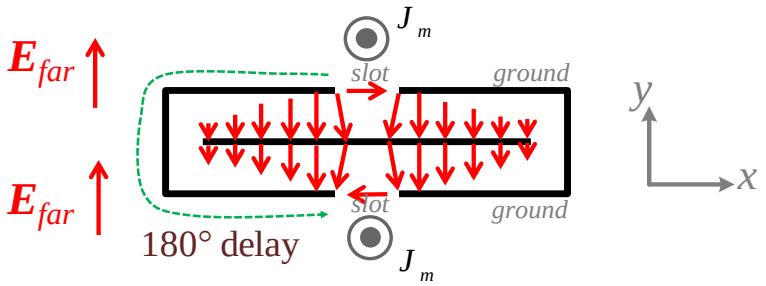

Figure 6.2. Use parallel plate waveguide as 180 °phase shifter for the slot antenna.

Even though a slot antenna naturally has radiation nulls on the antenna plane as depicted in Figure 6.1 (c), and explained in Figure 6.1 (b), one can make some modification to a conventional slot antenna to remove the nulls on azimuthal plane. Firstly, as shown in Figure 6.2, increase the thickness of the ground plane and open identical slots on both sides. Then, insert a parallel plate waveguide phase shifter of 180 °phase delay between the two sides of the ground plane. This measure manipulates the equivalent magnetic currents on both sides to be in-phase and then forces two slots radiating identical electric field at *x*-axis direction where nulls exists for the conventional slot antenna. As a result, if one designs a slot antenna as demonstrated in Figure 6.2, there will not be any radiation null on the *xy*-plane.

The concept of azimuthal omnidirectional slot antenna in Figure 6.2 can be realized at 2.4 GHz as Figure 6.3 shows. Instead using a 1-fold parallel plate waveguide, using a 3-fold parallel plate waveguide will reduce the antenna's width and improve the omni-directionality. As shown in Figure 6.3, several *x*- and *y*-direction metallic walls are inserted between the front slot and the back slot. Two outer metallic walls on narrow sides connect two ground planes on the front and on the back, and also connect to inner walls. The top end and the bottom end of the antenna are remaining open-circuited. Otherwise, a short end will make the inner structure into a rectangular waveguide, which suffers from strong dispersion effect and higher order modes interference, compared to parallel plate waveguide. The inner area is filled by dielectric (RO4003C, ε_r=3.55),

to mechanically support the structure and shrink the volume of the waveguide phase shifter. The 180 °phase shifter has two mirror-symmetrical paths and each path has a length of 36 mm, which is approximately equal to half wavelength in the dielectric.

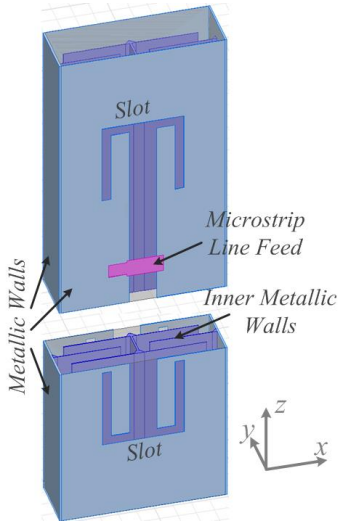

Figure 6.3. Slot antenna geometry demonstration. A 3-fold parallel plate waveguide is inserted between the front slot the back slot. In this figure, antenna is cut to into two parts to show the cross section.

The length of the slot for a conventional slot antenna is half wavelength in freespace. Considering the margin on the ground plane, the slot antenna length has to be larger than half wavelength. In order to achieve a compact size, the slots in the proposed antenna are modified into a back-to-back C-shaped geometry, as shown in Figure 6.3. To make the antenna resonant at 2.4 GHz, each C-shaped slot has a contour length of half wavelength. Finally, the overall size of the proposed slot antenna is only 58 mm $\times$ 18 mm $\times$ 6.5 mm, corresponding to 0.46 λ_0 $\times$ 0.14 λ_0 $\times$ 0.05λ_0.

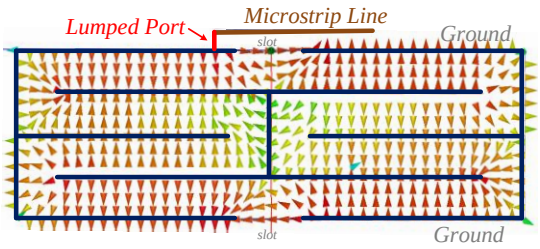

Figure 6.4. 3-fold parallel plate waveguide field distribution on its cross section plane

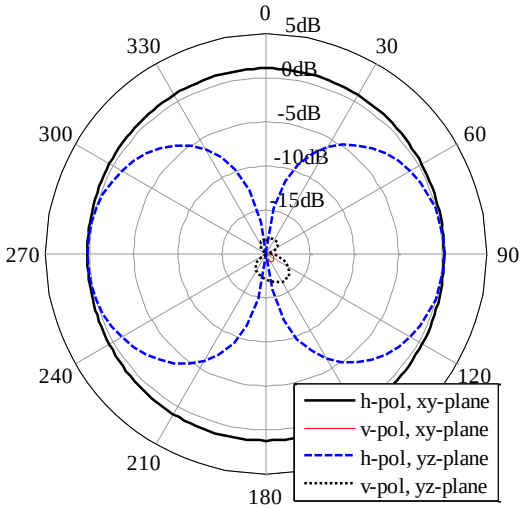

Figure 6.5. Proposed slot antenna with a lumped-port feeding shows an omnidirectional pattern on xy-plane and good cross-pol isolation.

The proposed slot antenna is initially fed by a lumped port and a small piece of microstrip line in front of the antenna. Once the front slot is excited, the wave will propagate along the 3-fold parallel plate waveguide to the back slot. As shown in Figure 6.4, the wave propagation experiences a phase delay of 180 °, so the field distribution presents a field flip in the middle of the waveguide and the field orientations on the front and back slot become opposite. As expected, Figure 6.5 shows a good omnidirectional horizontally polarized radiation pattern on *xy*-plane. Due to the symmetric design, the cross-pol isolation from the slot radiation is very good.

6.3 Vertically Polarized Antenna Design

Many candidate antennas are suitable for generate vertically polarized waves with an azimuthal omnidirectional pattern, such as monopole antenna, microstrip patch antenna, and inverted-F antenna. In this design, considering the existing metal structure of the slot antenna, a planar inverted-F antenna (PIFA) is more locational flexible and spatially efficient. However, PIFA usually is not outstanding on the aspect of omni-directionality and polarization purity due to the asymmetry of feeding position. To improve the symmetry, a pair of PIFAs is placed on the shoulders of the slot antenna, with the shoring plates connecting to the side wall, as shown in Figure 6.6. Any horizontally polarized radiation from one PIFA will be cancelled by the other one, so high cross-pol isolation can be expected. Another advantage of using PIFA pair is that the phase center will be moved to the symmetry plane. It is very important when combining the vertically polarized antenna and the horizontally polarized antenna into a CP antenna, that they should have the same phase center on *xy*-plane.

A dielectric slab is used to support each PIFA. Using RO5880 (ε_r=2.2), the slab thickness of 3.2 mm is selected. The width of the slab is 6.5mm and the length is 58mm, which are identical to the dimensions of the side wall. PIFA is optimized to have a 20.8 mm × 6.5 mm patch and a 5 mm × 3.2 mm shoring plate. A microstrip line is connected to each PIFA. Due to the mutual coupling between the PIFA pair, the input impedance of the pair is not simply equal to two individual input impedances in parallel. A quarter-wavelength impedance transformer is used to match the impedance to 50 Ω. The PIFA pair is fed by a 50 Ω lumped port excitation. The radiation pattern is shown in Figure 6.7.

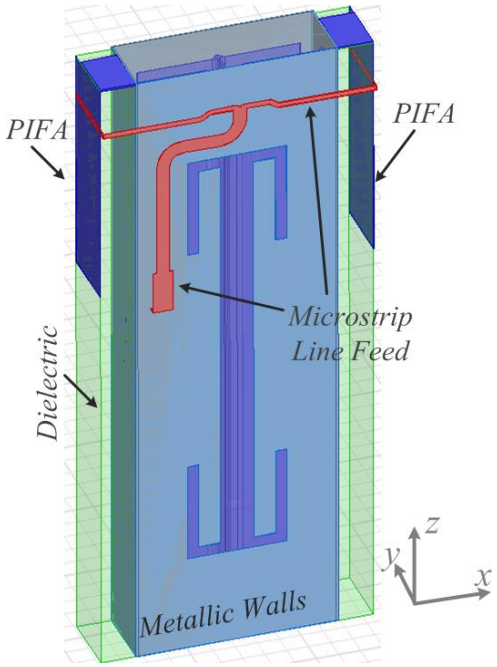

Figure 6.6. PIFA pair mounted on the side of the slot antenna forms a vertically polarized antenna.

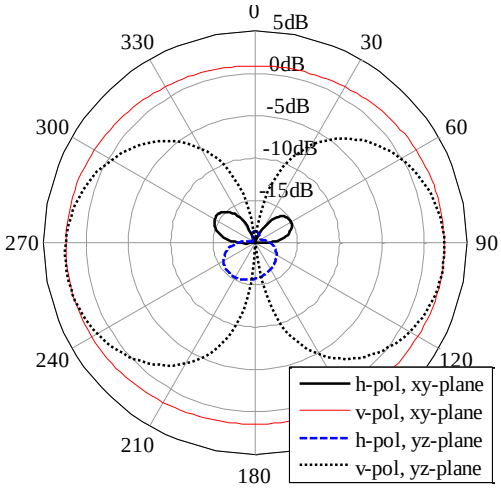

Figure 6.7. PIFA pair matched by microstrip line feeding network presents omnidirectional pattern on vertical polarization on xy-plane.

6.4 Feeding Network Design for Circularly Polarized Antenna

As described in Section 5.3 and Section 5.4, a horizontally polarized antenna (slot antenna) and a vertically polarized antenna (PIFA pair) are designed separately. Both antennas have good azimuthal (*xy*-plane) omnidirectional patterns and their patterns on the other principle

plane (*yz*-plane) are also very similar. This implies that only if one can simultaneously excite both antennas with a proper phase difference, a circularly polarized omnidirectional radiation pattern can be synthetized. Since both antennas are fed by microstrip line on the front, a microstrip line feeding network can be consequently designed to connect both antennas. a thin PCB layer, with microstrip line network printed on it, can be placed atop the front side of the slot antenna. The ground plane of the slot can be also used as the ground of microstrip line. If the microstrip do not overlap with the slot, its effect to the slot antenna is acceptable.

Before feeding network is designed, two antennas have to be matched separately. In Section 5.3, PIFA pair is already matched by a quarter-wavelength impedance transformer. The slot antenna then is needed to be matched. A series open-end stub on the left-hand side of the slot and a shunt open-end stub on the right-hand side are used to form the matching circuit. With fine tuning procedures, both antennas can be matched to 50 Ω microstrip lines at 2.4GHz. Figure 6.8 shows the two-port S-parameters when two antennas and their matching circuits are fed by two lumped port separately.

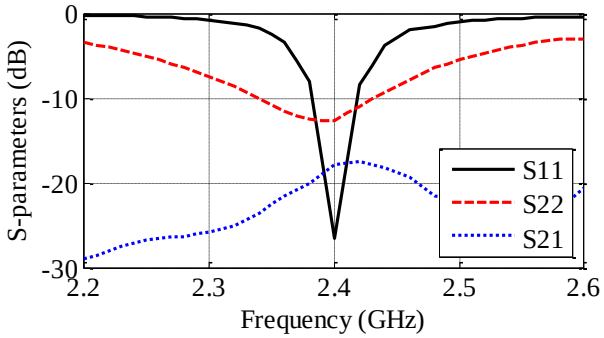

Figure 6.8. Horizontally polarized antenna (slot antenna fed by port1) and vertically polarized antenna (PIFA pair fed by port2) are both matched at 2.4GHz when fed separately.

To combine two antennas, a 3dB Wilkinson power divider is employed. It is worth mentioning that the Wilkinson power divider not only keep the impedance matched at all ports, but also isolate two antennas, which is important to improve the cross-pol isolation. On the

contrary, when splitting the power for feeding PIFA pair, a simple T-junction is used since there is no necessity to isolate two PIFAs. As shown in Figure 6.9, the first port of the Wilkinson power divider is connected to a coaxial probe which is the input port of the proposed antenna. In order to solder the coaxial probe, the PCB containing feeding network has extended by extra 5-mm on the bottom of the antenna. The overall feeding network is shown in Figure 6.9. The PCB dielectric is RO4003C (ε_r=3.55), with thickness of 0.8mm.

In the feeding network, the branch connecting to PIFA pair is about quarter-wavelength longer than the other branch that feeds the slot antenna. To adjust the phase delay precisely, the T-junction close to PIFA pair can be moved up and down, which provides a tunability of about 30 °. In simulations, the far field electric field phase can be observed and to help tuning the phase difference, as shown in Figure 6.10. As discussed above, keeping the phase center of both polarizations at the same position is very important. Otherwise, the phase difference will change dramatically at different azimuthal angles, that is, the curves in Figure 6.10 will have much more fluctuations.

The feeding network in Figure 6.9 makes the antenna to be right-handed circularly polarized (RHCP). If the mirror-imaged structure of the current feeding network with respect to x=0 plane is used, the antenna will be left-handed circularly polarized (LHCP).

Simulated results are shown in Section 5.5, Figure 6.13 – Figure 6.15, compared with measured results. By optimizing the feeding network, the proposed antenna can be matched at 2.4 GHz with a bandwidth of 40 MHz and the axial ratio can be lower than 1.3. The gain of this small antenna is 1dB with small fluctuation as a function of azimuthal angle on horizontal plane.

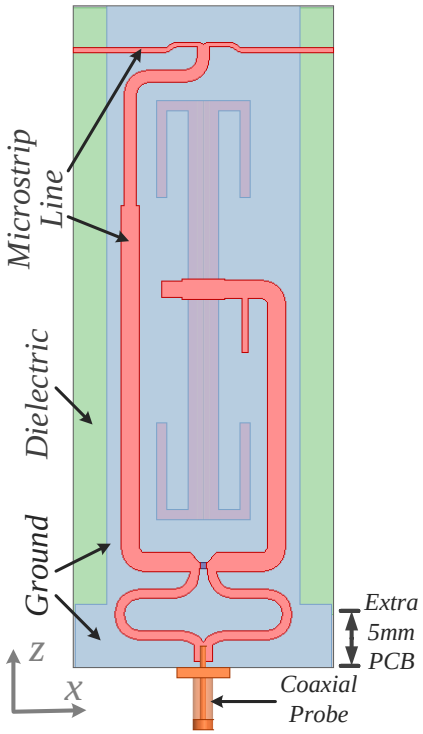

Figure 6.9. RHCP polarization feeding network for proposed antenna.

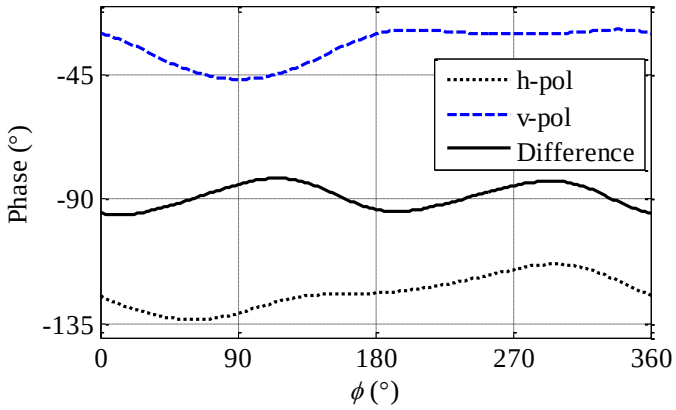

Figure 6.10. Phase of electric fields of far field radiation on *xy*-plane. Solid line shows the phase differences between two linear polarizations at different azimuth angle.

6.5 Fabrication and Verification

The fabrication process of the proposed antenna is based on the standard PCB fabrication with some soldering and gluing procedures. The slot antenna in Figure 6.3 is firstly fabricated, which consists of six pieces of PCBs in four layers, as shown in (b) The slot antenna along with PIFAs and microstip line feeding network composes the proposed antenna.

Figure 6.11 (a). The *x*-direction inner metallic walls shown in Figure 6.3 are composed by the metallization of PCBs, while the *y*-direction walls are copper strips that are soldered perpendicular to the PCB pieces. PCBs are assembled into a rectangular box shape, using regular super glue (ethyl cyanoacrylate (ECA), ε_r=3.4, tanδ=0.03). Note that since some soldering joints are inside the antenna, small parts of PCBs are filed so that there is enough room for solder alloy. Next, the slot antenna, two pieces of PIFA and a microstrip line PCB are glued together. Finally, the coaxial probe connecter is soldered on the bottom edge of the PCB. The assembled antenna is shown in Figure 6.12. The overall dimension of the antenna is 63mm × 24.8 mm × 7.3 mm, corresponding to 0.5 λ_0 × 0.2 λ_0 × 0.06 λ_0, excluding the coaxial connecter.

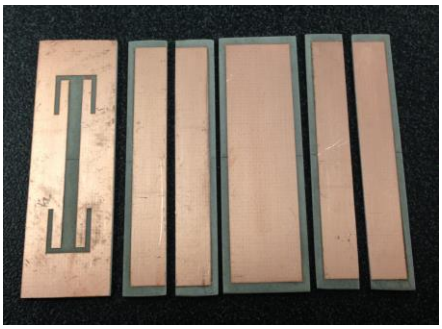

(a) The slot antenna consists of six pieces of PCBs.

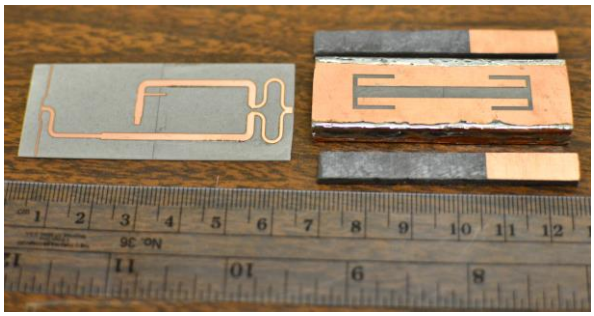

(b) The slot antenna along with PIFAs and microstip line feeding network composes the proposed antenna.

Figure 6.11. The fabrication of proposed antenna.

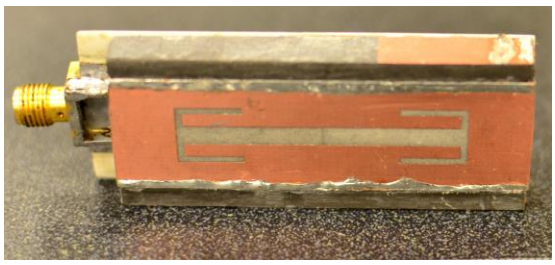

(a)

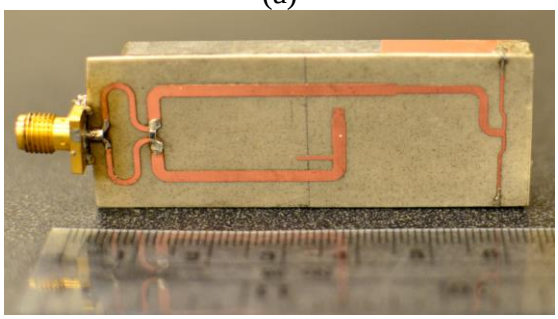

(b)

Figure 6.12 . (a) The front side and (b) the back side of the fabricated antenna.

The radiation pattern of the proposed antenna is measured in the anechoic chamber of the University of Michigan, and it is shown in Figure 6.14. The antenna is fixed on a Styrofoam

block with some paper tapes, with antenna's *z*-axis aligned vertically. The antenna and the block are placed atop a Styrofoam stand connected to an azimuth-over-elevation antenna positioner. Antenna is fed by a coaxial cable through the center of the turning table as shown in the picture of Figure 6.14. Antenna gain is measured using a standard-gain antenna, and the measurement is only performed on two linear polarizations (h- and v-pols). Since the phase and amplitude of measurements are recorded, RHCP and LHCP pattern can be synthesized in post-processing. As a result, a difference of 1-2 dB between the simulated and measured RHCP gain can be observed on some azimuthal angles. The cross-pol isolation is better than 12 dB. The antenna can achieve axial ratios less than 1.8 over the entire azimuth plane as shown in Figure 6.15. Although the efficiency measurement is not performed due to the lack of 3D scanning facilities, there is a 1~2dB gain drop according to the gain measurement. The loss is possibly introduced by fabrication errors and assembly problems, such as imperfect soldering and misalignment, which are hard to avoid in complicated assembly processes. The pattern distortion can be caused by the coaxial cable in the chamber. These feeding cables can reflect waves and affect the measured pattern, especially for an omnidirectional antenna. Overall, the measured performance still has a good agreement with the simulation results.

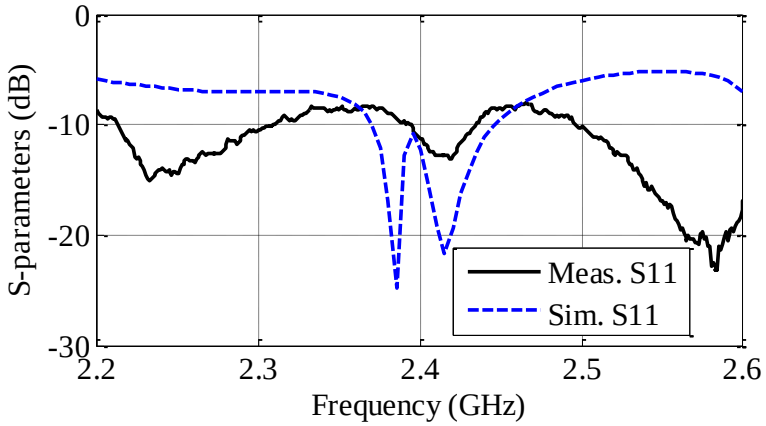

Figure 6.13. Measured and simulated S11 parameter.

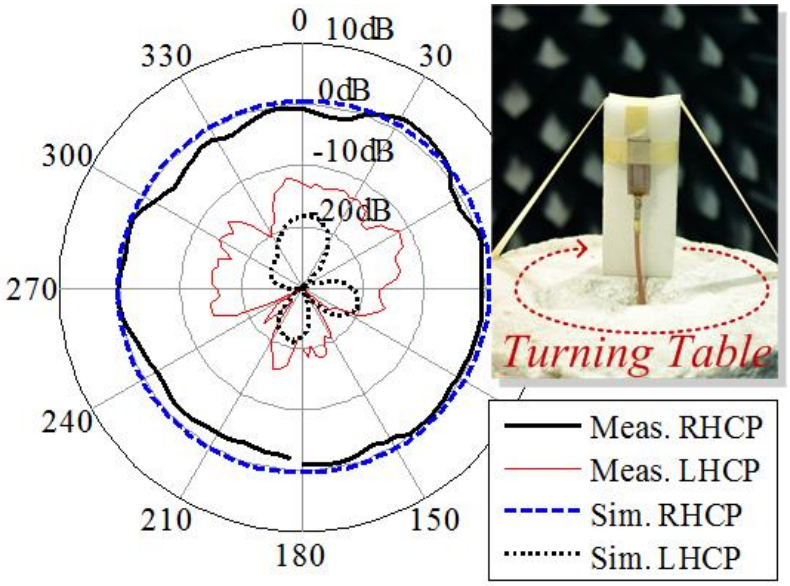

Figure 6.14. Measured and simulated right-handed circularly polarized (RHCP) and left-handed circularly polarized (LHCP) radiation pattern on azimuth plane when antenna is vertically placed on the turning table.

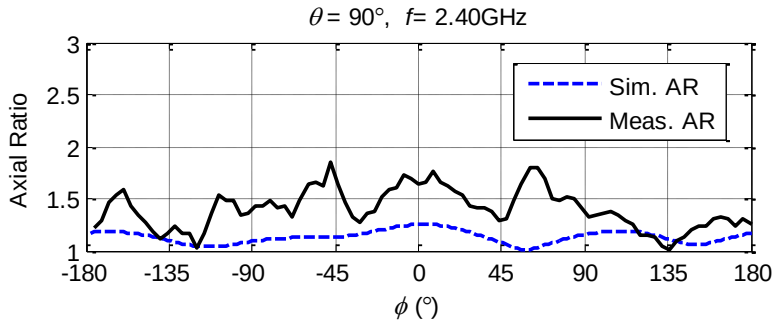

Figure 6.15. Measured and simulated antenna axial ratio on *xy*-plane.

6.6 Conclusion

In this Chapter, a circularly polarized antenna radiating omni-directionally on azimuthal plane is designed and fabricated. The proposed antenna is based on planar structure and has much smaller volume compared to existing omnidirectional CP antenna designs. Two linear omnidirectional antennas are designed and combined together to form the CP antenna, along with a microstrip line feeding network to provide necessary phase requirement. Horizontally polarized omnidirectional antenna is the most difficult part of this design. To solve the problem

while keeping low profile geometry, a novel slot antenna is designed. Different from other finite-ground-plane slot antenna, this slot antenna does not have radiation nulls at the antenna plane, which enables the antenna to have an azimuthal omnidirectional horizontal polarization. To make the difference, a parallel plate waveguide phase shifter is inserted between two ground planes. Two slots are opened on two ground planes, and are connected through the phase shifter. This novel slot antenna is then combined with a PIFA pair, which has a vertically polarized omnidirectional pattern on the same azimuthal plane. With a feeding network, the proposed antenna can achieve a good omnidirectional RHCP pattern at 2.4 GHz with simulated axial ratio less than 1.3. The fabrication verified the design with a good agreement.

CHAPTER VII

Conclusion and Future Work

In this chapter, the contributions of this dissertation are summarized. Ideas for future work are suggested as well.

7.1 Conclusion

In the thesis, we have discussed a number of topics on radar remote sensing for mapping the extent of sub-surface hydraulic fracture and monitoring lake ice. These topics relate to areas of radar system design, antenna design and scattering phenomenology.

Sub-surface hydraulic fracture imaging system: Building an imaging system for detecting the extent of hydraulic fractures in oil fields is a very challenging task due to the long penetration range requirement. We have proposed a medium frequency band (2MHz) system to take advantage of the low propagation loss at that frequency. Two approaches have been presented in the thesis:

The cross-hole system is using CW signal. With focusing the synthetic TX and RX arrays simultaneously, the target on the vertical plane can be detected. Null generation technique is used to suppress the direct-link signal. The single-hole imaging system takes a series of stepped frequency continuous wave measurements. A time-gating process is applied to filter out the direct-link signal in the time-domain. Both setups are tested with point target, cylindrical model

and fracture model at a distance of one kilometer. The outline of the model shapes have been detected clearly in the mapping results with a resolution about one wavelength.

Borehole antenna: For the proposed imaging system, a super-miniaturized borehole antenna working at MF band with the dimensions 98 mm × 98 mm × 4100 mm has been designed. The antenna shows a good efficiency of 10~50% but only provides a narrow bandwidth of about 1 kHz. To combat this limitation, a feed network is designed not only to match the antenna input impedance to a 50Ω port but also to enable frequency tunability in the range of 1.6 MHz to 2.8 MHz with a minimum gain of -25 dB.

Lake ice scattering phenomenology: To study the lake ice scattering mechanism, a full-wave simulation model has been developed. With this tool the contributions from rough ice/water interface and the columnar bubbles in the ice are analyzed. The results reveal that for the most scenarios for Arctic lake ice, columnar bubbles contribute about -16dB to backscattering coefficients which is much lower than the backscattering from rough ice/water interface.

Miniaturized Planar Antenna: A two-layer overlapped mushroom-like reactive impedance surface is studied in the thesis and is used for designing a miniaturized patch antenna with very small overall volume. The surface impedance and the wave propagation characteristics of the proposed RIS are carefully analyzed. Subsequently, a topology optimized patch antenna is placed atop the RIS substrate. The resulting patch antenna is shown to have a very small volume ($\lambda_0/11.4 \times \lambda_0/11.4 \times \lambda_0/74$). Compared to existing planar antennas with similar dimensions, the proposed antenna achieves a remarkable efficiency.

Azimuthal Omnidirectional CP antenna: In this design, a horizontally polarized omnidirectional antenna has been proposed firstly. This antenna is based on a conventional slot

antenna, which initially has radiation nulls at the antenna plane. To improve the azimuthal plane radiation pattern, a parallel plate waveguide phase shifter has been inserted between two sides of a thick ground plane. With two slots opened on both sides, this novel slot antenna has achieved an azimuthal omnidirectional pattern. This h-pol antenna is then combined with a PIFA pair, while the latter antenna has a vertically polarized omnidirectional pattern on the same azimuthal plane. With a microstrip line feeding network, the proposed antenna has achieved a good omnidirectional RHCP pattern at 2.4 GHz with simulated axial ratio less than 1.3, gain of 1dB on the entire azimuthal plane.

7.2 Future Work

Sub-surface hydraulic fracture imaging system: In the proposed cross-hole imaging system, we have not taken advantage of the tunable frequency bandwidth in the mapping process. With additional information from frequency domain, and adopting diffraction tomographic algorithm, an improvement on reconstruction resolution can be expected [149]-[154].

Surface-to-borehole setup is another system configuration to implement the imaging system. With using a large 2D antenna array (actual array or synthetic array), a 3D reconstruction mapping result can be obtained. The miniaturized planar antenna has already designed for this proposal.

Borehole antenna: The following steps for the borehole antenna design can be the fabrication of a prototype and its measurements. However, considering most antenna measurement techniques cannot be used at MF band, some special methods have to be developed.

Lake ice scattering phenomenology: Using the proposed simulation model, more objects can be included in the simulation, such as spherical bubbles, snow ice, frazil ice and so on, so that a more thorough analysis can be made.

Miniaturized planar antenna: Besides the patch antenna designed in this thesis, other antennas can be also miniaturized by the proposed RIS substrate. Especially, the RIS substrate has shown the ability to preserve the radiation pattern and the polarization purity of a planar antenna when it is used to achieve a large miniaturization factor. Thus, the proposed RIS substrate can be also used to reduce the size of a dual-polarized antenna or a planar CP antenna.

Azimuthal Omnidirectional CP antenna: The proposed antenna in this thesis is an RHCP antenna. If the feeding network is flipped with respect to the symmetry axis, it will become a LHCP antenna. Furthermore, if we place RHCP and LHCP feeding networks on the two sides of the antenna, respectively, this antenna can be designed to be a dual-polarized CP antenna. Due to the orthogonality, two polarizations should have a good port isolation.

APPENDIX A

Dual Polarized Antenna for Base Station Application

In this appendix, a wideband antenna with ground plane backing is presented. This is antenna is designed for multi-band base-stations applications optimizing for improving the frequency re-use and optimize the channel capacity.

A.1 Introduction

The performance of an antenna is affected by many basic parameters, such as bandwidth, input impedance, polarization, radiation patterns, and gain. Following some important characteristics for base station antenna are introduced.

The impedance match is an important characteristic in antenna design. The standing wave ratio (SWR) is defined as the ratio of maximum power to minimum power in wave in the feed line. According to that, an SWR of 1:1 is ideal, an SWR of 1.5 is always required. As for bandwidth, 1710-2170 MHz is a common frequency band in mobile radio application, which combines 1800 MHz, 1900 MHz and 2100 MHz bands.

The polarization of an antenna is the orientation of radiated electric field with respect to the Earth's surface and is determined by the structure of the antenna. Because the handset users usually hold their devices at a large angle to the vertical, between mouth and ear of a standing or seated user, typically about $45°$. Dual slant-polarized antenna with $\pm 45°$ linear polarization is now in almost universal use for polarization diversity systems. Most dual-polar antennas are required to have a high degree of cross-polar discrimination (XPD) and cross-polar isolation

(XPI) so each port receives power only from the designated polarization. In this configuration, the XPD is required to reach 25dB at boresight direction and 10 dB at 60° direction. The XPI is at least 30dB.

Radiation patterns are graphical representations of the radiated power distribution in free space. The azimuth beamwidth is determined by the design of the radiating element, together with its relationship to the reflecting surface behind it. By the requirement of communication system, the azimuth beamwidth is usually specified within a tight limitation, typically 65°±5° over the whole band. Antenna gain is a function of both the azimuth beamwidth and antenna array's electrical length in the vertical plane. Since the azimuth beamwidth is selected by the requirement of the frequency re-use plan, we usually achieve a high gain by increasing the vertical length of the antenna array. However, the maximum vertical length is limited by either the physical size or the minimum acceptable vertical beamwidth. Besides, as the antenna length increases, the attenuation of the feed network will also increase. Thus it is not easy to boost the gain during the design process.

Some wideband dual polarized antennas have been presented in the literature, such Vivaldi antennas [155]. However, Vivaldi antennas are traveling wave antennas and are required to be relatively long to achieve good directivity and front-to-back ratios which makes their size relatively large at low frequency systems. To address the wideband antenna size problem for the considered applications, a compact wideband antenna employing a coupled sectorial loop inside a rectangular cavity has been reported by the University of Michigan [156]. This antenna provided very wide operating bandwidth and desirable radiation characteristics. However, this design was a single polarization design. In this project we employ similar concept but the

radiating element is a dual polarized radiating element similar to the one presented in [157] which allows the excitation of the two orthogonal degenerate modes of the cavity thus enabling dual polarization application. The antenna structure offers geometric orthogonality between the two polarizations which results in high isolation between the two polarizations.

The antenna is placed in front of a metallic ground plane with a beamwidth of 65 ° and a compact size ($0.38\lambda_m \times 0.38\lambda_m \times 0.25\lambda_m$). The antenna structure and design will be presented in the following sections.

A.2 Antenna Structure

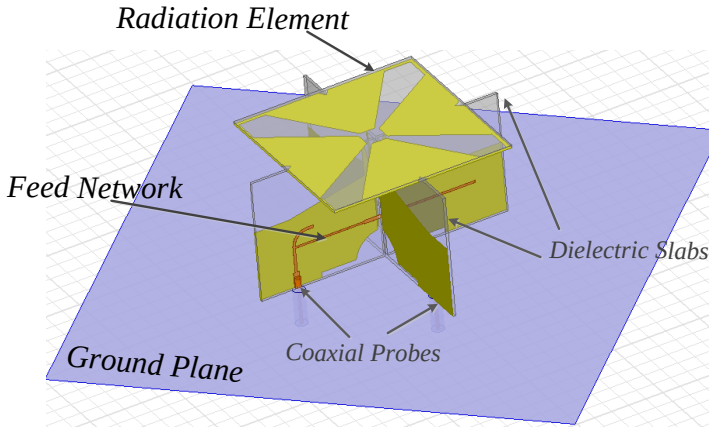

Figure A.1. The structure of the ground-plane-backed-CSLA.

The proposed antenna is shown in the Figure A.1. The radiating element consists of two orthogonal coupled sectorial loops antennas (OCSLA). Each sectorial loop is composed of two opposite triangular patches and a rectangular ring around the outside, with the two rings overlapping and eventually becoming a shared ring. To illustrate the operation of the antenna, the excitation is modeled using two ideal voltage gap sources as shown in Figure A.2 (a). The current distribution on the OCSLA is shown in Figure A.2 (b) for the vertical excitation. The horizontal polarization can be obtained by a simple 90-degree-rotation due to the geometrical

symmetry with respect to the ports. From the current distribution on Figure A.2 (b), we can see that all the vertical currents are in the same direction thus enhancing the vertical polarization radiation whereas all the horizontal currents are opposite to each other thus cancelling the horizontal radiation along the principal planes. The opposite is true for the horizontal excitation. It is interesting to note the geometric orthogonality between the two modes which ensures high isolation between the two ports. This is very important in most dual polarized applications.

Two vertical dielectric slabs are used to support the radiation element at a certain height *H* above the ground plane. A microstrip to slotline balun is printed on each slab to excite the two orthogonal modes as shown in Figure A.3.

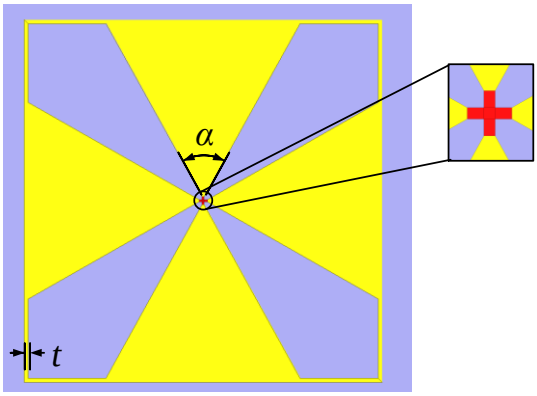

(a)

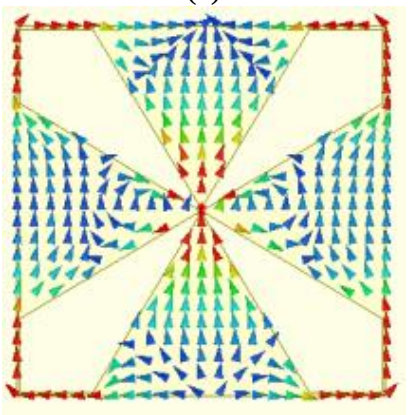

(b)

Figure A.2. (a) The structure of dual-polarized radiating element and (b) the current distribution for vertical polarization.

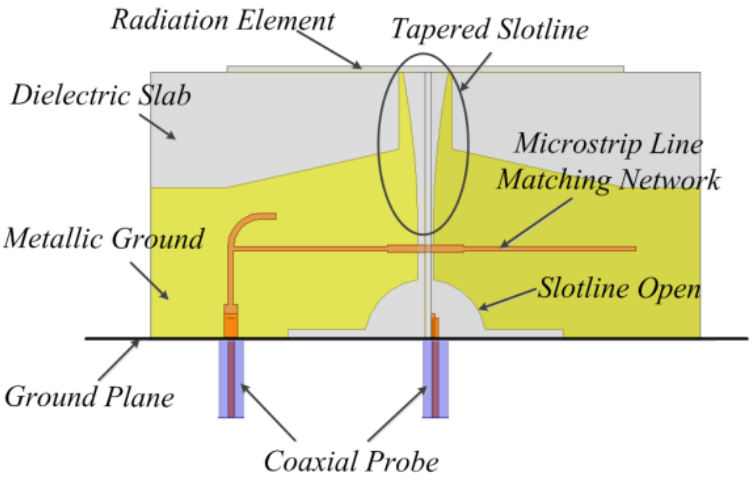

Figure A.3. Feeding network design using microstrip/ slotline transition for the ground-plane-backed antenna.

A.3 Radiation Element Parametric Study

The OCSLA dimensions are modified to work over the desired 1710 - 2170 MHz frequency band for mobile base stations. As will be shown in later, the input impedance of the antenna will be matched using a multi-section microstrip line. To study the effect of the different parameters on the antenna in a manner that is independent of the characteristic impedance of the feed line, the port impedance used to calculate the input reflection coefficient was chosen for each individual case to minimize the average VSWR within the band 1710 - 2170 MHz. This real-number frequency-independent characteristic impedance is the value that should be used in the impedance matching network design and is written in parenthesis in the legend of each figure in this section. The VSWR in this case will be referred to as the Minimum Achievable VSWR (MA-VSWR). In other words, MA-VSWR uses a certain real port impedance for which the antenna VSWR is minimal over the widest bandwidth.

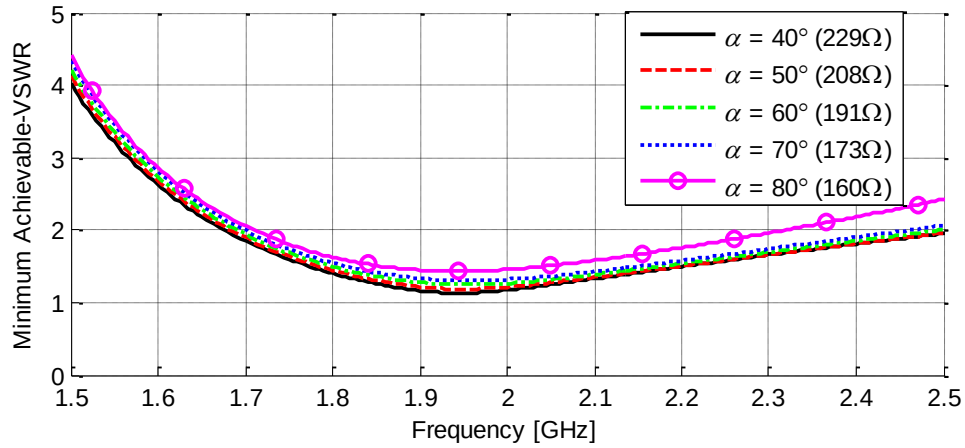

(a)

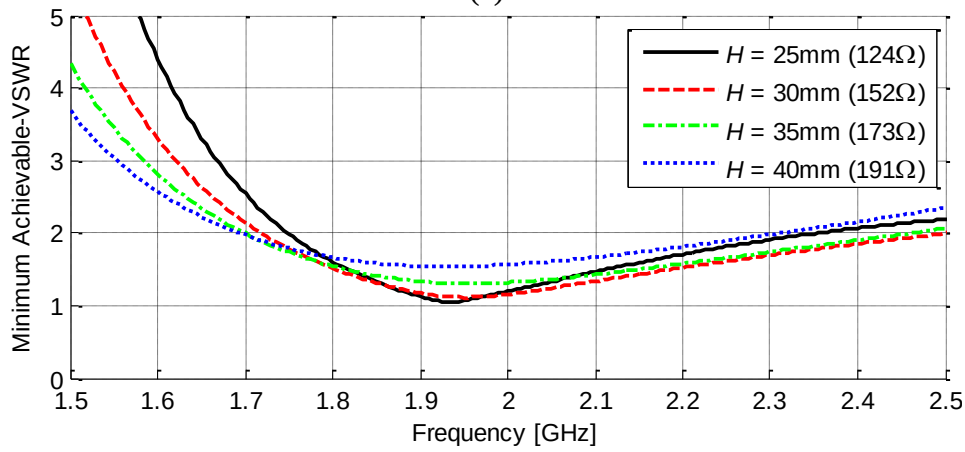

(b)

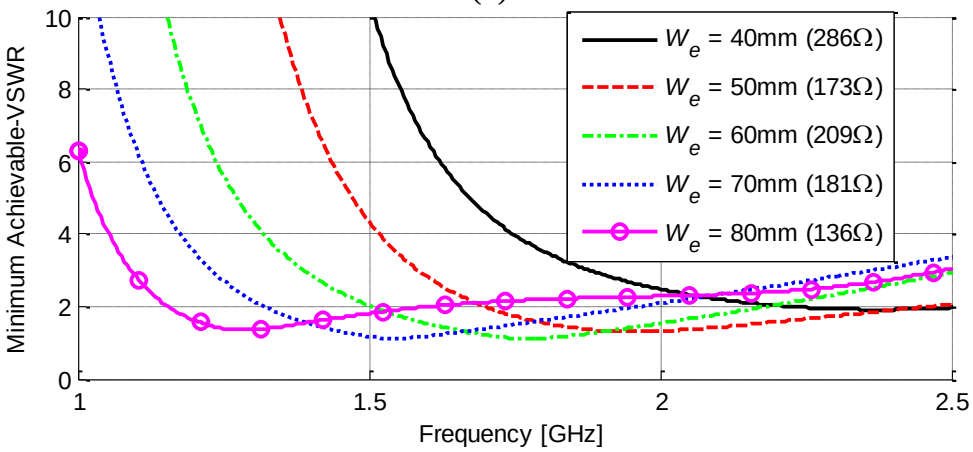

(c)

Figure A.4. Effect of (a) angle between the two sectorial loops, α, (b) Antenna Height H, and (c) Antenna width W_e on the minimum achievable VSWR (MA-VSWR) for the ground-plane-backed antenna. The optimized input impedance to achieve MA-VSWR is marked in the parentheses in the legend of each figure.

The effects of the different antenna dimensions on the input matching are shown in Figure A.4 (a) – (c). The angle between the two sectorial loops, α, mainly controls the input impedance of the radiation element similar to the cavity backed design as shown in Figure A.4(a). The effect of the radiating element height above the ground plane, H, is shown in the Figure A.4 (b). As H increases, the bandwidth slightly improves, but the matching becomes worse within the desired band. This is due the OCSLA being a resonant element and its height above the ground plane has to be close to quarter of the wavelength (~39mm) in order to ensure constructive interference between the direct ray and the reflected ray from the ground plane. Similarly, at a fixed H, the radiating element width, W_e has to be close to the resonance width as shown in Figure A.4 (c). Increasing W_e reduces the intrinsic resonance of the element allowing it to operate at lower frequencies but the destructive interference from the back ground plane negatively impacts the matching.

A.4 Feeding Network Design

The microstrip to slot line transition employs a microstrip line crossing the slot line that feeds the antenna from one end and short-circuited at a proper distance and configuration from the other end. The microstrip line is connected to a coaxial feed and includes each matching circuit segments as shown in Figure A.1 and Figure A.3. The slot lines and the microstrip lines are printed on two opposite sides of two perpendicular substrates which also support the upper radiating element at a certain height with a good mechanical stability. The electric field in one slot line is perpendicular to that in the other slot line, thus the two slot lines will not couple to each other.

To get wideband impedance matching, a tapered slot-line and a multi-section microstrip line are used as shown in Figure A.3. Since the radiation element has an input impedance of around 170Ω according to the parametric studies, the upper end of the slotline should have higher characteristic impedance. The slotline impedance is increased by gradually increasing the slot width and reducing the ground plane width [158]. In order to minimize the vertical ground plane's disturbance to the radiation element's near field distribution, the vertical ground planes are partially cut near the radiating elements. The final antenna dimensions are: α = 70 °, W_e = 50 mm, and H = 35 mm resulting in a 71 mm × 71 mm × 35 mm overall antenna dimension.

A.5 Measurement Results

The base station antenna is fabricated on a 1.52 mm RO4003C substrate for both the radiating structure and the feed, as shown in Figure A.5. The measured return loss values at the two ports are shown in Figure A.6 (a) and (b). The measured results show good agreement with the simulations with both S_{11} and S_{22} less than -14 dB over 1.71-2.17 GHz. The measured isolation between the two ports is less than -34 dB over the same band as shown in Figure A.6 (c). The small discrepancy between the measured and simulated results is due to the manual fabrication of the antenna which affects the fabrication tolerances.

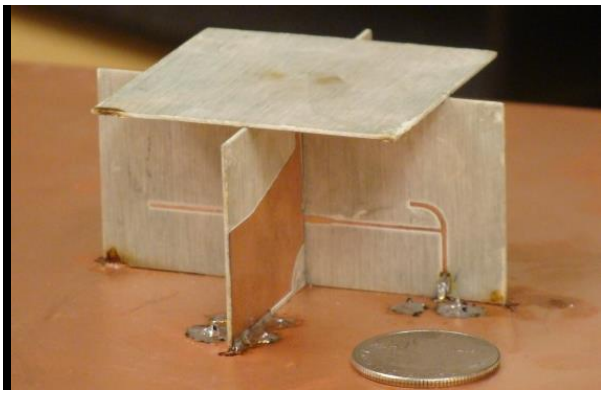

Figure A.5. The fabricated ground-plane-backed-CSLA base station antenna.

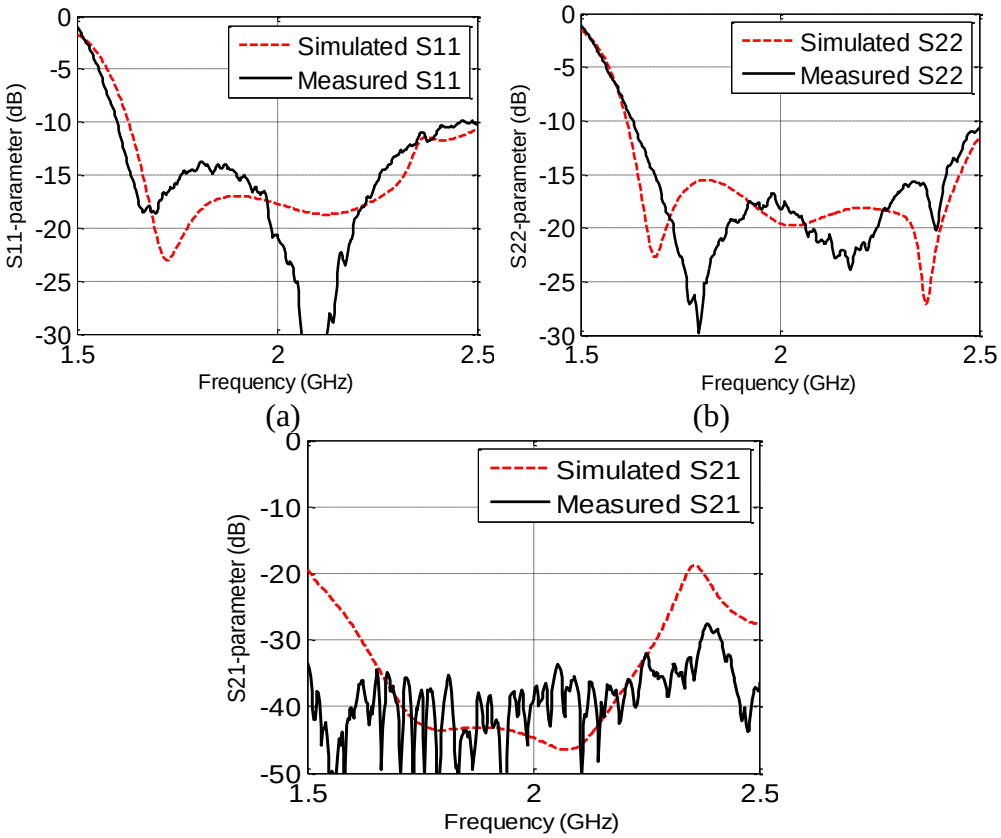

Figure A.6. The HFSS simulated results (dash line) and measured results (solid) for (a) S11, (b) S22 and (c) S21 of the ground-plane-backed antenna.

The measured co-pol and cross-pol radiation patterns at three different frequencies are shown in Figure A.7 (a)-(c). The antenna gain is 8 dBi and relatively constant over the operating band and the beamwidth is approximately 70°. The cross polarization discrimination (XPD) is below 28 dB at the low frequency band and increases to 23 dB at 2.1 GHz. The front-to-back ratio is about 20 dB at lowest frequency when using a 130 mm × 130 mm ground plane.

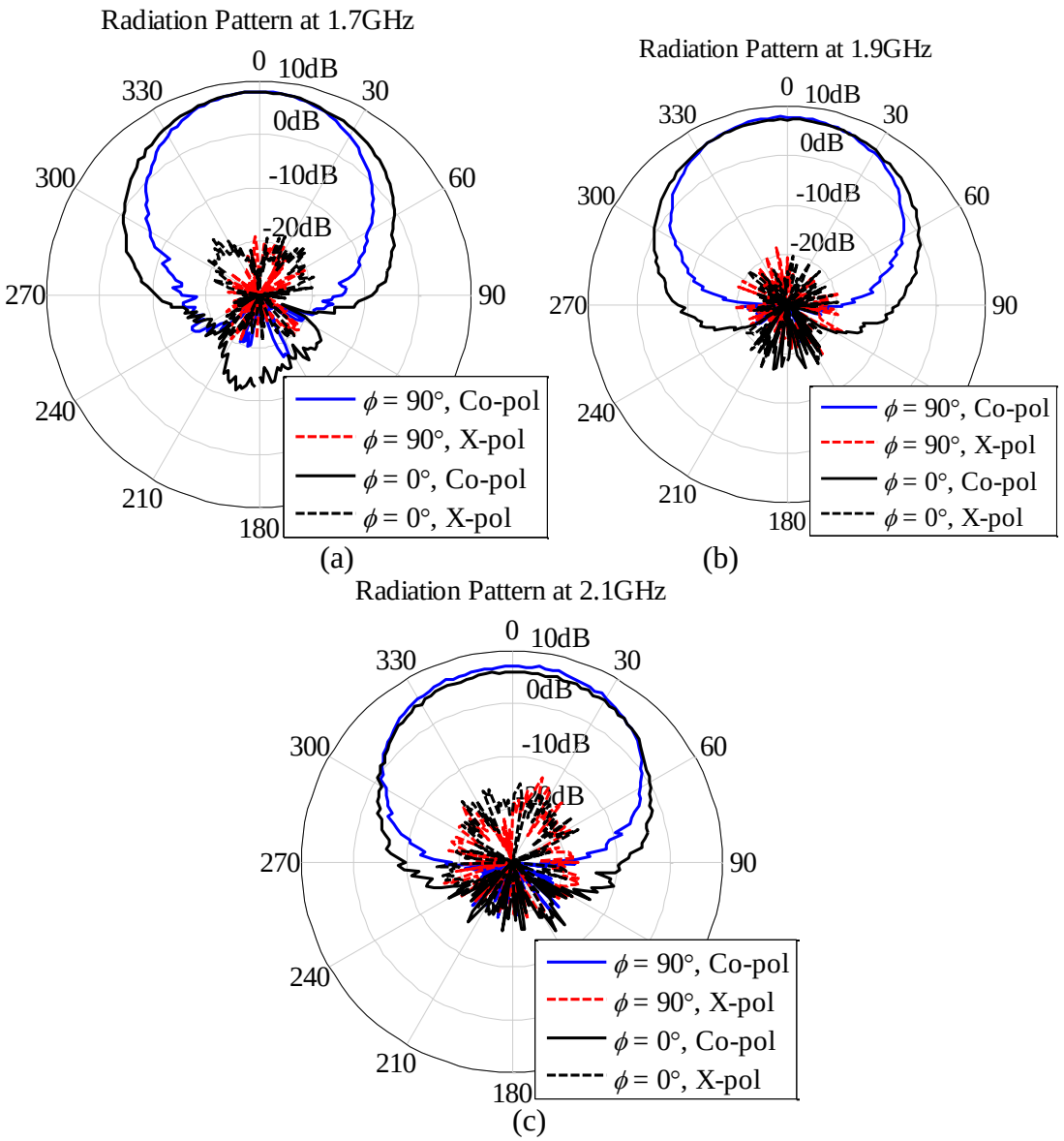

Figure A.7. The radiation patterns of the ground-plane-backed antenna measured in the anechoic chamber (a) at 1.7 GHz, (b) at 1.9 GHz and (c) at 2.1 GHz.

A.6 Conclusion

A new dual polarized driving element for design of wideband antennas is presented. The driving element consists of two orthogonal coupled sectorial loops which can be placed over a ground plane to achieve directional radiation. A parametric study of the antenna structure is presented to further investigate the operation of the antenna and determine the impact of the

different parameters. The OCSLA was used as a stand-alone radiating element by placing it on top of a metallic ground plane for mobile base station applications. To achieve optimum matching, it is shown that the OCSLA has to be placed about quarter of a wavelength above the ground plane at its intrinsic resonance frequency. The base station design is fed using orthogonal microstrip to slot line baluns for operation over 1.71 GHz to 2.17 GHz. The measurement results showed return loss better than 14 dB and input ports isolation better than 34 dB. The measured gain is above 8 dBi over the band with the corresponding beamwidth of 65^{o} to 70^{o}. The measured cross polarization discrimination is less than -23 dB at boresight and -17 dB at $\pm 60^{\circ}$ directions.

BIBLIOGRAPHY

[1] Pro Publica, “What Is Hydraulic Fracturing?”, https://www.propublica.org/special/hydraulic-fracturing-national.

[2] C. Boyer, J. Kieschnick, R. Suarez-Rivera, R. E. Lewis, and G. Waters, "Producing gas from its source," *Oilfield Review*, vol. 18, no. 3, pp.36-49, 2006.

[3] Frank R. Spellman, *Environmental Impacts of Hydraulic Fracturing*, CRC Press, 2012.

[4] J. C. Minne, J. Gartner, "Fracture Detection in the Middle East," *Middle East Technical Conference and Exhibition*, 1979.

[5] Ground Water Protection Council; ALL Consulting (April 2009), “Modern Shale Gas Development in the United States: A Primer (Report),” *DOE Office of Fossil Energy and National Energy Technology Laboratory*, pp. 56–66. Retrieved 24 February 2012.

[6] Dean V. Power, et al. "Detection of hydraulic fracture orientation and dimensions in cased wells," *Journal of Petroleum Technology*, vol. 28, no. 09, pp. 1-116, 1976.

[7] N. R. Warpinski, et al. "Mapping hydraulic fracture growth and geometry using microseismic events detected by a wireline retrievable accelerometer array," *SPE Gas Technology Symposium*. Society of Petroleum Engineers, 1998.

[8] James E. Uhl, et al. "Microseismic fracture mapping using seismic source timing measurements for velocity calibration," *U.S. Patent*, No. 7,660,194, 9 Feb. 2010.

[9] S. Ebihara, Y. Wada, "Investigation of wideband Coaxial-Fed Circular dipole Array antenna in a Borehole," *Advanced Ground Penetrating Radar (IWAGPR), 2011 6th International Workshop on*, pp.1-5, 22-24, June 2011.

[10] Sixin Liu, Zhaofa Zeng, M. Sato, "Subsurface water-filled fracture detection by borehole radar: a case history," *2005 IEEE International Geoscience and Remote Sensing Symposium(IGARSS '05) Proceedings*, 25-29 July 2005.

[11] Hong-Yan Liang, Hong-Chun Yang, Jing Hou; Ling-Yun Cai, "A Compact Ferrite-Based Dipole Directional Antenna for Borehole Radar Application," *Geoscience and Remote Sensing Letters, IEEE*, vol.10, no.3, pp.486-489, May 2013.

[12] F. Sagnard, F. Rejiba, M. Froumentin, "Design and analysis of wideband antennas for borehole and surface ground penetrating radars: Application to soil moisture content measurements," *Antennas and Propagation Society International Symposium (APSURSI), 2010 IEEE*, pp.1-4, 11-17 July 2010.

[13] T. Takayama, M. Sato, "A Novel Direction-Finding Algorithm for Directional Borehole Radar," *IEEE Transactions on Geoscience and Remote Sensing*, vol.45, no.8, pp.2520-2528, Aug. 2007.

[14] T. Miwa, M. Sato, H. Niitsuma, "Enhancement of reflected waves in single-hole polarimetric borehole radar measurement," *IEEE Transactions on Antennas and Propagation*, vol.48, no.9, pp.1430-1437, Sep 2000.

[15] M. Shahidi, J. B. Hasted, and A. K. Jonscher. "Electrical properties of dry and humid sand." *Nature*, vol.258, no. 5536, pp. 595-597, 1975.

[16] A. P. Annan, "GPR−History, trends, and future developments," *Subsurface Sens. Technol. Appl.*, vol. 3, no. 4, pp. 253‑270, Oct. 2002.

[17] B. K. Sternberg and J. W. McGill, "Archaeology studies in southern Arizona using ground penetrating radar," *J. Appl. Geophys.*, vol. 33, no. 1–3, pp. 209–225, 1995.

[18] C. Maierhofer, "Nondestructive evaluation of concrete infrastructure with ground penetrating radar," *J. Mater. Civil Engrg.*, vol. 15, no. 3, pp. 287–297, 2003.

[19] M. Sato and T. Takayama, "High range resolution directional borehole radar for 3D fracture delineation," *Proc. IEEE Int. Geoscience and Remote Sensing Symp.*, pp. 132–135, 2009.

[20] Mei Yang, Xiaoxing Yin, Hongxin Zhao, Shunli Li, Li Xie, "Resistive loading between the antenna array elements," *2014 3rd Asia-Pacific Conference on Antennas and Propagation (APCAP)*, pp.222-224, 26-29 July 2014.

[21] Evert Slob, Motoyuki Sato, and Gary Olhoeft. "Surface and borehole ground-penetrating-radar developments." *Geophysics* vol. 75, No.5, pp. 75A103-75A120, 2010.

[22] Richard Johnson and Henry Jasik, *Antenna Engineering Handbook*, McGraw-Hill, 2nd edition, 1984.

[23] L. Mattioni and G. Marrocco, "Design of a Broadband HF Antenna for Multimode Naval Communications, " *IEEE Antennas and Wireless Propagation Letters*, vol. 4, pp. 179-182, 2005.

[24] Z. Zhang, H. Xie, L. Zheng, and Q. Wang, "A Novel HF Fishbone Antenna with Vee-Element," *IEEE International Conference on Communications Technology and Applications (ICCTA'09)*, pp. 733-737, 2009.

[25] E. B. Joffe, "A Large Flat Biconical Antenna for LLSC Aircraft-Illumination in the HF band," *IEEE International Symposium on Electromagnetic Compatibility*, pp. 465-468, 1996.

[26] Z. Zhigang, X. Hui, Z. Longgen, and Z. Yongyu, "HF compound antennas consisting of a horizontal LPDA and a vertical mono-cone antenna," *2009 3rd IEEE International Symposium on Microwave, Antenna, Propagation and EMC Technologies for Wireless Communications*, pp. 687-689, 2009.

[27] V. L. Dorohov, V. T. Rozumenko, V. G. Somov, O. F. Tyrnov, "Upgrades to the Kharkiv V. N. Karazin National University MF radar antenna," *2013 IX International Conference on Antenna Theory and Techniques (ICATT)*, pp.370-372, 16-20 Sept. 2013.

[28] J. Y. Des, "Electrically small plate antenna that operates at HF," *2005 IEEE Antennas and Propagation Society International Symposium*, vol.1B, pp.15-16, 3-8 July 2005.

[29] Hong-Kyun Ryu, Gichul Jung, Jong-Myung Woo, "A small quarter wavelength microstrip antenna for HF and VHF band applications," *2010 Mediterranean Microwave Symposium (MMS)*, pp.48-51, 25-27 Aug. 2010.

[30] S. Kawdungta, C. Phongcharoenpanich, D. Torrungrueng, "Design of flat spiral rectangular loop gate antenna for HF-RFID systems," *Asia-Pacific Microwave Conference (APMC 2008)*, pp.1-4, 16-20 Dec. 2008.

[31] Jungsuek Oh, Jihun Choi, F. T. Dagefu, K. Sarabandi, "Extremely Small Two-Element Monopole Antenna for HF Band Applications," *IEEE Transactions on Antennas and Propagation*, vol.61, no.6, pp.2991-2999, June 2013.

[32] Jihun Choi; K. Sarabandi, "An extremely low-profile MF monopole antenna design and measurement," *2013 USNC-URSI Radio Science Meeting (Joint with AP-S Symposium)*, pp.121-121, 7-13 July 2013.

[33] J. Baker, Hyoung-sun Youn, N. Celik, M. F. Iskander, "Low-Profile Multifrequency HF Antenna Design for Coastal Radar Applications," *IEEE Antennas and Wireless Propagation Letters*, vol.9, no., pp.1119-1122, 2010.

[34] S. Abdullah, S. I. S. Hassan, "Design small size of High Frequency (HF) helical antenna," *5th International Colloquium on Signal Processing & Its Applications (CSPA 2009)*, pp.259-262, 6-8 March 2009.

[35] S. Ebihara, Y. Kimura, T. Shimomura, R. Uchimura, H. Choshi, "Coaxial-Fed Circular Dipole Array Antenna With Ferrite Loading for Thin Directional Borehole Radar Sonde," *IEEE Transactions on Geoscience and Remote Sensing*, vol.53, no.4, pp.1842-1854, April 2015.

[36] S. Pinhas, S. Shtrikman, "Comparison between computed and measured bandwidth of quarter-wave microstrip radiators," *IEEE Transactions on Antennas and Propagation*, vol.36, no.11, pp.1615-1616, Nov 1988.

[37] K. Hirasawa and M. Haneishi, *Analysis, Design, and Measurement of Small and Low-Profile Antennas*, Artech House, 1992.

[38] Rod Waterhouse, "Small microstrip patch antenna," *Electronics Letters*, vol.31, no.8, pp.604-605, 13 Apr 1995.

[39] T. K. Lo, Chun-On Ho; Y. Hwang, E. K. W. Lam, B. Lee, "Miniature aperture-coupled microstrip antenna of very high permittivity," *Electronics Letters* , vol.33, no.1, pp.9-10, 2 Jan 1997.

[40] K.F. Lee, K.M. Luk, *Microstrip Patch Antennas*, Imperial College Press, 2011.

[41] K.M. Luk, R. Chair, K. F. Lee, "Small rectangular patch antenna," *Electronics Letters* , vol.34, no.25, pp.2366-2367, 10 Dec 1998.

[42] Kin-Lu Wong, Kai-Ping Yang, "Small dual-frequency microstrip antenna with cross slot," *Electronics Letters* , vol.33, no.23, pp.1916-1917, 6 Nov 1997.

[43] K. F. Lee, K. M. Luk, K. F. Tong, Y. L. Yung, T. Huynh, "Experimental study of the rectangular patch with a U-shaped slot ," *Antennas and Propagation Society International Symposium*, 1996. AP-S. Digest , pp.10-13, 21-26 Jul 1996.

[44] H. Nakano, K. Vichien, "Dual-frequency square patch antenna with rectangular notch," *Electronics Letters*, vol.25, no.16, pp.1067-1068, 3 Aug. 1989.

[45] J. S. Kula, D. Psychoudakis, W.-J. Liao, C.-C. Chen, J. L. Volakis, J. W. Halloran, "Patch-antenna miniaturization using recently available ceramic substrates," *Antennas and Propagation Magazine*, IEEE , vol.48, no.6, pp.13-20, Dec. 2006.

[46] A. Alú, F. Bilotti, H. Engheta, L. Vegni, "Subwavelength, Compact, Resonant Patch Antennas Loaded with Metamaterials," *IEEE Trans. Antennas Propag*., vol. 55, pp. 13-25, 2007.

[47] F. Bilotti, A. Alú, L. Vegni, "Design of Miniaturized Metamaterial Patch Antennas with Mu-Negative Loading," *IEEE Trans. Antennas Propag*., vol. 56, pp. 1640-1647, 2008.

[48] D. Strickland, J. Pruitt, J. Helffrich, E. Martinez, B. Nance, L. Griffith, "Realization of Electrically Small Patch Antennas Loaded with Metamaterials," *Proc.Materials Research Society (MRS) Fall Meeting 2009*, Boston, MA, 2009.

[49] J. Pruitt, D. Strickland, "Experimental exploration of metamaterial substrate design for an electrically small patch-like antenna," *Antennas and Propagation Society International Symposium (APSURSI), 2010 IEEE* , 11-17 July 2010.

[50] S. Jahani, J. Rashed-Mohassel, M. Shahabadi, "Miniaturization of Circular Patch Antennas Using MNG Metamaterials," *IEEE Antennas and Wireless Propagation Letters*, vol.9, pp.1194 - 1196, 2010.

[51] K. Buell, H. Mosallaei, and K. Sarabandi, "A substrate for small patch antennas providing tunable miniaturization factor," *IEEE Trans. Microwave Theory Tech.*, vol. 54, no. 1, pp. 135–146, Jan. 2006.

[52] J. M. Fernández, J. L. Masa-Campos, and M. Sierra-Pérez, "Circularly polarized omnidirectional millimeter wave monopole with parasitic strip elements," *Microw. Opt. Technol. Lett.*, vol. 49, pp. 664–668, 2007.

[53] John D. Kraus, and Ronald J. Marhefka, *Antenna for all applications*, Upper Saddle River, NJ: McGraw Hill, 2002.

[54] Fu-Ren Hsiao; Kin-Lu Wong, "Omnidirectional planar folded dipole antenna," *IEEE Transactions on Antennas and Propagation*, vol.52, no.7, pp.1898-1902, July 2004.

[55] R. Bancroft, B. Bateman, "An omnidirectional planar microstrip antenna," *IEEE Transactions on Antennas and Propagation*, vol.52, no.11, pp.3151-3154, Nov. 2004.

[56] Ezzeldin Soliman, Magdy S. Ibrahim, and Alaa K. Abdelmageed, "Dual-polarized omnidirectional planar slot antenna for WLAN applications," *IEEE Transactions on Antennas and Propagation*, vol. 53, no. 9, 3093-3097, 2005.

[57] Byung-Chul Park, and Jeong-Hae Lee, "Omnidirectional circularly polarized antenna utilizing zeroth-order resonance of epsilon negative transmission line," *IEEE Transactions on Antennas and Propagation*, vol. 59, no. 7, 2717-2721, 2011.

[58] Dakui Wu, et al. "A 5.8-GHz omnidirectional horizontal radiation pattern antenna for wireless communication system." *IEEE International Conference on Communications, Circuits and Systems (ICCCAS)*, 2007.

[59] Alejandro Lucas Borja, et al. "Omnidirectional loop antenna with left-handed loading." *IEEE Antennas and Wireless Propagation Letters*, no. 6, pp. 495-498, 2007.

[60] C-C. Lin, L-C. Kuo, and H-R. Chuang. "A horizontally polarized omnidirectional printed antenna for WLAN applications." *IEEE Transactions on Antennas and Propagation*, vol. 54, no. 11, pp. 3551-3556, 2006

[61] Chi-Hyung Ahn, Seong-Won Oh, and Kai Chang. "A dual-frequency omnidirectional antenna for polarization diversity of MIMO and wireless communication applications." *IEEE Antennas and Wireless Propagation Letters*, no. 8, pp. 966-969, 2009.

[62] Yue Li, et al. "Compact azimuthal omnidirectional dual-polarized antenna using highly isolated colocated slots." *IEEE Transactions on Antennas and Propagation*, vol. 60, no. 9, pp. 4037-4045, 2012.

[63] Dino Giuli, "Polarization diversity in radars," *Proceedings of the IEEE,* vol. 74, no.2, pp. 245-269, 1986.

[64] M. English, B. Kochtubajda, F. D. Barlow, A. R. Holt, and R. McGuinness, "Radar measurements of rainfall by differential propagation phase: A pilot experiment," *Atmosphere-Ocean,* vol. 29, no.2, pp. 357-380, 1991.

[65] Y. M. M. Antar, A. Hendry, and G. C. McCormick, "Circular polarization for remote sensing of precipitation Polarization diversity work at the National Research Council of Canada," *IEEE Antennas Propag. Mag*., vol. 34, pp. 7-16, 1992.

[66] D. Lerner, "A wave polarization converter for circular polarization," *IEEE Transactions on Antennas and Propagation*, vol.13, no.1, pp.3-7, Jan 1965.

[67] Doris L. Wu, "Omnidirectional circularly-polarized conformal microstrip array for telemetry applications." *IEEE Antennas and Propagation Society International Symposium AP-S. Digest*. vol. 2, 1995.

[68] Yadong Xu, and Chengli Ruan, "A novel design of circularly polarized omni-directional antenna for Ka band." *IEEE Global Symposium on Millimeter Waves (GSMM),* 2008.

[69] XuLin Quan; RongLin Li; M. M. Tentzeris, "A novel broadband omni-directional circularly polarized antenna for mobile communications," *2011 IEEE International Symposium on Antennas and Propagation (APSURSI)*, pp.1777-1779, 3-8 July 2011.

[70] F.-R. Hsiao, and K.-L. Wong, "Low-profile omnidirectional circularly polarized antenna for WLAN access points," *Microw. Opt. Technol. Lett.*, vol. 46, pp. 227–231, 2005.

[71] A. Narbudowicz, Xiu Long Bao; M. J. Ammann, "Dual-Band Omnidirectional Circularly Polarized Antenna," *IEEE Transactions on Antennas and Propagation,* vol.61, no.1, pp.77-83, Jan. 2013.

[72] H. Iwasaki, N. Chiba, "Circularly polarised back-to-back microstrip antenna with an omnidirectional pattern," *IEE Proceedings in Microwaves, Antennas and Propagation*, vol.146, no.4, pp.277-281, Aug 1999.

[73] D. K. Atwood, G. E. Gunn, C. Roussi, Jiangfeng Wu; C. Duguay, K. Sarabandi, "Microwave Backscatter From Arctic Lake Ice and Polarimetric Implications," *IEEE Transactions on Geoscience and Remote Sensing*, vol.53, no.11, pp.5972-5982, Nov. 2015.

[74] Yunqiang Yang; A. E. Fathy, "Development and Implementation of a Real-Time See-Through-Wall Radar System Based on FPGA," *IEEE Transactions on Geoscience and Remote Sensing*, vol.47, no.5, pp.1270-1280, May 2009.

[75] G. Heidari, *WiMedia UWB: Technology of Choice for Wireless USB and Bluetooth*, 1st ed. Chichester, U.K.: Wiley, 2008.

[76] Chi-Chih Chen, M. B. Higgins, K. O'Neill, R. Detsch, "Ultrawide-bandwidth fully-polarimetric ground penetrating radar classification of subsurface unexploded ordnance," *IEEE Transactions on Geoscience and Remote Sensing*, vol.39, no.6, pp.1221-1230, Jun 2001.

[77] R. G. Vaughan, J. B. Andersen, "Antenna diversity in mobile communications," *IEEE Transactions on Vehicular Technology*, vol.36, no.4, pp. 149- 172, Nov 1987.

[78] A. Elsherbini, Jiangfeng Wu; K. Sarabandi, "Dual Polarized Wideband Directional Coupled Sectorial Loop Antennas for Radar and Mobile Base-Station Applications," *IEEE Transactions on Antennas and Propagation*, vol.63, no.4, pp.1505-1513, April 2015.

[79] H. Bukhari, and K. Sarabandi, "Miniaturized Omnidirectional Horizontally Polarized Antenna," *IEEE Antennas and Propagation Magazine,* vol. 63, no. 10, pp. 4280-4285, Oct. 2015.

[80] J. Wu, and K. Sarabandi, "Design and Evaluation of a Class of Miniaturized Metal-backed Antennas," *IEEE Antennas and Propagation Magazine,* vol. 56, no. 6, pp. 279-293, Dec. 2014.

[81] W. Hong, and K. Sarabandi, "Low-Profile, Multi-Element, Miniaturized Monopole Antenna," *IEEE Trans. Antennas and Propagation*, pp.72-80, vol. 57, no. 1, Jan. 2009.

[82] W. Hong, N. Behdad, and K. Sarabandi, "Size Reduction of Cavity-Backed Slot Antennas," *IEEE Transactions on Antennas and Propagation*, vol. 54, no. 5, pp. 1461-1465, May 2006.

[83] F. Dagefu, J. Oh, and K. Sarabandi, "A Sub-wavelength RF Source Tracking System for GPS-denied Environments," *IEEE Transactions on Antennas and Propagation,* pp. 2252-62, vol. 61, no. 4, April 2013.

[84] Robert L. Nowack, "Wavefronts and solutions of the eikonal equation."*Geophysical Journal International*, vol. 110, pp. 55-62, 1992.

[85] Fawwaz Tayssir Ulaby, et al. *Microwave radar and* radiometric *remote* sensing. Ann Arbor: University of Michigan Press, 2014.

[86] Olukayode D. Akinyemi, et al. "Characterization of Density and Porosity of Rocks Samples from Ogun State of Nigeria," *Earth Science Research*, vol. 1, no. 2, pp. 98, 2012.

[87] Online Source, Rock Density Table, https://rocscience.com/help/rocfall/webhelp/baggage/Rock_Density_Table.htm.

[88] Rosemary J. Knight, and Amos Nur. "The dielectric constant of sandstones, 60 kHz to 4 MHz." *Geophysics*, vol. 52, no. 5, pp. 644-654, 1987.

[89] Roger F. Harrington, *Time-harmonic electromagnetic fields*. McGraw-Hill, 1961.

[90] Michael D. Holloway, and Oliver Rudd. *Fracking: The Operations and Environmental Consequences of Hydraulic Fracturing*, Ch.9, John Wiley & Sons, 2013.

[91] USDOE, *Modern Shale Gas Development in the United States: A Primer*, U.S. Department of Energy, Washington, DC, pp. 55-59, 2009.

[92] A. Langman, M. R. Inggs, "Pulse versus stepped frequency continuous wave modulation for ground penetrating radar," *IEEE International Geoscience and Remote Sensing Symposium (IGARSS '01)*, vol.3, pp.1533,1535, 2001.

[93] T. Kido, T.; Y. Yokota, F. Kawahara, M. Sato, "Wide band stepped-frequency ground penetrating radar," *IEEE International Geoscience and Remote Sensing Symposium (IGARSS)*, pp.55-58, 24-29 July 2011.

[94] R. G. Lyons, *Understanding digital signal processing*, 3rd ed. Upper Saddle River, NJ: Prentice Hall, 2011.

[95] Dunsmore, Joel P. *Handbook of microwave component measurements: with advanced VNA techniques*, John Wiley & Sons, 2012.

[96] Trisha A. Smrecak, "Jointing and fracturing in the Marcellus Shale", *The Marcellus Papers*, Issue 5, Aug 2011.

[97] CWS Bytemark, "Material 61 Datesheet," http://www.bytemark.com/products/61material.htm.

[98] Constantine A. Balanis, *Antenna Theory: Analysis And Design*, 3rd ed., New York: Wiley, 1997, pp.162–165.

[99] C. Surdu, C. R. Duguay, L. C. Brown, and D. Fernández Prieto, "Response of ice cover on shallow Arctic lakes of the North Slope of Alaska to contemporary climate conditions (1950-2011): Radar remote sensing and numerical modeling data analysis," *The Cryosphere*, no. 8, pp. 167-180, 2014.

[100] J. C. Mellor, "J. C. Bathymetry of Alaskan arctic lakes: A key to resource inventory with remote-sensing methods," *Ph.D. dissertation, Inst. of Marine Science Alaska Univ.*, Fairbanks, AK, USA, 1982.

[101] W. F. Weeks, et al. "Differences in radar return from ice-covered North Slope Lakes." *J. Geophys. Res.: Oceans*, vol. 83. C8, pp. 4069-4073, 1978.

[102] P. Sellmann, W. F. Weeks, and W. J. Campbell, "Use of side-looking airborne radar to determine lake depth on the Alaskan North slope," *Cold Regions Res. Eng. Lab., Hanover, NH, USA, No. CRREL-SR-230*, 1975.

[103] C. Elachi, M. L. Bryan, and W. F. Weeks, "Imaging radar observations of frozen Arctic lakes," *Remote Sens. Environ.*, vol. 5, pp. 169–175, 1976.

[104] M. O. Jeffries, H. Wakabayashi, W. F. Weeks, "ERS-1 SAR backscatter changes associated with ice growing on shallow lakes in Arctic Alaska," *International Geoscience and Remote Sensing Symposium*, vol.4, pp. 2001-2004, 18-21 Aug 1993.

[105] H. Wakabayashi, W. F. Weeks, M. O. Jeffries, "A C-band backscatter model for lake ice in Alaska," *International Geoscience and Remote Sensing Symposium*, pp.1264-1266 vol.3, 18-21 Aug 1993.

[106] M. O. Jeffries, K. Morris, W. F. Weeks, and H. Wakabayashi, "Structural and stratigraphic features and ERS 1 synthetic aperture radar backscatter characteristics of ice growing on shallow lakes in NW Alaska, winter 1991–1992," *J. Geophys. Res.*, vol. 99(C11), pp. 22459–22471, 1994.

[107] M. Engram, et al. "Synthetic aperture radar (SAR) backscatter response from methane ebullition bubbles trapped by thermokarst lake ice," *Canadian Journal of Remote Sensing*, vol. 38, no. 6, pp. 667-682, 2013.

[108] N. Garcia, and E. Stoll. "Monte Carlo calculation for electromagnetic-wave scattering from random rough surfaces." *Physical review letters*, vol. 52, no. 20, pp. 1798, 1984.

[109] D. Zahn, K. Sarabandi, K. F. Sabet, and J. Harvey, "Numerical Simulation of Scattering from Rough Surfaces: A Wavelet-Based Approach," *IEEE Transactions on Antennas and Propagation*, vol. 48, no. 2, pp. 246-253, February 2000.

[110] K. Sarabandi, Y. Oh, and F. T. Ulaby, "A Numerical Simulation of Scattering from One-Dimensional Inhomogeneous Dielectric Random Surfaces," *IEEE Transactions on Geoscience and Remote Sensing*, vol. 34, no.2, pp. 425-432, March 1996.

[111] T. C. Chiu, and K. Sarabandi, "Electromagnetic Scattering Interaction between a Dielectric Cylinder and a Slightly Rough Surface," *IEEE Transactions on Antennas and Propagation*, vol. 47, no. 5, pp. 902-913, May 1999.

[112] K. Sarabandi, and T.C. Chiu "Electromagnetic Scattering from Slightly Rough Surfaces With Inhomogeneous Dielectric Profile," *IEEE Transactions on Antennas and Propagation*, vol. 45, no. 9, pp. 1418-1430, September 1997.

[113] K. Sarabandi, "Derivation of Phase Statistics from the Mueller Matrix," *Radio Science*, vol. 27, no. 5, pp. 553-560, September – October 1992.

[114] K. Sarabandi, P. F. Polatin, and F. T. Ulaby, "Monte Carlo Simulation of Scattering from a Layer of Vertical Cylinders," *IEEE Transactions on Antennas and Propagation*, vol. 41, no. 4, pp. 465-475, April 1993.

[115] K. F. Warnick and W. C. Chew, "Numerical simulation methods for rough surface scattering," *Waves in Random Media*, vol. 11, no. 1, pp. 1-30, 2001.

[116] Y. Oh, and K. Sarabandi, "Improved Numerical Simulation of Electromagnetic Wave Scattering from Perfectly Conducting Random Surfaces," *IEE Proceedings-Microwave, Antennas and Propagation*, vol. 144, no. 4, pp. 256-260, August 1997.

[117] S. H. Lou, L. Tsang, C. H. Chan, and A. Ishimaru. "Application of the Finite Element Method to Monte Carlo." *Journal of electromagnetic waves and applications*, vol. 5, no. 8, pp. 835-855, 1991.

[118] K. Sarabandi, "Scattering from Variable Resistive and Impedance Sheets," *Journal of Electromagnetic Waves and Applications*, vol. 4, no. 9, pp. 865-891, 1990.

[119] K. Sarabandi, "Scattering from Dielectric Structures Above Impedance Surfaces and Resistive Sheets," *IEEE Transactions on Antennas and Propagation*, vol. 40, no. 1, pp. 67-78, January 1992.

[120] W. F. Weeks, A. J. Gow, and R. J. Schertler. "Ground-truth observations of ice-covered North Slope lakes imaged by radar," *No. Crrel-81-19. Cold Regions Research And Engineering Lab Hanover NH*, 1981.

[121] D. Isleifson, L. Shafai, D. G. Barber, "Numerical rough surface scattering simulations using the FVTD method," *15th International Symposium on Antenna Technology and Applied Electromagnetics (ANTEM)*, pp.1-4, 25-28 June 2012.

[122] R. E. Collin, *Antenna and Radio Wave Propagation*, Sec. 4-1, New York: McGraw-Hill, 1985.

[123] W. H. Bragg, W. L. Bragg, "The Reflexion of X-rays by Crystals". *Proceedings of the Royal Society of London. Series A, Containing Papers of a Mathematical and Physical Character*, pp. 428-438, 1913.

[124] I. Gherboudj, Monique Bernier, R. Leconte, "A Backscatter Modeling for River Ice: Analysis and Numerical Results," *IEEE Transactions on Geoscience and Remote Sensing*, vol. 48, no. 4, pp. 1788-1798, April 2010.

[125] Engineering Toolbox, Webpage: http://www.engineeringtoolbox.com/air-solubility-water-d_639.html.

[126] K. Sarabandi, P. F. Polatin, and F. T. Ulaby, "Monte Carlo Simulation of Scattering from a Layer of Vertical Cylinders," *IEEE Transactions on Antennas and Propagation*, vol. 41, no. 4, pp. 465-475, April 1993.

[127] K. Sarabandi, and T. B. A. Senior, "Low Frequency Scattering from Cylindrical Structures at Oblique Incidence," *IEEE Transactions on Geoscience Remote Sensing*, vol. 28, no. 5, pp. 879-885, September 1990.

[128] Y. C. Lin, and K. Sarabandi, "Electromagnetic Scattering Model for a Tree Trunk Above a Tilted Ground Plane," *IEEE Transactions on Geoscience and Remote Sensing*, vol. 33, no. 4, pp. 1063-1070, July 1995.

[129] D. Sievenpiper, L. Zhang, R. Broas, N. G. Alexopolous, and E. Yablonovitch, "High-impedance electromagnetic surfaces with a forbidden frequency band," *IEEE Transactions on Microwave Theory and Techniques*, vol. 47, no. 11, Nov. 1999.

[130] F. Yang, and Y. Rahmat-Samii, "Reflection phase characterizations of the EBG ground plane for low profile wire antenna applications," *IEEE Transactions on Antennas and Propagation*, vol. 51, no. 10, pp. 2691- 2703, Oct. 2003.

[131] H. Mosallaei, and K. Sarabandi, "Antenna Miniaturization and Bandwidth Enhancement Using a Reactive Impedance Substrate," *IEEE Transactions on Antennas and Propagation*, vol. 52, no. 9, pp. 2403-2414, September 2004.

[132] N. Altunyurt, M. Swaminathan, R. Pulugurtha, and V. Nair, "Analysis on the miniaturization of reactive impedance surfaces with magneto-dielectrics," *IEEE Antennas and Propagation Society International Symposium*, June 2009.

[133] K. Buell, D. Cruickshank, H. Mosallaei, and K. Sarabandi, "Patch antenna over RIS substrate: a novel miniaturized wideband planar antenna design," *Antennas and Propagation Society International Symposium*, vol. 4, pp. 269- 272, June 2003.

[134] K. Sarabandi, A. M. Buerkle, and H. Mosallaei, "Compact Wideband UHF Patch Antenna on a Reactive Impedance Substrate," *IEEE Antennas and Wireless Propagation Letters*, vol. 5, no. 1, pp. 503-506, Dec. 2006.

[135] F. Urbani, F. Bilotti, A. Alu, and L. Vegni, "Low cost compact active integrated antenna with a reactive impedance surface,"*IEEE/ACES International Conference on Wireless Communications and Applied Computational Electromagnetics*, pp. 257- 260, April 2005.

[136] Z. Du; K. Gong; J. S. Fu, B. Gao, and Z. Feng, "A compact planar inverted-F antenna with a PBG-type ground plane for mobile communications," *IEEE Transactions on Vehicular Technology*, vol. 52, no. 3, pp. 483- 489, May 2003.

[137] S. Mahdi Moghadasi, A. R. Attari, and M. M. Mirsalehi. "Design of three-layer circular mushroom-like EBG structures." *Proceedings of the Electromagnetics Research Symposium*, pp. 143-146, 2008.

[138] G. Goussetis, A. P. Feresidis, J. C. Vardaxoglou, "Tailoring the AMC and EBG characteristics of periodic metallic arrays printed on grounded dielectric substrate," *IEEE Transactions on Antennas and Propagation*, vol. 54, no. 1, pp. 82- 89, Jan. 2006.

[139] A. P. Feresidis, G. Apostolopoulos, N. Serfas, J. C. Vardaxoglou, "Closely coupled metallodielectric electromagnetic band-gap structures formed by double-layer dipole and tripole arrays," *IEEE Transactions on Antennas and Propagation*, vol. 52, no. 5, pp. 1149-1158, May 2004.

[140] A. E. Waltho, "Frequency selective surfaces to suppress surface currents," *US patent* no. 7190315 B2, March 2007.

[141] B. Gao; M. M. F. Yuen, "Passive UHF RFID Packaging With Electromagnetic Band Gap (EBG) Material for Metallic Objects Tracking," *IEEE Transactions on Components, Packaging and Manufacturing Technology*, vol. 1, no. 8, pp. 1140-1146, Aug. 2011.

[142] M. Hosseini, A. Pirhadi, and M. Hakkak, "A novel AMC with little sensitivity to the angle of incidence using 2-layer jerusalem cross FSS." *Progress In Electromagnetics Research*, pp. 43-51, 2006.

[143] Y. Dong, H. Toyao, and T. Itoh, "Design and Characterization of Miniaturized Patch Antennas Loaded With Complementary Split-Ring Resonators," *IEEE Transactions on Antennas and Propagation*, vol. 60, no. 2, pp.772-785, Feb. 2012.

[144] O. Luukkonen, C. Simovski, G. Granet, G. Goussetis, D. Lioubtchenko, A. V. Raisanen, and S. A. Tretyakov, "Simple and Accurate Analytical Model of Planar Grids and High-Impedance Surfaces Comprising Metal Strips or Patches," *IEEE Transactions on Antennas and Propagation*, vol. 56, no. 6, pp. 1624-1632, June 2008.

[145] A. B. Yakovlev, O. Luukkonen, C. R. Simovski, S. A. Tretyakov, S. Paulotto, P. Baccarelli, and G. W. Hanson, "Analytical modeling of surface waves on high impedance surfaces," *Metamaterials and Plasmonics: Fundamentals, Modelling, Applications*, pp. 239-254, 2009.

[146] A. B. Yakovlev, M. G. Silveirinha, O. Luukkonen, C. R. Simovski, I. S. Nefedov, and S. A. Tretyakov, "Characterization of Surface-Wave and Leaky-Wave Propagation on Wire-Medium Slabs and Mushroom Structures Based on Local and Nonlocal Homogenization

Models," *IEEE Transactions on Microwave Theory and Techniques*, vol. 57, no. 11, pp.2700-2714, Nov. 2009.

[147] S. A. Tretyakov, *Analytical Modeling in Applied Electromagnetics*. Boston, MA, Artech House, 2003.

[148] N. Van de Meijs, and J. T. Fokkema, "VLSI circuit reconstruction from mask topology," *Integration*, no. 2, pp. 85-119, 1984.

[149] A. J. Witten, J. E. Molyneux, and J. E. Nyquist, "Ground penetrating radar tomography: Algorithm and case studies," *IEEE Trans. Geosci. Remote Sensing*, vol. 31, pp. 461-467, Mar. 1994.

[150] L. L. Monte, D. Erricolo, F. Soldovieri, and M. C. Wicks, "Radio frequency tomography for tunnel detection," *IEEE Trans. Geosci. Remote Sensing*, vol. 48, no. 3, pp. 1128-1137, Mar. 2010.

[151] T. J. Cui and W. C. Chew, "Novel diffraction tomographic algorithm for imaging two-dimensional targets buried under a lossy earth," *IEEE Trans.Geosci. Remote Sensing*, vol. 38, no. 4, pp. 2033-2041, Jul. 2000.

[152] T. B. Hansen and P. M. Johansen, "Inversion scheme for ground penetrating radar that takes into account planar air-soil interface," *IEEE Trans. Geosci. Remote Sens.*, vol. 38, no. 1, pp. 496-506, Jan. 2000.

[153] T. J. Cui and W. C. Chew, "Diffraction tomographic algorithm for the detection of three-dimensional objects buried in a lossy half-space," *IEEE Trans. Antennas Propag.*, vol. 50, no. 1, pp. 42-49, Jan. 2002.

[154] R. W. Deming and A. J. Devaney, "Diffraction tomography for multi-monostatic ground penetrating radar imaging," *Inv. Prob.*, vol. 13, pp. 29-45, 1997.

[155] G. Adamiuk, T. Zwick, W. Wiesbeck, "Dual-orthogonal polarized Vivaldi antenna for ultra wideband applications," *17th International Conference on Microwaves, Radar and Wireless Communications*, pp.1-4, 19-21 May 2008.

[156] A. Elsherbini, K. Sarabandi, "Compact Directive Ultra-Wideband Rectangular Waveguide Based Antenna for Radar and Communication Applications," *IEEE Transactions on Antennas and Propagation*, vol.60, no.5, pp.2203-2209, May 2012.

[157] A. Elsherbini, K. Sarabandi , "Dual-Polarized Coupled Sectorial Loop Antennas for UWB Applications," *IEEE Antennas and Wireless Propagation Letters*, vol.10, pp.75-78, 2011.

[158] J. J. Lee, "Slotline impedance," *IEEE Transactions on Microwave Theory and Techniques*, vol.39, no.4, pp.666-672, Apr 1991.